

3-28-2024

Human Motion-Inspired Inverse Kinematics Algorithm for a Robotics-Based Human Upper Body Model

Urvish Trivedi
University of South Florida

Follow this and additional works at: <https://digitalcommons.usf.edu/etd>



Part of the [Robotics Commons](#)

Scholar Commons Citation

Trivedi, Urvish, "Human Motion-Inspired Inverse Kinematics Algorithm for a Robotics-Based Human Upper Body Model" (2024). *USF Tampa Graduate Theses and Dissertations*.
<https://digitalcommons.usf.edu/etd/10252>

This Dissertation is brought to you for free and open access by the USF Graduate Theses and Dissertations at Digital Commons @ University of South Florida. It has been accepted for inclusion in USF Tampa Graduate Theses and Dissertations by an authorized administrator of Digital Commons @ University of South Florida. For more information, please contact digitalcommons@usf.edu.

Human Motion-Inspired Inverse Kinematics Algorithm for a Robotics-Based Human Upper
Body Model

by

Urvish Trivedi

A dissertation submitted in partial fulfillment
of the requirements for the degree of
Doctor of Philosophy
Department of Mechanical Engineering
College of Engineering
University of South Florida

Co-Major Professor: Rajiv Dubey, Ph.D.
Co-Major Professor: Redwan Alqasemi, Ph.D.
Tansel Yucelen, Ph.D.
Sudeep Sarkar, Ph.D.
Kandethody Ramachandran, Ph.D.

Date of Approval:
March 27, 2024

Keywords: Weighted Least Norm, Motion Capture,
Performance Criteria, Redundant Robotic Model, OpenSim

Copyright © 2024, Urvish Trivedi

Dedication

I dedicate this dissertation to my beloved family, my parents, whose unwavering hard work and countless sacrifices have been the cornerstone of my journey. To my sister Niyati, brother-in-law Harsh, and my adorable niece Jashvi, your constant support and boundless love have been my motivation and strength.

I extend my heartfelt appreciation to all my teachers, starting from my school days. Special recognition goes to Deepak Doshi, whose passion for teaching ignited my thirst for knowledge. Throughout my academic voyage, Prof. Dr. Rajiv Dubey and Dr. Redwan Alqasemi have been my guiding lights, offering unwavering support and imparting invaluable wisdom.

I also want to express my sincere gratitude to our beloved family friends, Gautam Patel, Falguni Patel, Zarna Amin, and Vijay Patel, for their unwavering and unconditional support on this journey. This dissertation is dedicated to you, symbolizing the meaningful connections that have sustained me throughout my academic pursuit.

To my cherished friends, who have been my unwavering pillars of support through every challenge and triumph, my gratitude knows no bounds. To Nirali Patel, Harsh Patel, Pankti Mehta, Tayyeb Mehmood, Maria Ghulam, Dr. Swapnil Jagtap, Yash Patel and all my friends both in India and the United States, your invaluable assistance and constant encouragement have been indispensable during this demanding journey.

This dissertation is a reflection of the collective efforts and love of my cherished family, dedicated teachers, and loyal friends. Thank you all for being a part of this significant chapter in my life.

Acknowledgments

The research was carried out at the University of South Florida, made possible through the generous support of the Florida Department of Education—Division of Vocational Rehabilitation.

Table of Contents

List of Tables.....	iv
List of Figures	vi
Abstract	viii
Chapter 1: Introduction	1
1.1 Research Motivation	1
1.2 Research Stages and Objectives	2
1.3 Dissertation Outline.....	3
Chapter 2: Literature Review	6
2.1 Study Methodology	7
2.1.1 Robot Manipulators	8
2.1.2 Test Environments	12
2.1.3 Single/Dual-Manipulator Motion.....	16
2.2 Redundancy Resolution Methods.....	19
2.2.1 Closed-Form Solutions	21
2.2.2 Gradient Projection Methods	22
2.2.3 Weighted Least-Norm Solution	25
2.2.4 Constrained Optimization	26
2.2.5 Machine Learning, Neural Networks, and Reinforcement Learning	29
2.3 Performance Criteria	33
2.3.1 Manipulability.....	34
2.3.2 Norm of the Gravity and Payload Torques	35
2.3.3 Velocity Ratio.....	38
2.3.4 Mechanical Advantage	39
Chapter 3: Motion Capture Dataset, Right-Hand Upper Body Model, and Motion Analysis	43
3.1 Motion Capture Dataset.....	44
3.1.1 Marker Placement and Vicon Camera Setup	44
3.1.2 Participants	48
3.1.3 Experimental Setup.....	49
3.1.3.1 Range of Motion Tasks.....	49
3.1.3.2 Activities of Daily Living Tasks	53
3.1.3.3 Objects	55
3.2 Upper Body Model for OpenSim Model and Motion Files.....	56
3.3 Upper Body Model for MATLAB	57
3.4 Post-Processed Dataset.....	59
3.5 Trajectory Generation and Velocity Mapping.....	61
3.6 Statistical Parametric Mapping.....	64
3.7 Motion Analysis	66
3.7.1 Motion Analysis of the Range of Motion Task.....	66

3.7.2 Motion Analysis of the Brushing Task	68
3.7.3 Motion Analysis of the Drinking from a Cup Task	70
3.7.4 Motion Analysis of the Opening a Higher-Level Cabinet Task.....	71
3.7.5 Motion Analysis of the Picking Up a Full Water Jug for Shelving Task.....	73
Chapter 4: The Method and Results of Evaluating the Influence of Arm Configurations on Various Performance Criteria.....	76
4.1 Brushing Task	77
4.2 Drinking from a Cup Task.....	80
4.3 Opening a Higher-Level Cabinet Task.....	82
4.4 Picking Up a Full Water Jug for Shelving Task	84
4.5 Summary	86
Chapter 5: The Method and Results of Identifying Phase Dominant Inverse Kinematics Optimization Criteria Based on Motion Capture Data	88
5.1 Brushing Task	89
5.2 Drinking from a Cup Task.....	91
5.3 Opening a Higher-Level Cabinet Task.....	93
5.4 Picking Up a Full Water Jug for Shelving Task	96
5.5 Summary	98
Chapter 6: Inverse Kinematics Methods and Results Predicting Human-Like Motion.....	100
6.1 Inverse Kinematics Methods for Predicting Human Motion.....	100
6.1.1 Least Norm Solution	100
6.1.2 Weighted Least Norm Solution.....	103
6.1.2.1 Link Based Weights	104
6.1.2.2 Joint Limits Avoidance Weights	105
6.1.2.3 Gradient Based Weights.....	108
6.1.2.4 Combined Weights.....	110
6.1.3 Error Analysis	111
6.2 Results of Different Motion Control Algorithm.....	112
6.2.1 Brushing Task	113
6.2.2 Drinking from a Cup Task.....	118
6.2.3 Opening a Higher-Level Cabinet Task.....	124
6.2.4 Picking Up a Full Water Jug for Shelving Task	129
Chapter 7: Discussion and Future Works.....	135
7.1 Discussion	136
7.2 Limitation.....	141
7.3 Contribution	142
7.4 Future Work	143
References.....	146

Appendix A: Copyright Permissions	158
Appendix B: Institutional Review Board Document	159
Appendix C: Data Collection Documents	160

List of Tables

Table 3.1	Marker description	46
Table 3.2	Subject demographic information.....	49
Table 3.3	Activities of daily living tasks.	54
Table 3.4	Segment weight.....	58
Table 3.5	D-H parameters of RHUBM model.....	58
Table 3.6	OpenSim and MATLAB joint angles mapping information	60
Table 3.7	File formats	61
Table 3.8	Motion analysis of the range of motion task.....	67
Table 3.9	Motion analysis of the brushing task	68
Table 3.10	Motion analysis of the drinking from a cup task	70
Table 3.11	Motion analysis of the opening a higher-level cabinet task.....	72
Table 3.12	Motion analysis of the picking up a full water jug for shelving task.....	73
Table 4.1	Results of brushing task	78
Table 4.2	Results of drinking from a cup task	80
Table 4.3	Results of opening a higher-level cabinet task	83
Table 4.4	Results of picking up a full water jug for shelving task	85
Table 6.1	Average weights of eight subjects using combined weights method	114
Table 6.2	Brushing task average RMS error evaluation	115
Table 6.3	Weight distribution in the WLN_{CWM} method for torso flexion/extension joint	117

Table 6.4	Weight distribution in the WLN_{CWM} method for elbow pronation/supination joint	118
Table 6.5	Average weights of eight subjects using combined weights method	120
Table 6.6	Drinking from a cup task average RMS error evaluation	121
Table 6.7	Weight distribution in the WLN_{CWM} method for torso rotation joint	123
Table 6.8	Weight distribution in the WLN_{CWM} method for elbow pronation/supination joint	124
Table 6.9	Average weights of eight subjects using combined weights method	126
Table 6.10	Opening a higher-level cabinet task average RMS error evaluation	127
Table 6.11	Weight distribution in the WLN_{CWM} method for torso rotation joint	128
Table 6.12	Weight distribution in the WLN_{CWM} method for elbow pronation/supination joint	129
Table 6.13	Average weights of eight subjects using combined weights method	131
Table 6.14	Picking up a full water jug for shelving task average RMS error evaluation	132
Table 6.15	Weight distribution in the WLN_{CWM} method for torso rotation joint	134
Table 6.16	Weight distribution in the WLN_{CWM} method for shoulder rotation joint	134

List of Figures

Figure 2.1	The organization flow chart of the literature review	6
Figure 2.2	Categorization of the studies based on the experimental setup	7
Figure 2.3	Comparative analysis of the biomimetics approach on single vs. dual arms	17
Figure 3.1	Camera positions relative to subject and motion capture system origin.....	45
Figure 3.2	Upper body marker placement front body	47
Figure 3.3	Upper body marker placement back body	47
Figure 3.4	Lower body marker placement	48
Figure 3.5	Torso flexion	50
Figure 3.6	Torso rotation.....	51
Figure 3.7	Torso lateral flexion.....	51
Figure 3.8	Shoulder external/internal rotation	52
Figure 3.9	Shoulder ab/adduction	52
Figure 3.10	Shoulder flexion/extension	52
Figure 3.11	Forearm pronation/supination.....	53
Figure 3.12	Elbow flexion/extension	53
Figure 3.13	RHUBM MATLAB model	59
Figure 3.14	Phases of the brushing task	69
Figure 3.15	Phases of the drinking task	71
Figure 3.16	Phases of the opening a higher-level cabinet task	72
Figure 3.17	Phases of the picking up a full water jug for shelving task	74

Figure 3.18	Flowchart of the data flow during the development of the RHUBM	75
Figure 4.1	Brushing task	77
Figure 4.2	Drinking from a cup task	80
Figure 4.3	Opening a higher-level cabinet task.....	82
Figure 4.4	Picking up a full water jug for shelving task	85
Figure 5.1	The mean continua of the criteria for brushing task	89
Figure 5.2	Left: The LM and AVR mean continua with their standard deviations	89
Figure 5.3	The mean continua of the criteria for drinking from a cup task	91
Figure 5.4	Left: The LM and AVR mean continua with their standard deviations	92
Figure 5.5	The mean continua of the criteria for opening a higher-level cabinet task	93
Figure 5.6	Left: The LM and LVR mean continua with their standard deviations	94
Figure 5.7	The mean continua of the criteria for picking up a full water jug for shelving task.....	96
Figure 5.8	Left: The LM and LMA mean continua with their standard deviations	96
Figure 6.1	Gradient of joint limit	109
Figure 6.2	Torso flexion/ extension joint trajectory for subject S06.....	117
Figure 6.3	Elbow pronation/supination joint trajectory for subject S06	118
Figure 6.4	Torso rotation joint trajectory for subject S06.....	123
Figure 6.5	Elbow pronation/supination joint for subject S06	124
Figure 6.6	Torso rotation joint trajectory for subject S04.....	128
Figure 6.7	Elbow pronation/supination joint trajectory for subject S04	129
Figure 6.8	Torso rotation joint trajectory for subject S04.....	133
Figure 6.9	Shoulder rotation joint trajectory for subject S04.....	134

Abstract

The goal of this research is to develop a human motion-inspired inverse kinematics algorithm framework specifically designed for a Robotics-Based Human Upper Body Model (RHUBM). This framework offers solutions to challenges in various fields. In humanoid robotics, the framework addresses the problem of unnatural robot movement by enabling the development of motion planning algorithms that incorporate human-like movements. For prosthetics, the framework tackles the challenge of amputee difficulty in learning and controlling prosthetics by providing a user-friendly interface that predicts and visualizes upper limb movements, enabling learning and practice. In rehabilitation therapy, the framework tackles the issue of developing effective training protocols by assisting physiotherapists in creating customized programs based on natural human movements, potentially improving stroke recovery.

The central hypothesis of this research suggests that, compared to heavier joints, humans prioritize the movement of lighter joints and integrate various performance criteria—including manipulability, velocity ratio, and mechanical advantage—while avoiding joint limits across different phases of Activities of Daily Living (ADLs). Based on this idea, to develop a framework for motion planning, this research involves five primary objectives, each with specific outcomes.

- Objective 1 is the creation of a subject-specific, ten-degree-of-freedom RHUBM using a Motion Capture System (MoCap) in the OpenSim and MATLAB software platforms. The MoCap data includes eight range-of-motion (RoM) tasks and nine ADLs, recorded using an eight-camera Vicon motion analysis system. OpenSim enables the calculation of joint angles, which can then be integrated into the robotic model created within MATLAB.

- Objective 2 is evaluating the influence of arm configurations moving in a null space on each performance criterion and understanding how their combination governs motion.
- Objective 3 is identifying dominant performance criteria. The full task trajectory is segmented into 4-5 major phases, depending on the specific ADL task. Motion capture data are analyzed to identify the dominant performance criteria during each phase of the respective task. A weight matrix is derived, assigning weights to each joint based on these observations.
- Objective 4 involves developing an inverse kinematics control algorithm, utilizing the Weighted Least Norm (WLN) approach. This algorithm allocates weights to each joint based on the identified performance criteria, thereby establishing priority among redundant joints and generating human-like motion. The weight matrix used in the WLN algorithm is built on three key components:
 - The first component is Joint Load Management. This component results in less movement of heavier joints, such as the torso, by assigning higher weights to them. This approach minimizes overall joint and muscle strain by reducing movement in heavier joints compared to lighter ones.
 - The second component is Joint Limit Avoidance. This component ensures that joint movements stay within predefined boundaries.
 - The third component is Performance Criteria Optimization. Gradient-based weights optimize specific performance criteria during different task phases, enhancing the overall performance of the robot.
- Objective 5 involves comparative analysis of WLN algorithm outcomes against MoCap. The MoCap datasets are used as a benchmark to compare the results generated by integrating various weights into the WLN algorithm. The algorithm's efficiency is also

assessed by comparing it against the Least Norm solution. The results indicate that combining link weights, joint limit criteria weights, and gradient-based weights enhances accuracy in recreating human-like motion.

Building upon these results, future research will expand in two stages. The initial stage will focus on expanding the data collection through the recruitment of a more diverse group of participants and the inclusion of a broader spectrum of ADLs. Such expansion is essential for the development of more reliable motion planning algorithms. The subsequent stage aims to investigate various methods for resolving redundancy, including the implementation of advanced machine learning techniques, such as reinforcement learning. These techniques will be tailored to the unique characteristics of users and will prioritize human-like motions. These advancements have the potential not only to enhance the lives of individuals relying on prosthetics and improve the capabilities of robotic assistants but also to facilitate more collaborative and efficient human-robot partnerships.

Chapter 1: Introduction

1.1 Research Motivation

As humanity enters a new era marked by post-humanization, the role of robots is set to undergo significant transformation. They are expected to play a crucial role in enriching human existence, contributing to daily life, work, and a multitude of tasks. However, to ensure robots can seamlessly integrate into environments designed for humans, they must embody qualities such as safety, reliability, and user-friendliness. Progress in these areas, especially in mimicking natural phenomena and achieving human-like motion, continues to pose a significant challenge [1].

In light of this, researchers are actively working on the development of robots endowed with human-like design and motion. Empirical research findings have shed light on the profound influence of human-like motion in redundant joint robotics systems during collaborative interactions[2]. Additionally, it highlights the benefits of developing interfaces that can predict and visualize upper limb movements tailored to specific prostheses, enabling users to learn prescribed motions and reduce the risk due to compensatory motions[3]. It also illustrates the advantages of designing a rehabilitation tool based on human motion [4], which would enable both the prosthesis user and the occupational therapist to quantify and assess the individual's performance.

To cultivate and sustain this advantage of predicting human motion, robust motion planning algorithms are required. These algorithms must demonstrate the capacity to accurately replicate and simulate human motion, aligning with the primary motivation of this research.

1.2 Research Stages and Objectives

The central hypothesis of this research suggests that humans prioritize the movement of heavier joints and integrate various performance criteria, including manipulability, velocity ratio, and mechanical advantage while avoiding joint limits across different phases of ADLs. To facilitate this research, we have identified specific research objectives as follows:

- The first objective is centered on the establishment of a comprehensive database. The MoCap dataset contains eight RoM tasks and nine ADLs, recorded using an eight-camera Vicon motion analysis system. The RoM tasks include elbow flexion and extension, forearm pronation and supination, shoulder flexion and extension, shoulder abduction, adduction, and rotation, torso flexion and extension, torso lateral flexion, and torso rotation. The ADLs performed were brushing, drinking from a cup, opening a lower-level cabinet, opening a higher-level cabinet, picking up the box, picking up the duster and cleaning, picking up an empty water jug for shelving, picking up a full water jug for shelving, and picking up a water jug and pouring. This research focuses on four tasks: brushing hair, drinking from a cup, opening a higher-level cabinet, and picking up a full water jug for shelving. The data collected have been used to construct subject-specific upper-body models within the OpenSim environment, facilitating the computation of joint angles in the OpenSim framework, which can subsequently be applied to the subject-specific robotic model developed in the MATLAB framework. This objective involves data collection, preprocessing, and organization to ensure its suitability for further research and analysis.
- The second objective entails an in-depth evaluation of the impact of different arm configurations on each performance criterion and an understanding of how their combination governs motion.

- The third objective includes identifying dominant performance criteria during the execution of ADLs at different phases. The task trajectory is segmented into 4-5 major phases based on the specific ADL task. The aim is to quantify and analyze the dominant performance criterion during each phase for the respective task.
- The fourth objective focuses on developing a WLN inverse kinematics algorithm. By allocating weights to each joint based on the identified performance criteria in the previous steps, this algorithm establishes priority among redundant joints and generates human-like motion.
- The fifth and final objective involves comparing the results generated by integrating various weights into the WLN algorithm with the MoCap dataset. Additionally, the efficiency of the algorithm is assessed by comparing it against the Least-Normal solution. The investigation will explore the intricacies of these algorithms and their applicability in human motion prediction.

In summary, these research objectives establish the framework for a comprehensive study to advance our understanding of human motion. Through a combination of empirical data collection and algorithm development, this research endeavors to contribute to the fields of robotics and biomechanics by enhancing our capability to replicate and predict human-like motion for various applications.

1.3 Dissertation Outline

Chapter 2 explores background information related to redundancy resolution methodologies applied in motion generation to replicate human motion. This in-depth analysis of the existing body of literature identifies promising directions for future research efforts while revealing substantial constraints inherent in existing motion planning approaches. Moreover, this

section references scholarly publications that thoroughly examine various aspects, including redundant robots, performance criteria, biomimetics, imitation learning, and learning from demonstration techniques employed for controlling redundant robot motion.

Chapter 3 is dedicated to the thorough explication of methodologies employed for data collection. These procedures are utilized to construct subject-specific full-body models within the OpenSim framework, facilitating subsequent calculations of joint angles. These derived joint angles are then incorporated into the subject-specific robotic model developed within the MATLAB framework. This chapter encompasses the systematic progression of crafting the upper body human model, including data filtering and pre- and post-processing protocols.

Chapter 4 provides a detailed overview of how diverse performance criteria influence humans' choice of particular arm configurations during various ADLs. It utilizes null space projection and investigates whether human motion results from optimizing a single criterion or a combination of multiple criteria.

Chapter 5 offers a detailed overview of how different performance criteria influence arm movements across various phases of ADLs. This investigation yields invaluable insights into the influences exerted by distinct performance criteria within the context of ADLs.

Chapter 6 provides a detailed overview of different inverse kinematics algorithms and discusses the development of the weight matrix, integrating various factors such as link weight, distribution of weights based on joint limit criteria, and weights derived from optimizing distinct performance criteria. Additionally, this chapter explores methods such as the LN and WLN techniques, along with the trajectory generation process. It also summarizes a comprehensive examination of the results obtained using WLN and LN algorithms, evaluating and enhancing their interpretative clarity and contextual relevance concerning each ADL.

Chapter 7, the concluding chapter, functions as a summative synthesis of the research outcomes and their implications within domains such as biomedical engineering, rehabilitation programs, virtual reality, gaming, and animation. It also provides limitations and recommendations for future research avenues within these domains.

Chapter 2: Literature Review¹

The primary objective of this section is to comprehensively document, categorize, and critically analyze the outcomes and constraints associated with diverse robot manipulators, experimental configurations, redundancy resolution techniques, and various performance criteria employed to replicate human-like motion during the execution of various ADLs. The categorization of literature is accomplished based on the specific experimental setups/study methodology, the redundancy resolution methods, and the performance criteria utilized in these studies. The visual representation of this categorization is provided in Figure 2.1, which offers a graphical depiction of the classification framework for the reviewed literature, facilitating a more structured and systematic understanding of the research landscape in this domain.

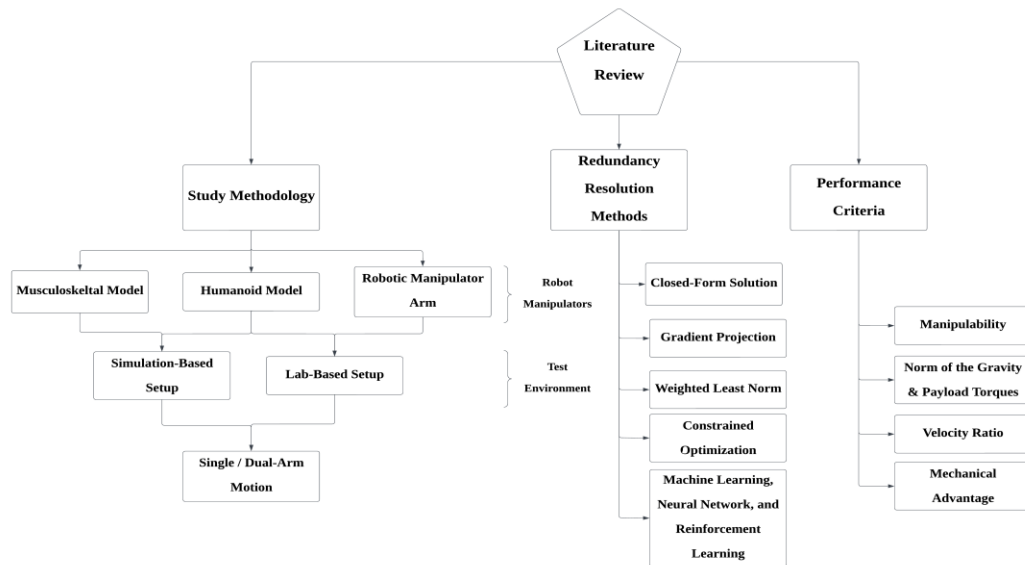


Figure 2.1 The organization flow chart of the literature review

¹ This chapter was published in Trivedi, U., et al., Biomimetic Approaches for Human Arm Motion Generation: Literature Review and Future Directions. *Sensors*, 23(8): p. 3912. Permission is included in Appendix A

Initially, the search yielded 142 publications, which were potentially relevant to the study. However, after applying the inclusion criteria, only 96 are relevant to this research. The included publications, representing the most current research on the topic, were published after 2003.

2.1 Study Methodology

Biomimetic research aims to create robots and software platforms capable of emulating human movements within a human-centric context. This simulation process involves initially developing a physical system model based on a theoretical framework, followed by the practical implementation of this model and a subsequent in-depth analysis of its performance [5]. As the complexity of robotic systems continues to increase, the role of simulation becomes increasingly pivotal in optimizing and validating motion before these algorithms are deployed in tangible robotic entities. As illustrated in Figure 2.2, our literature review reveals that 74% of biomimetics studies have utilized simulation platforms, with the remaining 26% opting for real robotic implementations[6]. Several factors influenced this distribution, including the costs associated

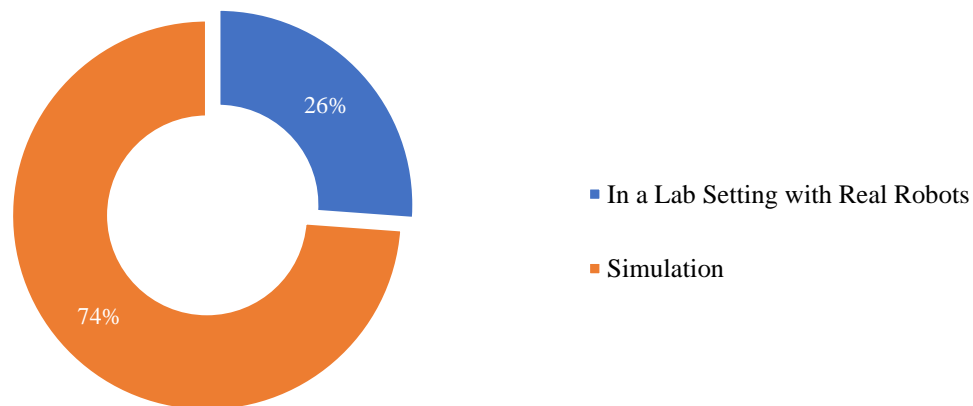


Figure 2.2 Categorization of the studies based on the experimental setup

with experiments, the availability of robotic equipment, and the specific tasks to be undertaken. Notably, Silva et al.[7] demonstrated that anthropomorphic robots, capable of replicating human-like movements, facilitate human-robot collaboration. These anthropomorphic attributes enhance

the efficiency and naturalness of human-robot interactions, allowing human users to better comprehend the robot's movements as purposeful actions.

Developing autonomous object manipulation capabilities in anthropomorphic robots poses a formidable challenge, primarily due to several complex factors:

- Anthropomorphic robots typically possess a high number of DOFs, endowing them with flexibility and the capacity to rapidly compensate for control deviations while adapting to new dynamics. However, concurrently controlling multiple DOFs in a predictive and goal-oriented manner presents substantial computational challenges in the domain of cognitive robotics.
- Generating optimal end-effector trajectories is imperative to prevent collisions between the robot itself and the objects in its environment.
- The optimization of diverse performance criteria plays a crucial role in generating joint angle trajectory paths that closely mimic human movements.

2.1.1 Robot Manipulators

In recent decades, substantial research endeavors have been dedicated to the development of robots capable of emulating human anthropomorphism. These musculoskeletal robots aspire to achieve a harmonious blend of compliance and natural distribution of mass and dynamics, thus mimicking human mechanical attributes. An inherent advantage of these robots resides in their actuators' lightweight and low-inertia characteristics. Richter et al.[8] introduced a design closely mirroring the human arm, featuring a substantial muscle mass affixed to the torso. Tendons, composed of minimal weight, serve as connectors between the muscles and the distal components of the body. Effectively controlling these musculoskeletal models necessitates formulating appropriate control strategies, with a central focus on replicating the efficient mechanisms humans

employ in governing their bodily motions. Research institutions worldwide have been actively engaged in the advancement of robotic musculoskeletal systems, channeling their efforts toward mechanical design or simulation software to achieve human-like performance.

At Stanford University, researchers crafted a comprehensive upper extremity model encompassing the shoulder, elbow, forearm, wrist, thumb, index finger, and 50 muscle compartments spanning these joints, resulting in a representation accommodating 15 degrees of freedom [9]. These developed models were deployed to estimate muscle forces and joint moments, leveraging muscle activation patterns. These models' precision was assessed against the maximum moment-generating capacity exhibited by various muscle groups. Fan et al. [10] pursued a parallel trajectory, introducing an artificial muscle-driven robotic arm characterized by multifilament muscles that closely mirrored the physiological attributes of human arm muscles. These multifilament muscles underwent modeling within a simulation environment, yielding humanoid robot arm models ideally suited for emulating human motion. Control policies were cultivated using reinforcement learning methodologies to evaluate the controllability and the capacity to replicate human motion across diverse muscle configuration models.

In a comprehensive investigation by Al Borno et al. [11], muscle synergy models were seamlessly integrated into a biomechanically realistic upper extremity model, primarily derived from [9]. The core objective of this model was to simulate upper extremity movements in real-time. Computational experiments were orchestrated to scrutinize the effects of muscle synergies on task performance, facilitate participant learning of movements, and ascertain the generalizability of these synergies to other movement patterns. In a parallel avenue of exploration, Lenarcic et al. [12] embarked on a mission to replicate the well-established characteristics of three-dimensional upper extremity movements. Their pursuit involved the creation of a biomechanically realistic

computational model, primarily grounded in [9], with a specific emphasis on reproducing features regulated by Fitts' law. Additionally, Sapiro et al.[13] delved into the realm of predicting arm configurations during reaching movements by assessing the muscular effort requisite for positioning tasks. They adeptly leveraged the musculoskeletal model originating from Holzbaur et al.[9] to effectively account for kinematic coupling inherent in the human shoulder.

The comprehensive examination of human-like movement necessitates the deployment of mathematical models, either encompassing the entirety of the human body or specific components thereof, to facilitate an analysis of kinematic and dynamic characteristics. These mathematical representations of the human arm exhibit diversity across various research groups. Lenarcic et al. [12] delineated the human arm as a serial mechanism comprising four distinct parts: the shoulder girdle, upper arm, forearm, and hand. In contrast, Chan et al.[14] proposed a model featuring eight DOFs and encompassing three primary segments: the upper arm, forearm, and hand. Gams et al.[15], in their endeavor, conceptualized a model comprising four core segments: the shoulder girdle, upper arm, forearm, and hand, each endowed with ten DOFs. Notably, a prevalent approach entails the representation of the human arm through seven-DOF kinematic chains for each arm [3], featuring three rotational joints dedicated to the shoulder, one each for the elbow and forearm, and two allocated for the wrist.

Humanoid models, tailored to approximate human proportions, joint limitations, and kinematic parameters, invariably encompass multiple degrees of freedom (DOFs). Commonly, these models embrace a minimum of seven DOFs per arm, alongside three for the torso and six for the legs. Diligent researchers are fervently committed to crafting robot models that faithfully align with human attributes. For instance, Tomic et al. [16], leveraging the kinematic foundation established by the ROMEO robot, painstakingly devised a human body model housing a total of

35 DOFs. Within this comprehensive model, seven DOFs were allocated for each arm, six for each leg, one for each foot, two for the neck, two for the head, and one for the spine. Notably, an array of robot platforms, including Simon, NAO, and the HOAP-3, was employed by other researchers [17-20], each marked by its unique DOF distribution. Pertinently, the HOAP-3 and NAO commanded a collective tally of 25 degrees of freedom, albeit with nuanced variations in the allocation of DOFs throughout their respective anatomies.

When confronting the intricacies of redundant manipulators, wherein an infinite array of joint angle configurations may lead to a specific desired outcome, the direct mapping of human motion onto a robot arm encounters infeasibility owing to disparities in length and joint constraints. Researchers have adeptly tackled this correspondence challenge through the implementation of optimization-based strategies. Notwithstanding inherent workspace constraints, select research groups have opted for six-DOF robotic arms, such as the UR5 and Jaco2 [21, 22]. The UR5 arm, for instance, embraces two DOFs on the shoulder, one in the elbow, and three in the wrist. Conversely, the Jaco2 arm encompasses a shoulder joint marked by one DOF, an elbow featuring one DOF, a wrist boasting three DOFs, and a final DOF dedicated to regulating the robotic arm's rotation. Furthermore, researchers have progressively embraced seven-DOF robotic arms, exemplified by the KUKA [23] and Mitsubishi's PA-10 [24], driven by the pursuit of expanded workspace capabilities and the maximization of arm redundancy. Within the realm of hyper-redundant robot arms, characterized by a higher degree of freedom, in-depth research has persisted for several decades, albeit with limited practical applications. Liarokapis et al. [25] ingeniously harnessed a constrained optimization approach to engineer hyper-redundant robot arms, crafting arms with nine, eight, twenty, and twenty-one degrees of freedom, each thoughtfully tailored to either exceed, align with, or marginally deviate from the average length of the human arm.

2.1.2 Test Environments

Over the past several decades, many simulation tools tailored for robotic systems have proliferated in the market. Various research groups and industrial sectors have extensively utilized these tools, serving as indispensable aids in designing and validating control algorithms. Notably, these simulation tools' primary focus revolves around robotic manipulators' manipulation and motion within diverse environments, with less emphasis placed on their graphical interfaces. Central to all simulation systems is the inclusion of either kinematic or dynamic models, instrumental in replicating the intricate motions of robot manipulators.

In the realm of biomimetics research, two primary categories of simulation tools emerge: those developed as extensions atop existing simulation platforms, exemplified by MATLAB [26], OpenSim [27], and Cosimir [28], and tools crafted by research groups to precisely evaluate the performance of their algorithms [29].

The field of biomechanical movement analysis has witnessed an escalating reliance on computer models in recent times. This burgeoning interest stems from the conviction that modeling endeavors have the potential to substantially enhance our comprehension of the intricate interplay between the neuromuscular and musculoskeletal systems in generating human movement. A prominent open-source software application, OpenSim, has been pivotal in this domain. Researchers employ OpenSim to construct detailed musculoskeletal structures and execute dynamic simulations encompassing various movements [27]. These musculoskeletal models are invaluable tools for scrutinizing the biomechanics underpinning diverse movements and the intricate neuromuscular control mechanisms governing them.

To ensure fidelity in modeling, researchers, such as Fox et al.[30], have endeavored to engineer highly detailed upper extremity models, incorporating a comprehensive 15 degrees of

freedom. These musculoskeletal models have been instrumental in scrutinizing human motion patterns. Additionally, in the context of biomimetics research, it is posited that the central nervous system (CNS) leverages modularity as a fundamental principle to streamline the control of the multifaceted, multi-dimensional musculoskeletal system. This entails minimizing motor commands by encapsulating them within a compact set of modules known as muscle synergies. These modules function cohesively as a system and offer a vantage point for in-depth motion analysis. In this vein, Al Borno et al.[11] harnessed a biomechanically realistic upper extremity model grounded in OpenSim to simulate muscle synergies. Fan et al.[10] adopted a parallel approach, employing the same model to execute reinforcement learning experiments. Sapio et al.[13] further extended these experiments to optimize muscle effort criteria, all within the purview of this detailed musculoskeletal model.

The MATLAB software platform has emerged as a preeminent choice for developing models and simulations spanning various systems. MATLAB's foundational data types, vectors, and matrices render it exceedingly versatile and aptly suited for simulating robotic systems and their dynamics [31]. Among the pantheon of MATLAB extensions, the robotics toolboxes pioneered by Peter Cork[26] have garnered preeminence as the most extensively employed adjuncts. This toolbox has played a pivotal role in shaping human-like models and facilitating the implementation of diverse optimization algorithms. Notably, the values of key parameters governing upper-body motion were derived by Fox et al.[30] through the ROM tasks, employing the Denavit and Hartenburg convention. Conversely, Menychtas et al.[3] charted a distinct course, fashioning a robotic model of the human body rooted in Lie algebra. Drawing upon the ROM data, this model entailed the extraction of parameters encompassing segment lengths and joint centers to craft the robot model and compute joint angles, thereby enabling the analysis of assorted ADL

tasks. An analogous MATLAB-based robotics toolbox by Peter Cork was adroitly employed by [32] to actualize a kinematic model of the human arm, affording the analytical study of swivel motion and manipulability in task execution, with implications for endowing humanoid robots with human-like behavior.

Furthermore, researchers have embraced the utilization of software platforms such as ROS (Robot Operating System) [33] and Mujoco[34]. Both of these open-source software suites have been architected to empower researchers across the domains of robotics, biomechanics, and machine learning[5]. Beyond their open-source nature, one of their preeminent advantages lies in their seamless integration and compatibility with a diverse array of hardware and software components, thereby conferring flexibility and adaptability to researchers working within the realm of robotics. Moreover, these software platforms offer extensive tools and libraries to facilitate communication and orchestration among disparate hardware elements. By adeptly configuring and integrating these components, developers can expedite the creation of intricate robotic systems, obviating the need for ground-up construction—a testament to the efficiency and utility of these software packages. Given their comprehensive libraries and robust online support ecosystems, ROS and Mujoco have emerged as reliable cornerstones for many researchers [10].

The burgeoning demand for robot assistance has witnessed sustained growth over the past two decades across a spectrum of fields that share physical workspaces with humans, encompassing industries, service robotics, and rehabilitation. While simulation software offers highly reliable and cost-effective avenues for motion planning, the comportment of robots in real-world scenarios necessitates predictability and social acceptability for the system to thrive. Numerous research collectives have undertaken extensive studies to enhance the quality of assistance proffered by robot manipulators and humanoid robots in diverse real-world scenarios

[35-37]. For instance, Su et al.[38] scrutinized the human capacity to manage redundancy while teleoperating anthropomorphic robot arms, specifically KUKA robots. In their pursuit of an anthropomorphic arm posture during teleoperation, they employed a nonlinear regression methodology rooted in neural networks to establish a correlation between the elbow swivel angle of the human arm and the target hand pose. A simulation was executed to evaluate this method's effectiveness, followed by laboratory experiments. Complementary studies, such as those presented by Liu et al.[39] and Artemiadis et al.[40]. Similarly, human demonstration tracking experiments assessed the efficacy of algorithms designed to generate human-like motion by optimizing the elbow swivel angle. These endeavors entailed the utilization of KUKA and PA-10 robotic platforms to emulate human motions. In a different vein, Kim et al. [41] pioneered a method for modifying and scaling the trajectory of the wrist and the angle of elbow elevation to reproduce human-like arm motions.

Chen et al. [42] unveiled a computational framework founded upon the hierarchical tenets of human motor control to derive hand configuration trajectories. Leveraging a second-order kinematic model, they endeavored to encapsulate the dynamic intricacies of the hand, culminating in an external representation of the high-level motor control system. To validate the effectiveness of their proposed approach, a battery of self-reaching movements was executed on a seven DOFs anthropomorphic arm, with the resultant configuration trajectory compared to authentic human movement in terms of spatiotemporal profiles. Similarly, Elbasiony et al.[19] pioneered an innovative interface for imparting entire-body human demonstrations to robots, emphasizing the seamless integration of the learning framework and the demonstration interface. This symbiotic integration empowered the NAO robot to learn, and replicate demonstrated motions, transcending mere imitation autonomously. Dynamic time warping (DTW) was harnessed for signal alignment

to curtail motion dimensionality, while a Gaussian process latent variable model (GPLVM) was invoked for modeling and replicating the demonstrated motions. Albrecht et al. [43] introduced a framework predicated on optimizing physically inspired principles and analyzing human motion recorded in an unconstrained observational setting. The authors dissected motion recording data through a bilevel optimization approach to discern the most fitting cost function for characterizing human arm movements. This cost function, in turn, engendered optimal trajectory paths for iCub, a humanoid robot tasked with performing functions akin to those executed by a human.

2.1.3 Single/Dual-Manipulator Motion

In response to recent advancements in biomimetics and the continuous evolution of robotics technology, there is a growing interest in studying dual-arm movements and developing robotic manipulators with human-like attributes. A comprehensive analysis, as depicted in Figure 2.3, indicates that a substantial portion of the research endeavors, comprising 79%, has primarily focused on devising methodologies for generating single-arm motions. In contrast, a relatively smaller fraction, constituting 21% of the studies, has been dedicated to proposing techniques for dual-arm motion generation. Several variables contribute to this observed distribution, including the specific manipulators and simulator platforms employed in experimental setups and the nature of the tasks designed for experimentation.

Tasks ranging from simple pick-and-place operations to intricate assembly processes require different levels of coordination and synchronization between robotic arms. Researchers may prioritize developing methodologies that address the specific challenges posed by the tasks they intend to investigate. For instance, tasks involving dual-arm manipulation often necessitate solutions that ensure precise coordination and collaboration between the arms, which may lead to a greater emphasis on dual-arm motion generation techniques in studies focusing on such tasks.

An illustrative example of this research trajectory is presented by Zanchettin et al. [44], who introduced a straightforward correlation between hand posture (comprising position and orientation) and swivel angle during task execution. The proposed relationship is based on the fundamental connection between hand pose and swivel angle. Utilizing kinematic variables as a foundation, the authors established that this relationship could be readily applied to control robotic manipulators, elucidating the motion of an arm. Employing human volunteers as participants tasked with executing assembly-like operations, an extensive experimental investigation was conducted. This investigation sought to scrutinize and substantiate the connection between hand poses and swivel angles by combining clustering and multivariate correlation statistics. The outcomes of this study culminated in the successful application of the model to a humanoid robot, namely the ABB FRIDA, thereby showcasing the model's proficiency in generating human-like dual-arm movements.

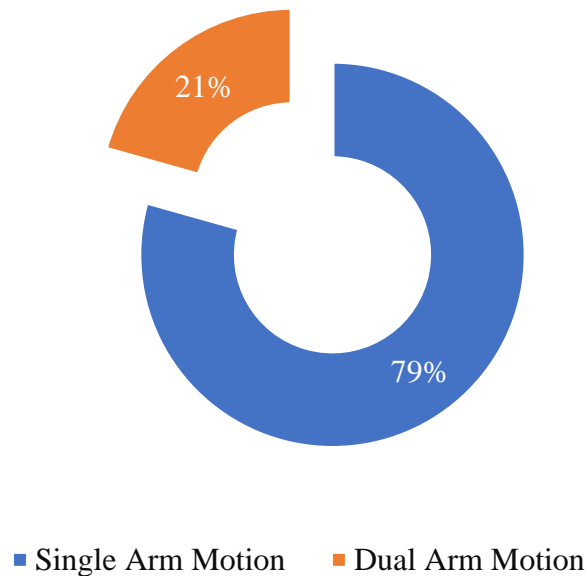


Figure 2.3 Comparative analysis of the biomimetics approach on single vs. dual arms

In a comparable vein, Lamperti et al. [45] introduced a strategy to address redundancy in an anthropomorphic dual-arm robotic system while minimizing muscular effort. The foundational premise was that the problem of right-hand positioning could be effectively resolved by minimizing muscular activation, i.e., the muscular effort required to maintain the manipulator's position against gravitational forces. This objective was achieved by computing an optimal swivel angle based on the hand's position. Likewise, the definition of left arm posture was predicated on identifying a left swivel angle that minimized the muscular effort in moving the left arm. Leveraging data samples from various dual-arm tasks, the authors mapped arm configurations to eight redundant variables that collectively defined hand pose and swivel angle. Continuing along this trajectory, Garcia et al. [46] investigated the attainment of human-like motion by a mobile anthropomorphic dual-arm robot, focusing on the influence of the robot's mobile base on its dual-arm synergies. The research aimed to establish harmonious coordination between the robot's translational movements and arm actions during dual-arm manipulation tasks on a table. The study unfolded in three distinct phases. In the initial phase, human movements were acquired and transposed into the robotic system as a human operator executed manipulation tasks while approaching a table. The subsequent phase involved a detailed analysis of the acquired movements to elucidate the relationships between robot position, orientation, arm configuration, and recorded movements. Based on the derived robot configurations, the study delved into fluctuations within these relationships and computed dual-arm synergies using the mapped robot configurations. The Cartesian space was discretized and segmented into various regions by conducting computations and observing correlations within the collected data. A motion planning algorithm founded on rapidly exploring random trees (RRT) was introduced in the final phase. This algorithm harnessed

synergies between different regions of the Cartesian space to generate coordinated movements closely resembling human actions.

The methodology pursued by Shin et al. [47] for instilling human likeness in the models involved the utilization of specific criteria, specifically hand trajectory and elbow trajectory. These trajectories were generated by manipulating the elbow elevation angle (EEA). To this end, the authors proposed a control method grounded in the virtual dynamics model (VDM). A VDM-based controller filtered the target trajectory of a motion (or force) to be regulated and subsequently transmitted it to the robot's motor controller, which executed the motion on the robot. The VDM-based controller conferred direct control over the robot arm without necessitating the resolution of inverse kinematics or avoidance of geometric singularities. The efficacy of the VDM-based controller was evaluated by comparing the arm motion generated by the proposed controller with captured arm motion data. This was exemplified in an object manipulation task demonstrated using a humanoid robot, showcasing a sequence of events involving reaching for, grasping, and relocating an object. Notably, the dependency on databases limited the generalization of manipulation tasks within the VDM-based controller approaches.

In summary, a significant portion of research has concentrated on developing techniques for generating single-arm reaching movements emulating human-like motion, with limited exploration of intricate manipulation movements. Nonetheless, recent strides in biomimetic research have paved the way for more intricate applications in robotics, including dual-arm manipulation that draws inspiration from actual human biological and psychological patterns.

2.2 Redundancy Resolution Methods

Generally, six degrees of freedom (DOFs) are adequate to accurately position the end-effector in both location and orientation within its workspace. However, achieving a specific

position and orientation solely through a single set of joint angles is feasible and practical for robots operating in structured environments, often assigned to repetitive, similar tasks. Nevertheless, as environmental complexity increases due to the introduction of obstacles or the necessity for more intricate tasks, the reliance on this joint-to-space mapping diminishes significantly. To address this challenge, the introduction of redundant joints to the robotic manipulator's kinematic chain emerges as a solution. Redundant joints enable the creation of multiple configurations leading to a particular end-effector position. It is worth noting that this enhancement comes at the cost of necessitating the utilization of more sophisticated control algorithms tailored for redundant manipulators, capitalizing on the additional DOFs.

The human body, equipped with numerous joints and under the refined control of the central nervous system, possesses the remarkable ability to execute highly intricate tasks in unstructured environments. Consequently, biomimetic robots aspire to replicate aspects of human motion, thereby establishing a kinematic and dynamic correspondence with the desired end-effector, typically the hand. This endeavor adopts a task-driven approach, wherein the challenge is to identify the specific facets of human motion that warrant duplication while concurrently maintaining translational and rotational velocities consistent with the intended end-effector behavior.

This multifaceted challenge has spurred diverse approaches, each attempting to resolve the intricacies of human motion emulation. These approaches encompass various methodologies, including the analysis of human motion patterns and the development of human-like control algorithms, among others. The objective of this section is to comprehensively review these diverse strategies and assess the scope and efficacy of each approach. Such an analysis is essential given the ongoing status of human motion emulation as a complex, unsolved problem. Moreover, the

applicative context governs the adequacy of the imitation's precision, necessitating a thorough evaluation of whether the attained results align with the demands of the intended application.

2.2.1 Closed-Form Solutions

The primary category of biomimetic methodologies encompasses closed-form solutions designed to replicate human motion. Closed-form solutions provide analytical techniques for efficiently resolving inverse kinematics problems. These methodologies establish a direct mapping between the end-effector's spatial coordinates and the corresponding joint angles, grounded in the robot's geometric characteristics. While closed-form solutions are inherently tailored to each robot's specific geometry, they can precisely determine motion configurations in diverse scenarios. In principle, they represent the most straightforward means of achieving desired robot configurations. However, challenges arise in the context of redundant robots, where a direct one-to-one correspondence between joint angles and end-effector Cartesian coordinates is absent. To achieve configurations resembling human-like movements, additional constraints must be introduced to the robot's mechanical structure and assigned tasks.

For instance, Liu et al. [39] conducted a study employing demonstrators to capture upper extremity motions, facilitating the establishment of key shoulder, elbow, and wrist positions within a predefined plane. The solution to inverse kinematics was confined within this specified plane, compelling the robot to reach the designated endpoint while concurrently maintaining the elbow angle on the prescribed plane. The performance evaluation entailed comparing real-time depth camera data (Kinect) data.

Kim et al. [47] pursued an alternative approach, concentrating on the elbow's elevation angle (swivel) to devise a closed-form solution. They harnessed a response surface methodology (RSM) on motion capture data to approximate the elbow's elevation angle during motion. This

constraint enabled a humanoid robot (MAHRU, developed by the Korean Institute of Science and Technology—KIST) to replicate human-like arm motions. Correspondingly, Zanchetin et al. [48] leveraged the swivel angle to establish a connection between the hand and elbow, identifying a kinematic constraint conducive to human-like movements.

Likewise, Wang et al. [49] incorporated the swivel angle into their closed-form solution. Ding et al. [50] introduced a distinct approach, introducing an intermediate step between the task and joint space, delineated by a triangle formed by the human arm's shoulder, elbow, and wrist (termed the human arm triangle). This intermediary space facilitated the transformation of task space motions onto the human arm triangle, enforcing constraints that streamlined the resolution of the inverse kinematics problem.

The domain of exoskeletons, also necessitating precise replication of human motion, witnessed the utilization of the swivel angle as a constraint by Kim et al. [51], with motion selections based on the projection of maximum manipulability. Subsequently, Kim et al. [32] incorporated a joint angle availability function to address inverse kinematics while considering the swivel angle to minimize energy exchange between the user and the exoskeleton. Chen et al. [42] introduced a more abstract approach, utilizing a composite force field to generate trajectories and incorporating bio-inspired coefficients to determine joint angles. Although optimization methods were applied to MoCap data for coefficient calculation, the core algorithm itself remains independent of such methods, thereby preserving the speed characteristic of a closed-form solution.

2.2.2 Gradient Projection Methods

The second category of methodologies encompasses the gradient projection method, primarily involving numerical techniques for addressing motion resolution within the null space

at the velocity level. This approach allows for the incorporation of additional degrees of freedom to satisfy supplementary criteria without compromising end-effector precision. Unlike closed-form solutions, which typically rely on geometrical or anatomical constraints, gradient projection methods adopt more abstract criteria to govern motion. These methods are generally represented by Equation 2.1,

$$\dot{q} = J^\# \dot{X} + \lambda(I - J^\# J) \nabla k \quad 2.1$$

where in \dot{q} denotes the joint angle velocity vector, $J^\#$ represents the generalized inverse of the Jacobian matrix (usually the Moore–Penrose inverse), λ signifies a scaling factor, I stands for the identity matrix, and ∇k represents the gradient vector. In essence, $J^\# \dot{X}$ utilizes the requisite joint motion to guide the end-effector along the desired Cartesian trajectory, while the remaining components of the equation manipulate the joints within the null space to fulfill optimization criteria.

While specific details may vary among different implementations, the core objective of the gradient projection method is to define an appropriate ∇k (sometimes accompanied by a factor λ) that facilitates the generation of anthropomorphic motion. This approach offers the advantage of ensuring that the end-effector accurately follows the defined trajectory, irrespective of the criteria employed. Furthermore, it is computationally efficient and suitable for real-time motion resolution. However, it should be noted that the method primarily resolves inverse kinematics locally, determining the motion that satisfies constraints at each step rather than generating a comprehensive motion profile that minimizes or maximizes criteria across the entire trajectory. In cases where the criteria are not on the brink of violation, the outcome corresponds to the least-norm solution.

The research conducted in this domain concentrates on identifying appropriate criteria that lead to biomimetic motion. For example, Zhao et al. [52] proposed a criterion that minimized potential energy while considering wrist discomfort factors to synthesize motion, projecting them into the null space to generate human-like motion. Alibeigi et al. [19] employed the gradient of two cost functions in real-time mapping of human motions onto an anthropomorphic robot (NAO), thereby preserving end-effector and joint configurations between humans and robots. Lura et al. [53] utilized a probability density function derived from MoCap data to discern human-like postures during specific tasks primarily aimed at prosthesis users. The density function was optimized with varying workspace increments and data sizes, revealing a trade-off between accuracy and robustness.

Poignant et al. [54] utilized the Rapid Upper Limb Assessment (RULA) to generate ergonomically comfortable postures for prosthesis users. Xie et al. [55] incorporated a minimum jerk criterion and defined a target arm pose to establish desirable motion, while Artemiadis et al. [40] applied a probability distribution function. By using a Bayesian network to record joint motions, Artemiadis and colleagues established the interdependency of joints, resulting in an objective function projected into the null space for the joints. Other methods have employed more specific criteria for gradient projection, including manipulability. Manipulability measurements not only evaluate comfort levels provided by a posture [56] but can also be harnessed to simulate human movements.

Gams et al. [15] applied a manipulability maximization criterion to ensure that the arm maintained high levels of dexterity throughout the posture. They developed a weighting matrix through trial and error. An advanced concept of manipulability criterion was implemented by Jaquier et al. [57], where a manipulability ellipsoid profile was employed to control a humanoid

robot. Building upon this method, Jaquier et al. later demonstrated [58] that the manipulability of the ellipsoid was task-dependent and transferrable to robots for human-like movement. Sentis et al. [59] showcased the feasibility of applying the gradient projection method to recursively apply multiple criteria, refining the executed motion in the process.

2.2.3 Weighted Least-Norm Solution

The WLN solution method bears similarities to the gradient projection technique, albeit with a key distinction: it does not separate the rank and null spaces and is expressed in the general form depicted in Equation 2.2.

$$\dot{q} = WJ^T (JWJ^T)^{-1} \dot{X} \quad 2.2$$

In this equation, W represents a typically diagonal weighting matrix, and J^T denotes the transpose of the Jacobian matrix. Notably, this equation marked the earliest endeavor to resolve kinematics for redundant manipulators. In 1969, Whitney [60] introduced the WLN as a means to address motion resolution for both manipulators and human prosthetic devices (it is worth noting that the gradient projection was proposed later in 1977 by Alain Liegeois [61]). The WLN approach incorporates weighting factors for each joint, thereby resolving full motion that encompasses both rank and null motion spaces.

Chan and Dubey [62] employed the WLN method to circumvent a robot's joint limits. In their study, a comparison between the WLN and the gradient projection revealed that the WLN consistently moved the mechanism away from the joint limits. Conversely, the gradient projection increased compensation only when the joint limits were approached. Essentially, the WLN remained active continuously, while the gradient projection could be toggled 'on' and 'off,' resulting in increased compensation. In practical terms, the distinctions between these two methods should

be minimal, as biomimetic motion always needs to adhere to specific criteria, implying that both methods remain active at all times.

Lura et al. [63] employed optimization techniques to derive weights tailored for able-bodied individuals, incorporating joint limits to obtain a more personalized motion profile. Subsequently, Menychtas et al. [64] extended this work to prosthesis users. While the initial outcomes appeared promising, the differing anthropometric characteristics of prosthesis users posed challenges in generalizing the results for a broader population. The most practical approach appeared to be the utilization of the average joint velocity during a task [3]. Remarkably, the motion generated through this method exhibited no statistically significant differences compared to the optimized weights. Gams et al. [15] conducted another study employing the WLN method. They combined the gradient projection and the WLN to maintain separation between the two proposed criteria.

In summary, both the gradient projection and the weighted least-norm approaches share the fundamental concept of motion resolution. The end-effector is guided to a desired location, and the null space is controlled in a manner conducive to creating human-like motion. There remains no consensus regarding which criterion yields the most human-like posture, leading researchers to explore diverse constraints aligned with their specific objectives to attain the most favorable results. This trend continues in subsequent methods, where more abstract criteria come into play.

2.2.4 Constrained Optimization

Constrained optimization emerges as a prominent methodology for addressing the inverse kinematics of human motion. In this framework, joint angles are employed as variables within an objective function, and the resultant motion profile derived from these variables plays a pivotal

role in problem resolution. While the specific characteristics that shape this motion profile may exhibit variability, they share commonalities with preceding methods by striving to confine the solution space about a given end-effector position through defined criteria. Constrained optimization is characterized by its capacity, and intrinsic nature, to emulate tasks contingent upon multiple components, each potentially exerting distinct influences across a spectrum of tasks. Essentially, this approach amalgamates criteria without unequivocally prioritizing the dominance of a single criterion. For instance, Kusters and Gleen [89] discerned that kinematics and dynamics differentially influenced motion, with task complexity dictating the appropriateness of kinematic or dynamic resolution. Researchers, driven by specific contextual considerations, typically select constraints, often leading to the formulation of more abstract criteria for optimization—a departure from prior methods where criteria tended to be more intuitive or well-defined.

Lamperti et al. [45] harnessed OpenSim to simulate dual-arm human motions and optimized the motion to mitigate muscular fatigue in an anthropomorphic robot. However, no direct comparison was conducted with MoCap data. Liarokapis et al. [25] formulated their objective function by incorporating three distinct geometric metrics: human-robot distance, joint-based triangle areas, and convex hull characteristics. These metrics quantified dissimilarities between human and robot attributes, enabling the algorithm to map anthropomorphic motion onto the robotic mechanism effectively. Gielniak et al. [65] adeptly employed spatiotemporal coordination to engender human motion, introducing variance to ameliorate non-anthropomorphic repeatability. Intriguingly, their experiments with additional constraints revealed that an increased number of criteria led to a diminution in human-like motion. Tomić et al. [16] devised an algorithm to emulate human motion, showcasing limited error between the desired and robot joint angles. Leveraging a minimum angular jerk criterion for joint angle optimization, Kashima and Hori [66]

effectively employed one of the earliest criteria for generating human-like trajectories, even applicable to rudimentary movements. This same criterion was adopted by Silva et al., whose algorithm adeptly accounted for obstacle avoidance and joint limits. Albrecht et al. derived a cost function from human motion capture data in a unique approach. Subsequently, they applied it to a robot, yielding biomimetic motion harmonizing with its mechanical constraints. Ishida et al.[67] adroitly employed time-varying weights in optimizing a composite cost function, allowing them to faithfully mimic human motion while accommodating soft constraints that could be momentarily relaxed to facilitate the attainment of human-like synergies between two arms.

In the pursuit of human-like motion, Garcia et al. [46] adeptly mapped MoCap data directly onto a robot to generate trajectories. Choi et al. [68] judiciously employed constrained optimization to facilitate the transfer of human motion to multiple humanoid robots. Kim et al. [41] employed a method entailing the definition of swivel angles and a motion plane to map MoCap data onto an anthropomorphic robot, scaling the MoCap data to align with the robot's capabilities. Rosado et al.[69] grappled with a similar challenge, directing human motions directly into the robotic mechanism via a depth camera (KINECT). Subsequently, they conducted constrained optimization to augment the quality of joint angle data, which was subsequently mapped directly onto the robot. The overarching objective of this endeavor was the transference of skills from humans to robots.

Constrained optimization techniques have also gained substantial traction in the domains of wearable robots and simulations of the human body. Kim et al. [70] adeptly computed swivel angle kinematics and dynamics, culminating in synthesized motion that surpassed single-criterion outputs. Similarly, Kashi et al. [31] adroitly leveraged a minimal angular displacement criterion in conjunction with a joint range availability criterion to compute a human-like posture, with the amalgamation of both criteria yielding superior performance. Vetter et al.[71] adroitly introduced

two criteria for elucidating human motion: a postural model associating joint configuration solely with end-effector position and a transport model that factored in the influence of previous posture on the final joint posture. Sha et al. [72] adroitly embraced multiple criteria to engender a biomimetic solution, encompassing total joint power, center of mass displacement, and end-effector error minimization. It is imperative to note that their approach hinged upon a virtual full-body model, thereby circumventing mechanical constraints. Fox et al. [30] astutely employed optimization to generate human motion with the primary goal of scrutinizing the postoperative function of the shoulder and exploring changes in kinematics and muscle effort. In contrast, their study did not involve motion mapping onto a robot; instead, it was designed to simulate the human body. Similarly, Al Borno et al. [73] proficiently employed OpenSim to delve into the speed-accuracy trade-off, attributing this phenomenon to heightened task complexity rather than signal-dependent noise. Additionally, they undertook an exploration of muscle synergies through simulation [11]. In a similar vein, Khatib et al. [74] aptly accounted for cross-joint coupling by harnessing robotic task prioritization techniques, while De Sapio et al. [13] adroitly employed shoulder modeling to factor in cross-joint coupling.

2.2.5 Machine Learning, Neural Networks, and Reinforcement Learning

Machine learning (ML), neural networks (NN), and reinforcement learning (RL) methods serve as instrumental tools in the analysis of MoCap data. These methods employ statistical techniques to extract biomimetic motion patterns from the data. The data is utilized as input, and a discerning pattern recognition process ensues. The algorithm subsequently extracts salient features deemed most relevant to the motion under consideration. This pursuit operates at a relatively high level of abstraction, emphasizing the correlation between features and motion over how these features influence motion. It is imperative to note that this does not entail treating the

criteria as a black box; instead, it underscores the paramount importance of discerning the relationship between features and motion. ML represents an extensive field of research in its own right, but within this discussion, our focus remains confined to biomimetics.

Learning by demonstration is the central tenet driving ML-based control, underpinning various algorithms to glean actionable insights from motion data[75]. ML algorithms facilitate the transfer of human motions to anthropomorphic robots, enabling them to imitate, learn, and replicate these motions. Although ML techniques excel at faithfully mimicking human motion when provided with ample data, their primary focus revolves around something other than creating inherently biologically inspired criteria, a domain more aptly addressed by reinforcement learning. Consequently, the imitated motions lack inherent biological information and are unsuitable for biomechanical simulations. While Fang et al. [76] provide an exhaustive overview of learning from imitation, their emphasis primarily concerns transferring skills from human experts to robots rather than pure biomimicry.

Nonetheless, ML methods exhibit proficiency in emulating human motion and managing more intricate tasks than alternative approaches. In this discussion, our scope is circumscribed to ML algorithms validated for human-like kinematics instead of the broader domain of ML for robot redundancy resolution. Acknowledging that the escalated complexity of algorithms deployed does not intrinsically guarantee superior human imitation is vital. The most judicious methodology hinges on the specific task and pertinent features. For instance, Zanchettin et al. [44] discerned a correlation between swivel angle and hand posture, a revelation instrumental in problem resolution. Unlike methods discussed in sections addressing closed-form solutions, this relationship paved the way for creating a cluster of multiple solutions. Subsequently, a multivariate

correlation approach was employed to ascertain the most suitable solution, forsaking the imposition of limitations on the number of valid solutions available.

Artemiadis et al. [40] employed a Bayesian network to decipher intra-joint connections and mapped out motions using gradient projections. In a parallel endeavor, Park et al. [77] utilized a set of MoCap data to construct a motion primitive database, deriving a broad spectrum of efficient motions, albeit with reported stability concerns and joint limit constraints. Wei et al. explored using a Bayesian network and a coupled Convolutional Neural Network (CNN) to create motion primitives, with the CNN yielding superior performance. Su et al. [38] pioneered a nonlinear regression method employing an NN to control a teleoperated robot, with swivel angle manipulation attaining human-like motion in an industrial setting. To enhance algorithm robustness, they subsequently incorporated a deep convolutional neural network [79]. Later, Su et al. [80] applied these methods to transfer skills from humans to manipulators. Chen et al. [21] also harnessed NNs, reducing solution space dimensionality to address redundancy and curtail the number of potential solutions. This approach engendered human-like motion while mitigating computational and memory expenses.

Conversely, Elbasiony et al. [20] employed the KINECT system to demonstrate motions to a robot. Wen et al. [81] harnessed the KINECT for motion data acquisition, which subsequently served as input to a multi-layer perceptron (MLP) NN, facilitating the transfer of biomimetic movements to a robot. Kratzer et al. [82] adopted a distinctive approach, employing a recurrent NN for offline motion planning and gradient-based trajectory optimization online to account for external parameters and obstacles.

Reinforcement learning (RL) embodies an iterative process involving evaluating a cost function, with parameters continuously refined through each iteration. This approach circumvents

complex inverse kinematic computations, empowering the robot to explore the solution space autonomously until the cost function is converged. Unlike other ML algorithms, RL does not explicitly strive to replicate a given dataset to perfection; instead, it explores the solution space to identify permissible and ideally optimal solutions.

Xie et al. [83] delve into RL, focusing on path planning. This orientation allows researchers to experiment with bio-inspired criteria to replicate biological functions underlying motion under reasonable assumptions. It allows for experimentation with the cost function, culminating in a final algorithm that amalgamates initial criteria and the robot's motion capabilities. Striking a balance between exploration and utilization of existing knowledge is imperative to solve the cost function, where the robot follows the provided information while simultaneously accruing a substantial corpus of new knowledge through the exploration-exploitation trade-off during kinematic resolution.

Liu et al. [84] devise a collision-free, energy-efficient trajectory planning methodology, underpinning an adaptive exploration strategy to expedite the algorithm's convergence. Guenter et al. [85] melds demonstration with RL, enabling the robot to identify alternative solutions when confronted with unexpected perturbations. This feat is accomplished through the application of a Gaussian mixture model (GMM). Calinon and Bilard [18] mirror this approach, leveraging human input in the loop to encode human motion with a GMM and subsequently transfer these gestures to an anthropomorphic robot, harmonizing human and robot motion. Billard et. [28] employ reinforced learning with the aid of neural networks, employing a hierarchy of NNs modeled after the motor control centers within the brain. This paradigm reiterates observed motions internally to generate unique configurations, mirroring biological learning through observation. This approach

diverges from NN methods discussed subsequently, as the network serves to reinforce behavior rather than statistically deduce a pattern.

Lim et al. [86] utilize principal component analysis (PCA) to decompose motions into motion primitives, enabling the robot to amalgamate them for swift and efficient motion akin to humans. Jenkins et al. [87] embrace a bio-inspired classification of percepto-motor primitives to generate human-like motion. Yang et al. [88] pioneered the development of reward functions with MoCap data, employing deep deterministic policy gradient (DDPG) and hindsight experience replay (HER) to empower the robot to mimic human motions. Fan et al. [10] leverage reinforcement learning to govern an anthropomorphic robot using artificial muscles, with the unique characteristic of the system learning how to activate muscles for robot motion.

2.3 Performance Criteria

The researchers dedicated to replicating human-like motion in robots have embarked on an exhaustive analysis of everyday human activities. The primary objective of this investigation is to unveil the intricate interplay of diverse performance criteria that humans instinctively optimize while executing various tasks. The aim is to acquire a profound understanding of these criteria, enabling researchers to harness them effectively for the precise emulation of human motion.

As articulated by Chang in [89], integrating quantitative measures or criteria provides a logical foundation for the analysis, design, and control of complex systems. Performance criteria, often called performance parameters, assume a pivotal role in robotic manipulator design, analysis, task planning, and performance evaluation. Particularly in redundant manipulators, such as humanoid robots boasting multiple inverse kinematic solutions, performance metrics are indispensable tools for selecting the most appropriate solution based on predefined criteria. These metrics facilitate the identification of the optimal posture for a given task, thus contributing to

creating task-specific manipulator configurations. These configurations are designed with the overarching objective of either minimizing or maximizing performance indices throughout the trajectory or specific sections therein.

Throughout the evolution of the field of robotics, a plethora of performance criteria have been introduced, each varying in its level of acceptance within the discipline. Consequently, developing a comprehensive understanding of the context in which these indices should be applied is necessary. As the field of robotics and artificial intelligence continues to advance, an enhanced comprehension of these performance criteria assumes ever-increasing importance in the design and control of robotic systems.

2.3.1 Manipulability

Yoshikawa introduced the concept of the manipulability index as a kinematic performance metric for a manipulator [90]. Among various kinematic indices, the Yoshikawa manipulability index is the most widely acknowledged and utilized in the research domain for assessing kinematic manipulability [91]. Similar to many kinematic metrics, the manipulability index relies on the manipulator's Jacobian matrix for its computation. In the context of a redundant manipulator, it is defined as the square root of the determinant of the product formed by the Jacobian matrix and its transpose. In contrast, for non-redundant manipulators, the Jacobian assumes the form of a square matrix, and the manipulability index is equivalent to the absolute value of its determinant. The linear and angular components of the manipulability can be obtained by using the first or last three rows of the manipulator Jacobian matrix in Equations 2.3 and 2.4. The linear and angular components are denoted by the abbreviations LM and AM, respectively, throughout this paper. It signifies the arm's ability to control and manipulate objects, with higher values indicating more excellent dexterity and agility. This measure indicates the manipulator's dexterity in all directions.

$$\mu = \sqrt{\det(J \cdot J^T)} \quad 2.3$$

$$\mu = |\det(J)| \quad 2.4$$

The manipulability index offers several advantages, particularly in situations where a manipulator approaches singularity. When the determinant of the Jacobian matrix equals zero, it serves as a sufficient condition indicating the presence of a singularity [60]. Notably, recent studies, such as [65], have advocated the superiority of the manipulability index as an indicator of dexterity when compared to metrics like the condition number or minimum singular value. However, it is essential to acknowledge the associated limitations of the manipulability index. For instance, it cannot be used to quantify the proximity to a singularity [91]. Additionally, the manipulability index assumes a value of zero if the Jacobian matrix is not of full rank [92]. A notable drawback is that when the Jacobian loses its full rank, the manipulability index fails to differentiate between various types of singularities, as both scenarios result in determinants equaling zero [89].

Despite these limitations, the manipulability index finds widespread application in workspace optimization, manipulator design [93], and task and trajectory planning. It is important to note that various variations of the manipulability index exist, and readers are encouraged to explore the work conducted by [94] for comprehensive insights. In the context of this research, our primary focus centers around the manipulability index, which provides valuable insights into the dexterity of our robotic hand and its ability to maneuver effectively in various directions.

2.3.2 Norm of the Gravity and Payload Torques

The challenge of comprehending and emulating human motion patterns has long been significant in robotics. This challenge has become increasingly complex with recent advancements in artificial intelligence and the development of complex humanoid systems. Humanoid robots,

characterized by their numerous joints and anthropomorphic, redundant design, require the ability to move in a manner akin to humans. This capability is essential for seamless navigation within human-made environments and for fostering effective interactions with humans. This capability is essential for seamless navigation within human-made environments and fostering effective interactions with humans. Given that humans effortlessly address this challenge, Khatib et.al [74] proposed a methodology to extract and implement the underlying human movement strategies for robotic control.

To unravel these strategies, the authors conducted controlled experiments to explore how humans manage their muscular energy expenditure during precision positioning tasks. In broad terms, the findings underscore the innate human inclination to avoid excessive exertion in routine motions. It becomes evident that humans actively endeavor to minimize the muscular effort required to counteract gravitational forces while executing precision positioning tasks. This metric is normalized by torque capacity. This optimization process capitalizes on the inherent redundancy within the human musculoskeletal system, reducing the energetic demands associated with gravitational compensation. This insight yields the concept of an effort potential introduced in [74], which effectively characterizes human postural motion by minimizing torque on a joint.

$$U(q) = \sum_{i=1}^n w_i \frac{g_i(q)^2}{\Gamma_{B_i}(q)^2} \quad 2.5$$

In the Equation 2.5, $U(q)$ gives us muscle effort potential, g_i represents the gravity torque acting upon joint i . Γ_{B_i} denotes the torque boundaries induced by muscle activity, which can show as either upper or lower boundaries, depending on the sign of gravity. w_i stands for a weighting parameter associated with joint.

In a parallel research effort conducted by Berret et al.[95], they utilized Equation 2.6 as a performance criterion within their inverse optimal control technique. Their investigation yielded a compelling conclusion that human motor control strategies inherently minimize this specific performance criterion during the execution of various reaching tasks in experimental settings.

$$\text{Total Torque} = \int_0^T (\tau_1^2 + \dots + \tau_n^2) dt \quad 2.6$$

Building upon this analogous approach, the current study follows a similar trajectory. In this research, we adopt an analytical approach involving the analysis of joint space trajectories combined with a musculoskeletal model. This analytical framework quantifies the effort required to counteract the combined influence of gravity and payload torques acting on individual joints. Grounded in this analysis, we posit a hypothesis suggesting that humans, in their arm configurations, exhibit a propensity to minimize the aggregate torques experienced by specific joints during task performance.

Based on this foundational premise, we introduce a performance criterion called the norm of the gravity and payload torques criterion (GL). This criterion integrates the norm of gravity and payload torques, providing a holistic evaluation of the torques exerted on the joints shown in Equation 2.7. This criterion serves as a pivotal component of our research framework to shed light on the intricate mechanisms governing human arm motion and the optimization strategies employed to minimize joint torques during various tasks. Where, τ_{LW_i} is a torque on joint i due to link weight and τ_{PL_i} is a torque on joint i due to payload.

$$GL = \sqrt{\sum_{i=1}^n (\tau_{LW_i} + \tau_{PL_i})^2} \quad 2.7$$

This strategic adjustment permits us to concentrate on mitigating the influence of the heavier joints by assigning appropriate link weights. Through the implementation of this approach, our primary goal is to enhance the control and coordination of robotic manipulators while effectively addressing the challenges posed by disparities in joint weights.

2.3.3 Velocity Ratio

Velocity Ratio (VR) is a widely used performance criterion for evaluating the kinematic behavior of Single-Input-Single-Output (SISO) mechanisms such as four-bar chains[96]. However, the concept of velocity ratio can also be applied to study the kinematic behavior of robotic manipulators' multi-input-multi-output (MIMO) mechanisms[97]. In a seminal paper, Dubey and Luh proposed VR as a performance measure for the kinematic evaluation of manipulators[98]. The VR of a robot manipulator is defined as the ratio between the norm of the end-effector velocity vector and the norm of the joint velocity vector as shown in Equation 2.8.

$$VR = \frac{|\dot{x}|_{W_x}}{|\dot{\theta}|_{W_\theta}} \quad 2.8$$

$$|\dot{x}|_{W_x} = \sqrt{\dot{x}_v^T \dot{x}_v}; \quad |\dot{\theta}|_{W_\theta} = \sqrt{\dot{\theta}_v^T \dot{\theta}_v} \quad 2.9$$

$$\dot{x}_v = J_v \dot{\theta}_v \quad 2.10$$

$$J_v = W_x^{\frac{1}{2}} J W_\theta^{-\frac{1}{2}} \quad 2.11$$

$$\dot{x}_v = W_x^{\frac{1}{2}} \dot{x}; \quad \dot{\theta}_v = W_\theta^{-\frac{1}{2}} \dot{\theta} \quad 2.12$$

In this research, we employ a diagonal weight matrix, incorporating successive segment weights, to investigate the influence of link weights on the VR while performing various ADLs, given as,

$$VR = \frac{\dot{x}^T \dot{x}}{\dot{\theta}_{wm}^T W_{\theta} \dot{\theta}_{wm}} \text{ for } W_x = I \quad 2.13$$

$$\dot{\theta}_{wm} = W_{\theta}^{-1} J^T (J W_{\theta}^{-1} J^T)^{-1} \dot{x} \quad 2.14$$

where, $W_x, W_{\theta} \in R^{n \times n}$ are symmetric and positive definite weighting matrices. J is an $m \times n$ Jacobian matrix in reference to the base frame, J_v is transformed Jacobian, \dot{x} is m -Dimensional vector of translational and rotational velocities, \dot{x}_v is transformed end-effector velocities, $\dot{\theta}$ is n -Dimensional vector of joint velocities, $\dot{\theta}_v$ is transformed joint velocities and $\dot{\theta}_{wm}$ is joint velocities using weighted least-norm method. A manipulator's linear and angular velocity ratio can be calculated using the end effector linear or angular velocity norm (\dot{x}) as a numerator in Equation 2.13. VR is a measure that indicates the manipulator's efficiency in terms of the joint motion required to achieve the desired end-effector velocity in the direction of the cartesian motion. A higher velocity ratio means that the manipulator can achieve the desired end-effector velocity with less joint motion. In contrast, a lower velocity ratio indicates that more joint motion is required to achieve the same end-effector velocity. This research uses the LVR and AVR to denote the manipulator's linear and angular velocity ratios.

2.3.4 Mechanical Advantage

Similar to the Velocity Ratio, Mechanical Advantage (MA) stands as another performance criterion for assessing the kinematic behavior of SISO mechanisms, such as four-bar chains[99]. In their research, Dubey and Luh introduced Mechanical Advantage (MA) as a valuable metric for

assessing the kinematics of manipulators[98]. MA helps evaluate a manipulator's ability to apply force and moment effectively at the end-effector in a specific direction. The MA of a robot manipulator is defined as the ratio between the norm of the end-effector force/moment and the norm of the joint torque vector given below.

$$\text{MA} = \frac{|f|_{W_f}}{|\tau|_{W_\tau}} \quad 2.15$$

$$|f|_{W_f} = \sqrt{f_m^T f_m}; \quad |\tau|_{W_\tau} = \sqrt{\tau_m^T \tau_m} \quad 2.16$$

$$\tau_m = J_m^T f_m \quad 2.17$$

$$J_m = W_f^{-\frac{1}{2}} J W_\tau^{\frac{1}{2}} \quad 2.18$$

$$f_m = W_f^{\frac{1}{2}} f; \quad \tau_m = W_\tau^{\frac{1}{2}} \tau \quad 2.19$$

In this research, we utilize a diagonal weight matrix that incorporates consecutive segment weights to explore the impact of link weights on MA during the execution of various ADLs. In Equation 2.18, $W_f, W_\tau \in R^{n \times n}$ are symmetric and positive definite weighting matrices. J is an $m \times n$ Jacobian matrix about the base frame, J_m is transformed Jacobian, f is m -dimensional vector of forces and moment, f_m is transformed end-effector vector of forces and moment; In this study, we are solely considering the direction of the force at the end-effector since we do not have information about the magnitude of end-effector forces. τ is n -dimensional vector joint torque, τ_m is transformed joint torques. The calculation of a manipulator's linear (LMA) and angular (AMA) mechanical advantage can be performed using Equation 2.15. It signifies the arm's

efficiency in transferring forces or torques in the direction of the motion, with higher values indicating a greater ability to apply force or torque for a given input effort.

In conclusion, many techniques are available for addressing the inverse kinematics problem, which involves mapping human body movements to control anthropomorphic robots in diverse ways. The choice of technique depends on the specific application and the desired level of mimicry. Nevertheless, a systematic approach is crucial for reconstructing human motion and translating it into a functional framework. A comprehensive understanding of how the Central Nervous System influences human movement represents a pivotal area for further research. Despite the increasing prevalence of redundant robot research, establishing a formalized framework remains essential to structure experimental setups and optimize approaches for various biomimetic experiments.

This literature review contributes to establishing such a structured approach by categorizing data collection methods, robot manipulators, experimental setups, optimization techniques, and performance criteria. Firstly, human motor control is categorized into three fundamental sections. The first section pertains to diverse experimental setups, categorized by models, distinguishing between simulation-based and laboratory-based setups. The second section delves into various optimization methods, further divided into categories such as machine learning/neural networks, reinforcement learning, weighted least-norm, constrained optimization, and gradient projection. Lastly, the third section focuses on four core performance criteria: Manipulability, Norm of the Gravity and Payload Torques, Velocity Ratio, and Mechanical Advantage.

While biomechanics research has made significant progress in these performance criteria, there remains untapped potential for synergy with biomimetic research in the development of

simulation tools for the analysis and replication of human motion. Although neural networks and machine learning have demonstrated their efficacy in biomimetics, their applicability for novel trajectory applications requires further validation. Researchers are encouraged to leverage insights from human demonstrations to enhance mimicry's robustness. This approach can yield a deeper understanding of the various performance criteria optimized by humans subconsciously during task execution. Such endeavors would enable researchers to build upon prior studies and revisit concepts without duplicating research that has yielded mixed results.

Chapter 3: Motion Capture Dataset, Right-Hand Upper Body Model, and Motion Analysis²

Researchers have established a comprehensive framework for robot motion planning to facilitate human-like motions in robotic systems based on the human model. This framework leverages many optimization techniques to match human-like motions that individuals have demonstrated. Integral to this process is collecting motion data related to the human body and associated objects, which provides essential information for subsequent motion planning endeavors. In this research, we gathered and curated a dataset encompassing human motions during daily activities. This dataset comprises captured and highly accurate whole-body motion data obtained through a Vicon motion capture system. The acquired data has been instrumental in developing subject-specific upper-body models within the OpenSim environment. Furthermore, it has facilitated the computation of joint angles within the OpenSim framework, subsequently adaptable to the subject-specific robotic models constructed within the MATLAB framework. This section introduces an intricate dataset, comprising the following key components:

- The Motion Capture Dataset encompasses recordings acquired via the VICON motion capture system. It encapsulates nine distinct activities of daily living performed by ten healthy individuals. These activities include eight unimanual activities, one bimanual activity, and eight range-of-motion activities.

² This chapter was published in Trivedi, U., R. Alqasemi, and R.J.S. Dubey, CARRT—Motion Capture Data for Robotic Human Upper Body Model. *Sensors*, 23(20): p. 8354. Permission is included in Appendix A.

- Motion files compatible with the OpenSim software environment are thoughtfully provided for each task featured in the dataset. These files allow researchers to examine and scrutinize the captured motions using the OpenSim platform's capabilities.
- An approximated upper body model, designed for utilization within the MATLAB framework and crafted using the Peter Corke Robotic Toolbox, is an integral part of the dataset. This model serves as a valuable asset for investigating various performance criteria.
- The dataset has undergone post-processing procedures to facilitate extensive performance criteria evaluations within the MATLAB environment. This processed dataset empowers researchers to conduct thorough and profound analyses and investigations, contributing to robotic motion planning and emulation advancements.

3.1 Motion Capture Dataset

The principal aim of this section is to deliver a detailed description of the marker placement strategy and camera configuration deployed within the research study. Additionally, it offers an intricate depiction of participant demographics and the experimental arrangement. Furthermore, it encompasses an exhaustive description of the objects deployed in the execution of diverse ADLs. The database encompasses a wide-ranging array of anthropomorphic data, .c3d motion files, and a subject-specific MATLAB model constructed utilizing the Robotic Toolbox.

3.1.1 Marker Placement and Vicon Camera Setup

The complete kinematic data of the participant's entire body was obtained using a Vicon motion capture system, which utilized reflective markers[100] . This system consisted of eight strategically positioned cameras, as depicted in Figure 3.1. The placement of markers involved attaching 43 spherical reflective markers, each with a diameter of 12.5 mm, to the participant's

skin using double-sided adhesive tape. A comprehensive description of these markers, including their labels and spatial coordinates, can be found in Table 3.1, Figure 3.3, Figure 3.2, and Figure 3.4. To ensure the precision of data acquisition, a calibration procedure was performed for each participant at the beginning of the recording session. Participants maintained fixed, static T-positions both at the start and conclusion of each trial. Data from each trial was recorded at a frequency of 120 Hz. To reduce noise and address marker flickering during the trials, the recorded data underwent post-processing using Nexus 1.8.5 software by Vicon (Denver, CO, USA)[100] .

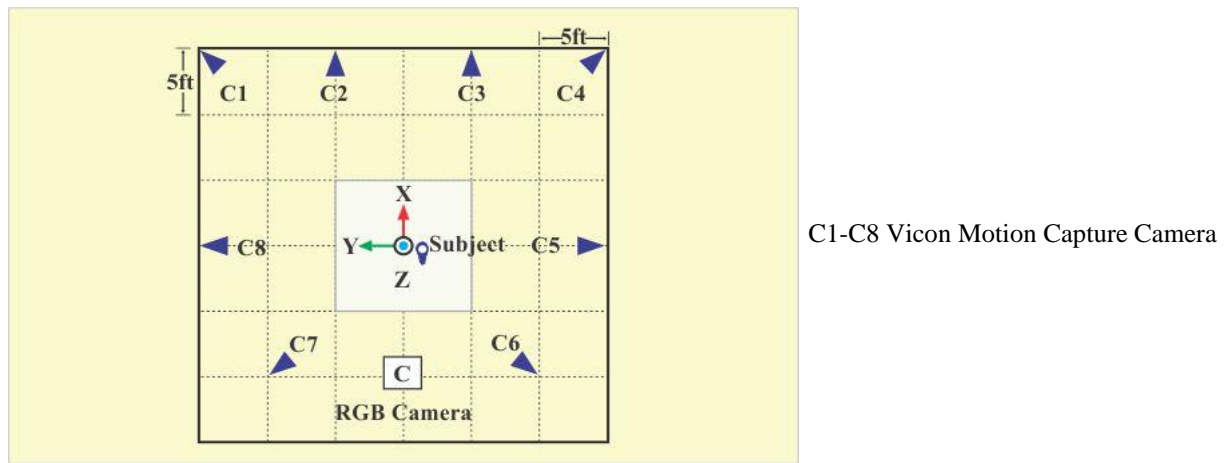


Figure 3.1 Camera positions relative to subject and motion capture system origin

The post-processing was carried out on a computer running Windows 7, equipped with an Intel Core i5 processor, a 250 GB hard disk, and 32 GB of RAM.

The data collection process involved using an RGB video camera, with video recordings conducted at a frame rate of 25 frames per second. To protect the anonymity of participants, each video underwent post-processing using video editing software. It is important to note that the videos themselves are not included in this dataset. Their sole purpose was to ensure the accuracy of the motion capture process.

Table 3.1 Marker description

Name	Marker Placement
T1	Spinous Process; 1st Thoracic Vertebrae
T10	Spinous Process; 10th Thoracic Vertebrae
CLAV	Jugular Notch
STRN	Xiphoid Process
LBAK	Middle Of Left Scapula (Asymmetrical)
R/LASI	Right/Left Anterior Superior Iliac Spine
R/LPSI	Right/Left Posterior Superior Iliac Spine
R/LGT	Right/Left Greater Trochanters
R/LSHOA	Anterior Portion of Right/Left Acromion
R/LSHOP	Posterior Portion of Right/Left Acromion
R/LUPA	Right/Left Lateral Upper Arm
R/LELB	Right/Left Lateral Epicondyle
R/LELBM	Right/Left Medial Epicondyle
R/LFRA	Right/Left Lateral Forearm
R/LWRA	Right/Left Wrist Radial Styloid
R/LWRB	Right/Left Wrist Ulnar Styloid
R/LFIN	Dorsum Of Right Hand Just Proximal To 3rd Metacarpal Head
R/LTHI	Right/Left Thigh
R/LLFC	Right/Left Lateral Epicondyle of Femur
R/LMFC	Right/Left Medial Epicondyle of Femur
R/LTBI	Right/Left Tibia Interior
R/LLMAL	Right/Left Lateral Malleolus
R/LCAL	Right/Left Calcaneus
R/LTOE	Right/Left Toe

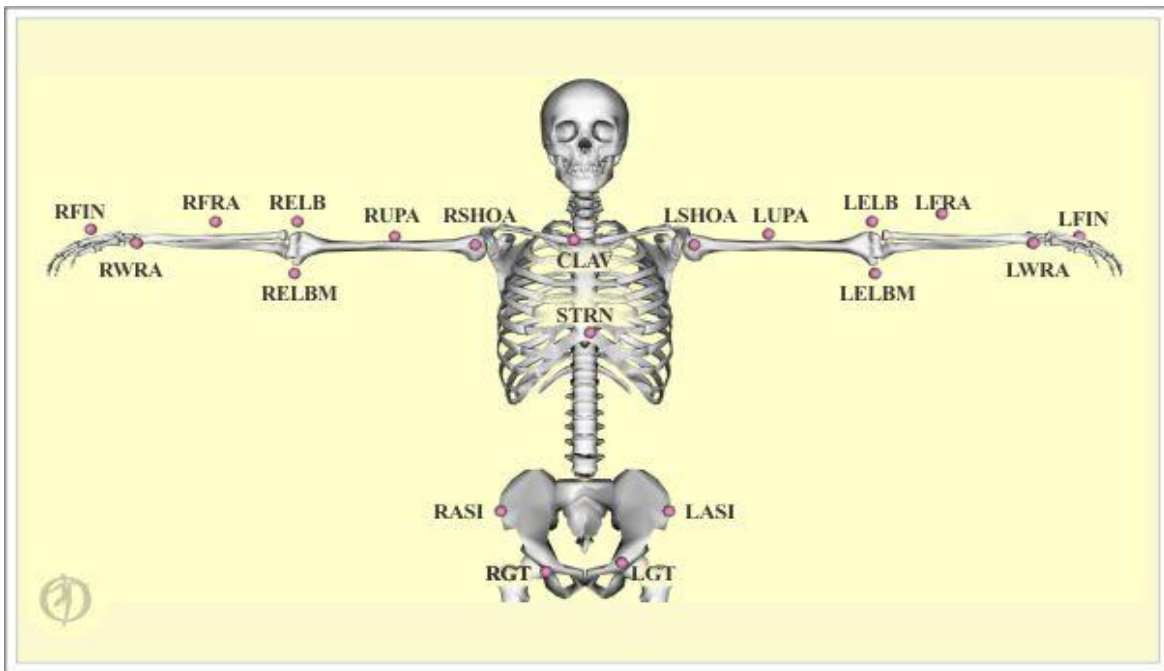


Figure 3.2 Upper body marker placement front body

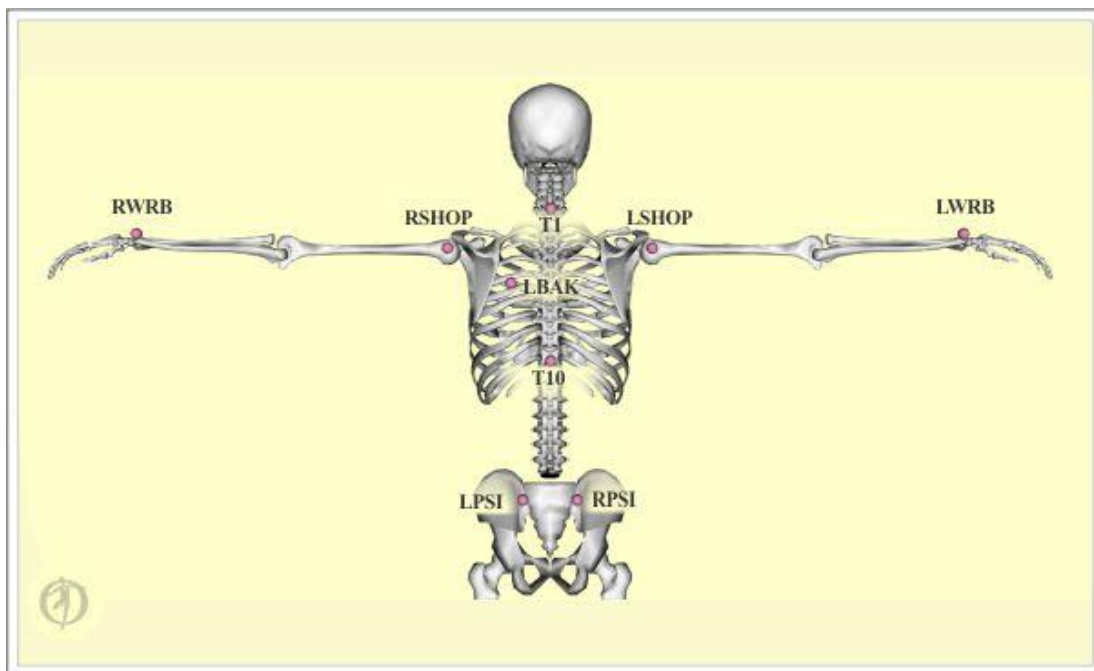


Figure 3.3 Upper body marker placement back body

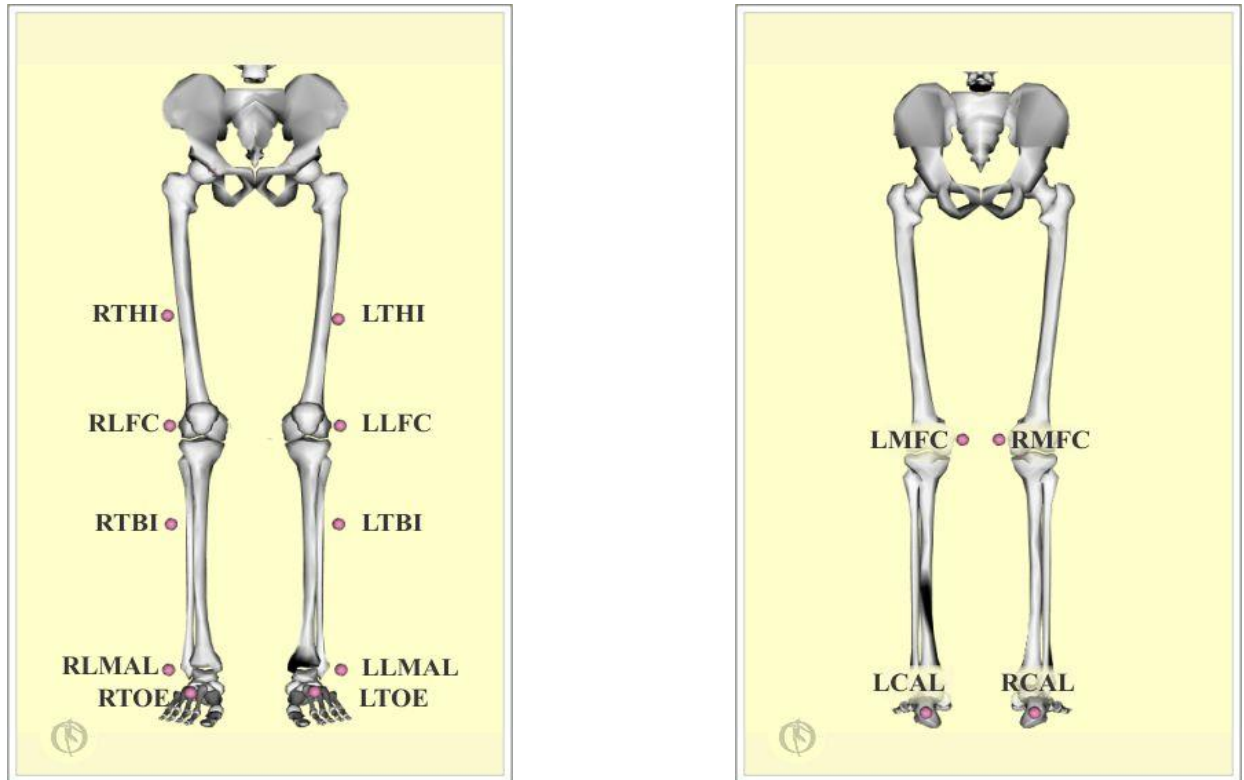


Figure 3.4 Lower body marker placement

3.1.2 Participants

The data collection involved ten healthy adults (four males and six females), with nine right-handed and one left-handed individuals. Detailed demographic information is presented in Table 3.2.

Participants had an average age of 28 years (St.D. = 8.56), an average height of 164.32 cm (St.D. = 5.69), and an average weight of 66.10 kg (St.D. = 10.48). To ensure diversity, we intentionally selected participants with limited or no prior experience with motion capture systems, including students and researchers. Ethical approval (IRB number: 004898) was obtained from the University of South Florida Institutional Review Board. Participants provided informed consent after receiving comprehensive information about the study.

Table 3.2 Subject demographic information

Subject	Gender	Dominant Hand	Height (cm)	Body Weight (Kg)
Subject 1	Male	R	162.5	60
Subject 2	Male	R	165.09	65
Subject 3	Female	R	160.02	58
Subject 4	Male	R	172.72	86
Subject 5	Female	R	152.4	58
Subject 6	Female	R	162.5	68
Subject 7	Female	R	165.09	51
Subject 8	Female	R	162.5	79
Subject 9	Male	L	172.72	60
Subject 10	Female	R	167.64	76

3.1.3 Experimental Setup

In this section, we will investigate a dataset encompassing eight ROM and four out of nine selected ADLs, in conjunction with the corresponding objects utilized to execute these activities.

3.1.3.1 Range of Motion Tasks

In this section, we will explore the ROM tasks in detail. Each task was executed under the eight Vicon cameras, with three repetitions performed for each. Subsequently, two of these demonstrations were selected for subsequent post-processing. The collected data underwent thorough post-processing using Vicon Nexus version 1.8.5, and more details can be found in Section 3.2.

The dataset encompasses eight distinct ROM tasks, as follows:

- Torso Rotation
- Torso Lateral Flexion
- Torso Flexion
- Shoulder External/Internal Rotation
- Shoulder Abduction/Adduction
- Shoulder Flexion/Extension
- Forearm Pronation/Supination
- Elbow Flexion/Extension

Each ROM task is designed to execute a fundamental rotation along a specific axis of individual body segments. When assessing torso movement, three fundamental motions are achievable by the torso: torso flexion (as illustrated in Figure 3.5), torso rotation (as shown in Figure 3.6), and torso lateral flexion (as shown in Figure 3.7). These three primary movements

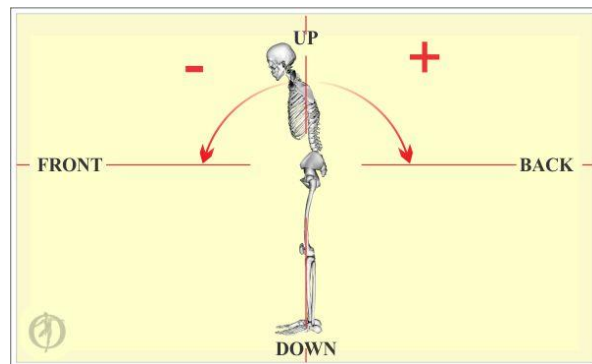


Figure 3.5 Torso flexion

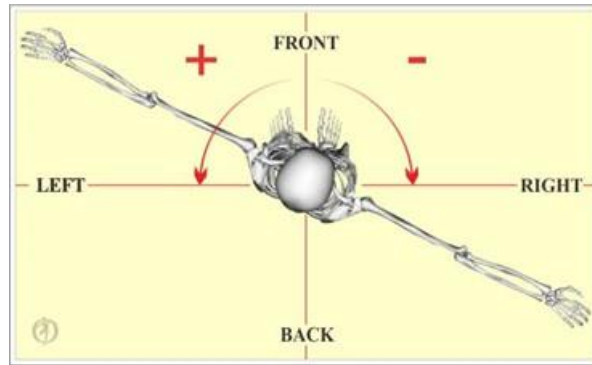


Figure 3.6 Torso rotation

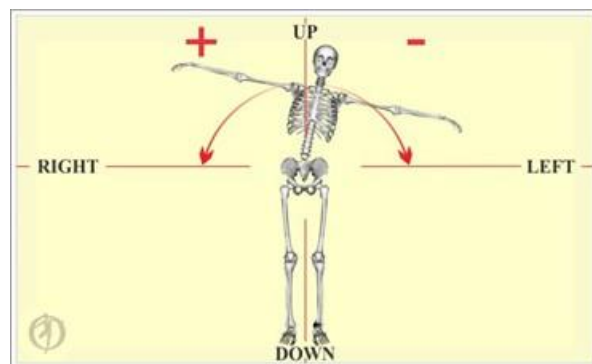


Figure 3.7 Torso lateral flexion

constitute the core motions executed by the trunk. Any other motion observed in the trunk results from a combination of these fundamental motions. It is worth noting that the direction of rotation aligns with the conventions established in [4].

The shoulder joint is considered one of the most complex joints to model due to its complex design, involving three primary motions shoulder external/internal rotation (depicted in Figure 3.8), shoulder abduction/adduction (illustrated in Figure 3.9), and shoulder flexion/extension (represented in Figure 3.10).

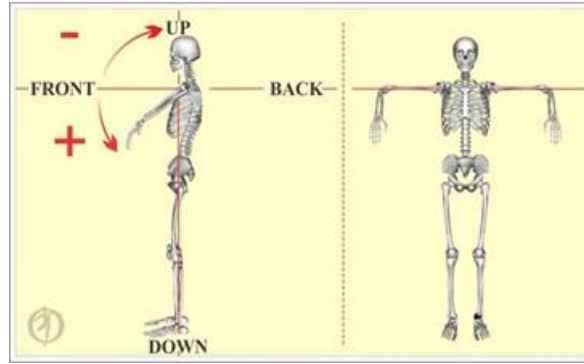


Figure 3.8 Shoulder external/internal rotation

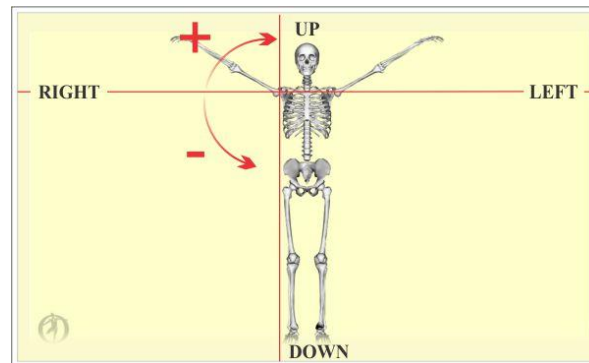


Figure 3.9 Shoulder ab/adduction

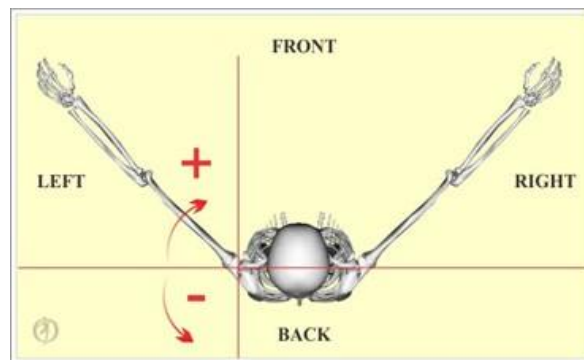


Figure 3.10 Shoulder flexion/extension

Conversely, the elbow joint exhibits two principal motions: forearm pronation/supination (depicted in 3.11) and elbow flexion/extension (as shown in 3.12). The software employed for creating visual representations of these motions was developed using OpenSim 3.3, which

incorporates the human musculoskeletal model designed by Rajagopal[101]. Additionally, image editing was conducted using Adobe Photoshop Version 2014.

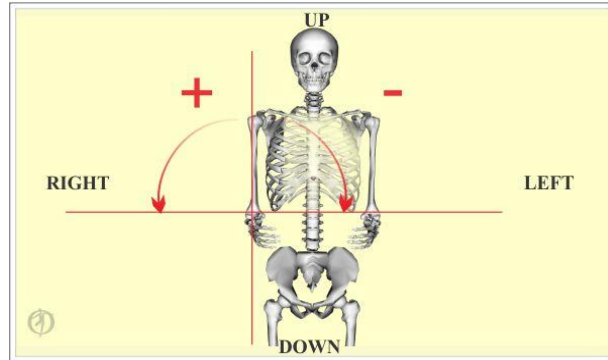


Figure 3.11 Forearm pronation/supination

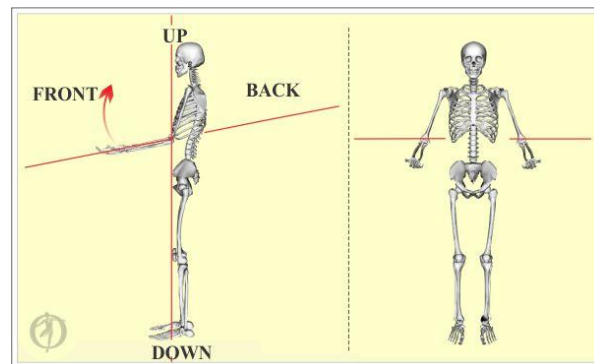


Figure 3.12 Elbow flexion/extension

3.1.3.2 Activities of Daily Living Tasks

In this research, the dataset we have collected encompasses nine distinct ADLs. However, for the purpose of this research, we will focus our analysis exclusively on four of these activities:

- Brushing Hair
- Drinking from a Cup
- Opening a Higher-Level Cabinet
- Picking Up a Full Water Jug for Shelving

The selection of these ADL tasks was based on prior research conducted by the authors of references [102-104], with a primary emphasis on upper body movements. These activities were thoughtfully chosen to highlight joint movements and explain human interactions with objects in both seated and standing positions.

Participants were given explicit instructions to execute each task while standing or seated on a chair positioned behind a table with an approximate height of 88 cm. Prior to commencing data recording, a calibration process was conducted for each participant to ensure the precise and accurate acquisition of measurements. During the recording sessions, two repetitions of each action were captured, with participants maintaining a stable and static posture at the commencement and conclusion of each trial. Detailed descriptions of each task can be found in Table 3.3.

In summary, each participant contributed 18 demonstrations for ADL activities and 16 for ROM tasks, resulting in an aggregate dataset comprising 340 demonstrations. The duration of each recorded demonstration varied within the range of five to fifteen seconds.

Table 3.3 Activities of daily living tasks.

ADL Task Name	Abbreviation	Object Used	Object Weight (Kg)	Object Size (m)
Brushing Hair	BH	Hairbrush	0.02	$0.243 \times 0.081 \times 0.0381$
Drinking From a Cup	FPC	Plastic Cup	0.02	$0.053 \times 0.053 \times 0.109$

Table 3.3 (Continued)

ADL Task Name	Abbreviation	Object Used	Object Weight (Kg)	Object Size (m)
Opening a Lower-Level Cabinet	OCL	*NA	NA	NA
Opening a Higher-Level Cabinet	OCH	NA	NA	NA
Picking Up the Box	PB	Carboard Box	0.52	$0.457 \times 0.356 \times 0.305$
Picking Up the Duster and Cleaning	PDC	Cleaning Duster	0.18	$0.356 \times 0.051 \times 0.076$
Picking Up an Empty Water Jug	PEWJ	1 Gallon Water Jug	0.90	$0.15 \times 0.15 \times 0.269$
Picking Up a Full Water Jug	PFWJ	1 Gallon Water Jug	3.79	$0.15 \times 0.15 \times 0.269$
Picking Up a Water Jug and Pouring	PWJ	1/2 Gallon Water Jug and Plastic Cup	2.55	$0.191 \times 0.105 \times 0.289$

(*NA= Not Applicable)

3.1.3.3 Objects

A curated collection of seven natural household objects was utilized to capture and analyze human motion during the execution of ADL tasks. These objects were thoughtfully chosen to closely resemble items commonly encountered in real-life scenarios, ensuring the relevance of the dataset to practical applications. Detailed specifications for each object, including their weight and

dimensions, can be found in Table 3.3. It is important to note that the data set does not incorporate information regarding markers placed on these objects.

3.2 Upper Body Model for OpenSim Model and Motion Files

Musculoskeletal models provide a non-invasive means to investigate human movement. Within the context of this dataset, we employed the comprehensive full-body musculoskeletal model initially developed by Rajagopal et al. [101] to derive subject-specific joint angles relevant to each task. Utilizing the scaling capabilities of OpenSim, we constructed personalized models replicating each individual's anatomical nuances. This intricate skeletal framework encompasses 22 articulating rigid bodies, effectively modeling the lower body, including the pelvis, femurs, patellae, tibiae/fibulae, talus, calcaneus, and toes. Similarly, the upper body is represented, encompassing the combined head and torso and the humerus, ulna, radius, and hand for both sides. This designed model comprises 20 degrees of freedom allocated to the lower body, covering the pelvis and each leg, and an additional 17 degrees dedicated to the torso and upper body, accounting for the lumbar joint and each arm. The collected data at hand offers an exhaustive array of joint angles, encompassing the entirety of the human body. However, it is imperative to emphasize that the primary focus of our research centers around the nuanced movements of the upper body, particularly during activities of daily living. Our analytical attention is directed toward the systematic examination and documentation of joint coordinates relevant to the upper body. For an in-depth understanding of each joint coordinate system, we recommend referring to the seminal work by Rajagopal et al. [101].

In our model, the head and torso merge into a single rigid segment intricately linked to the pelvis. The orientation of the torso is relative to the pelvis is described through torso fixed ZXY rotations, effectively capturing lumbar extension, lateral bending, and rotation. The connection

between the humerus and the torso is established via a ball-and-socket joint, with the orientation of the right humerus in relation to the torso determined by humerus-fixed ZXY rotations, covering shoulder flexion, adduction, and rotation, respectively. The ulna is linked to the humerus through a pivotal pin joint at the elbow, while forearm pronation is represented by a pin joint connecting the radius and ulna. The hand elegantly interfaces with the radius through a two-degree-of-freedom universal joint, with the hand's orientation relative to the radius precisely characterized by hand-fixed ZX rotations, effectively representing wrist flexion and ulnar deviation, respectively. It is essential to highlight that this model has been thoughtfully tailored to primarily capture the overarching motion dynamics of the torso and upper extremities. It does not aim to account for the intricacies of scapular motion or spinal bending, as our focus remains steadfastly attuned to upper body kinematics. The dataset is enriched with joint angles capturing the nuanced movements of the upper body during daily living activities, providing a valuable resource for in-depth biomechanical analyses and investigations.

3.3 Upper Body Model for MATLAB

In this research, the authors have exclusively provided the upper body model tailored for the MATLAB environment, building upon the foundational OpenSim model developed in the previous section. The RHUBM model was constructed using a rigid kinematic chain grounded in the Denavit-Hartenberg (D-H) parameters [105]. This model is characterized by 10 DOF attributed to each subject. These DOFs encompass three for the torso, representing lumbar lateral bending, extension, and rotation [9]. Moreover, shoulder joints have three DOFs, conscientiously accounting for shoulder flexion, adduction, and rotation. In parallel, two DOFs have been allocated to the elbow joint, effectively embodying elbow flexion and forearm pronation. Furthermore, two DOFs are ascribed to each wrist joint, defining wrist flexion and ulnar deviation. For a

comprehensive grasp of the parameters harnessed in constructing the RHUBM, please consult Table 3.4, Table 3.5 and Figure 3.13.

Within the RHUBM framework, the vertical length of the torso is designated as $D1$, while the horizontal length of the torso is denoted as $A1$. The upper arm's length is measured from the shoulder center to the elbow center, whereas the forearm length is intricately gauged from the elbow center to the wrist center. $A2$ represents the upper arm's length extending from the shoulder to the elbow center, while $D3$ aptly signifies the forearm's length. Additionally, the length of the hand, designated as $D4$, is scrupulously determined from the center of the wrist to the palm's center. It is applicable to underscore that the mass of each body segment is expressed as a percentage of the total body mass [106].

Table 3.4 Segment weight

	Weight (Kg)	Segment
W_1	$0.551 \times \text{Body Weight}$	Torso
W_2	$0.0325 \times \text{Body Weight}$	Upper Arm
W_3	$0.0187 \times \text{Body Weight}$	Lower Arm
W_4	$0.0065 \times \text{Body Weight}$	Hand

Table 3.5 D-H parameters of RHUBM model

i	α_{i-1} (deg)	a_{i-1} (m)	d_i (m)	Θ_i (deg)	Joint Name
1	0	0	0	$90 + \Theta_1$	Torso Lateral Flexion
2	90	0	0	$90 + \Theta_2$	Torso Flexion/Extension

Table 3.5 (Continued)

i	α_{i-1} (deg)	a_{i-1} (m)	d_i (m)	Θ_i (deg)	Joint Name
3	-90	0	0	$-90 + \Theta_3$	Torso Rotation
4	0	A1	D1	Θ_4	Shoulder Horizontal Flexion/Extension
5	-90	0	0	$-90 + \Theta_5$	Shoulder Abduction/Adduction
6	-90	0	D2	Θ_6	Shoulder Rotation
7	-90	0	0	$180 + \Theta_7$	Elbow Flexion
8	-90	0	D3	$90 + \Theta_8$	Elbow Pronation/Supination
9	-90	0	0	$90 + \Theta_9$	Wrist Flexion/Extension
10	-90	0	0	$180 + \Theta_{10}$	Wrist Abduction/Adduction

3.4 Post-Processed Dataset

This section comprehensively describes the essential software components supporting this study. The integral software components encompass OpenSim, the MATLAB RHUBM, and the

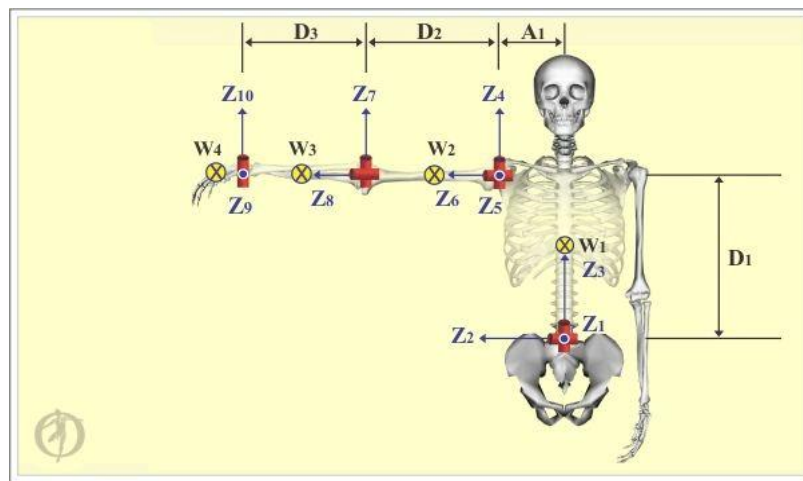


Figure 3.13 RHUBM MATLAB model

organization of the dataset. The dataset comprises a total of 426 .c3d motion files and 426 .trc files, optimized for seamless integration with OpenSim. Notably, the Demographic Data .xls file plays a crucial role, participant information, including unique identification, age, gender, dominant hand, weight, and precise body dimensions.

Table 3.6 OpenSim and MATLAB joint angles mapping information

Anatomical Joint	OpenSim Joint Angle (deg)	MATLAB Joint Angle (deg)
Torso Lateral Flexion	J1	90-J1
Torso Flexion/Extension	J2	90+J2
Torso Rotation	J3	90-J3
Shoulder Horizontal Flexion/Extension	J4	J4
Shoulder Abduction/Adduction	J5	0-J5
Shoulder Rotation	J6	180-J6
Elbow Flexion	J7	180-J7
Elbow Pronation/Supination	J8	90-J8
Wrist Flexion/Extension	J9	90-J9
Wrist Abduction/Adduction	J10	180-J10

This wealth of participant data assumes significance in creating the scaled model within OpenSim. Furthermore, the dataset encompasses seven MATLAB files, each encapsulating the RHUBM model tailored to the specific anatomical nuances of individual subjects. In addition to these files, 215 .xls joint angle files result from the comprehensive joint angle data obtained

through a one-on-one mapping process between OpenSim and MATLAB. Table 3.6 offers an extensive and detailed description of the joint angle mapping between OpenSim and MATLAB. Detailed instructions for executing the MATLAB code are provided within the accompanying text file. For a deeper understanding of the data's content and format, kindly refer to Table 3.7 [107].

Table 3.7 File formats

Dataset	Format	Number of Files
Participant Data	.trc	426
Vicon Data	.c3d	426
Matlab Raw Data	.xls	215
Matlab Code	.M	7
Demographic Data and Task Name	.xls	2

3.5 Trajectory Generation and Velocity Mapping

In this section, we explore techniques for computing a trajectory that precisely characterizes the intended motion of a hand within a given workspace. Here, "trajectory" denotes a chronological record of the hand's position and orientation. Accurate determination of the end-effector's position and orientation trajectory is crucial to adequately measuring the efficacy of diverse inverse kinematics methods. As explained in Section 3.1, a Vicon motion capture system is employed to procure reference motion data, typically encompassing an array of marker trajectories represented in cartesian coordinates. These marker trajectories undergo annotation and refinement procedures per standard motion capture protocols. Subsequently, the data undergoes post-processing through OpenSim. This entails scaling the model using a static pose dataset and

converting the obtained information into joint angle data through an inbuilt inverse kinematics algorithm, accounting for the range of feasible joint motions. The derived joint angle data is then seamlessly integrated into the subject specific RHUBM model in MATLAB via a one-to-one mapping, as explained in section 3.4. Using the forward kinematics function "fkine" from the Robotic Toolbox, the end-effector trajectory can be calculated based on the joint angles.

Once the trajectory becomes available, the manipulator end-effector's instantaneous linear and angular velocities can be calculated via inverse kinematics. Prolonged task durations coupled with a reduced number of trajectory points yield very high linear and angular velocities, which can notably impact the manipulator's overall performance. This concern can be mitigated effectively by modulating the desired velocity to attain the intended position. In this research, we have implemented an intuitive technique to manage this velocity modulation process. It involves partitioning consecutive trajectory points based on a predefined number of iterations required to reach the desired location while adhering to a linear tolerance of 1mm and a single-angle tolerance of 1 degree. This approach ensures precise control of the manipulator's movements, enhancing its performance during tasks with challenging velocity profiles.

The following discussion focuses on the discussion of velocity calculation through trajectory points and elaborates on the formula for the minimum rotation vector requisite for correcting orientation errors.

Let T_C^0 and T_T^0 denote the hand frame's current and target transformation matrices in relation to the Torso base frame, signifying the transformations undergone by the hand while transitioning from a current configuration to a target configuration.

$$T_C^0 = \begin{bmatrix} R_{11xC} & R_{12xC} & R_{13xC} & P_{xC} \\ R_{21yC} & R_{22yC} & R_{23yC} & P_{yC} \\ R_{31zC} & R_{32zC} & R_{33zC} & P_{zC} \\ 0 & 0 & 0 & 1 \end{bmatrix} \text{ and } T_T^0 = \begin{bmatrix} R_{11xT} & R_{12xT} & R_{13xT} & P_{xT} \\ R_{21yT} & R_{22yT} & R_{23yT} & P_{yT} \\ R_{31zT} & R_{32zT} & R_{33zT} & P_{zT} \\ 0 & 0 & 0 & 1 \end{bmatrix} \quad 3.1$$

The matrices T_C^0 and T_T^0 are 4x4 homogeneous transformation matrices each composed of a 3x3 matrix representing rotation and a 3x1 translation vector. Consider v as a 3x1 vector that characterizes the linear velocity of the hand frame during its transition from a starting point to a desired destination. Let ω symbolize the angular velocity. The elements v_x , v_y , and v_z denote the constituents of v , while ω_x , ω_y , and ω_z represent the elements of the angular velocity vector ω . v is the Euclidean measure of separation encompassing the individual x , y , and z components between the initial and final frames.

$$v = P_{i+1}^0 - P_i^0 \quad 3.2$$

ω can be computed by various methods in this work we used “Single Angle Single Axis” theorem to calculate desire ω_x , ω_y , and ω_z . This theorem simplifies the determination of angular velocities by focusing on a single rotation axis. It states that when a rigid body undergoes a sequence of infinitesimally small rotations about a single axis, the overall angular velocity vector can be represented by a scalar magnitude multiplied by the unit vector along that axis. Assume that the desired and current orientation matrices are R_C and R_T respectively. The orientation difference between these two matrices can be represented by

$$R_C^0 = \begin{bmatrix} R_{11xC} & R_{12xC} & R_{13xC} \\ R_{21yC} & R_{22yC} & R_{23yC} \\ R_{31zC} & R_{32zC} & R_{33zC} \end{bmatrix} \text{ and } R_T^0 = \begin{bmatrix} R_{11xT} & R_{12xT} & R_{13xT} \\ R_{21yT} & R_{22yT} & R_{23yT} \\ R_{31zT} & R_{32zT} & R_{33zT} \end{bmatrix} \quad 3.3$$

$$R_{diff} = \begin{bmatrix} r_{11} & r_{12} & r_{13} \\ r_{21} & r_{22} & r_{23} \\ r_{31} & r_{32} & r_{33} \end{bmatrix} = (R_T^0)^T R_C^0 \quad 3.4$$

The single angle representation between this rotation matrix can be calculated as,

$$\phi_{error} = \frac{\text{acos}((\text{trc}(R_{diff})-1))}{2} \quad 3.5$$

where “trc” is the trace of the rotation matrix which gives a unique solution from [0, pi].

The single axis representation can be calculated as,

$$K_1 = \frac{r_{32} - r_{23}}{2 \sin(\phi_{error})}; K_2 = \frac{r_{13} - r_{31}}{2 \sin(\phi_{error})}; K_3 = \frac{r_{21} - r_{12}}{2 \sin(\phi_{error})} \quad 3.6$$

If $\phi_{error} = 0$ then $\omega_x, \omega_y, \omega_z = 0$

This rotation vectors can be transformed to base frame as,

$$K^0 = R_C^0 \begin{bmatrix} K_1 \\ K_2 \\ K_3 \end{bmatrix} \quad 3.7$$

Angular velocities can be calculated as,

$$\begin{bmatrix} \omega_x \\ \omega_y \\ \omega_z \end{bmatrix} = \frac{\phi_{error}}{n} \cdot K^0 \quad 3.8$$

where, n is a number of steps.

3.6 Statistical Parametric Mapping

In functional mapping studies, Statistical Parametric Mapping (SPM) is a prevalent practice [109]. This technique involves creating statistical maps that facilitate the examination of hypotheses regarding regionally specific effects, such as neural activations, as initially proposed

in 1995 by [110]. These statistical parametric maps are essentially image-based representations where the voxel values adhere to predefined probability distributions under a null hypothesis assumption, typically following either Student's T or F distributions.

The conceptual simplicity of SPM is the foundational principle behind its widespread adoption. It entails thoroughly analyzing each voxel within the study area by applying various standard univariate statistical tests. The statistical parameters derived from these tests are then compiled to create a comprehensive image, termed the Statistical Parametric Map. There are different SPMs, each defined by the statistical measure they represent; for instance, SPM (T) encompasses T statistics, whereas SPM (F) represents F statistics.

These SPMs are interpreted within the framework of spatially extended statistical processes. This interpretation is grounded in the probabilistic characteristics of stationary Gaussian fields, as elucidated in the works of [109, 110] and [111]. In this context, stationary fields serve two primary functions: they model the univariate probabilistic properties intrinsic to an SPM and account for any spatial covariance structures that may be present. Deviations within the SPM deemed statistically 'unlikely' are interpreted as effects specific to a region, which can be attributed to the experimental manipulation of sensorimotor or cognitive processes. Statistical analysis in this context typically involves the application of general linear models. These models are instrumental in segregating observed neurophysiological responses into distinct categories: components of interest, confounding variables, and errors.

Expanding upon its applications, Statistical Parametric Mapping is an advanced analytical framework extensively used in diverse scientific fields, particularly in analyzing data in medical imaging and kinematics domains. Conceptualized initially for 2D medical imaging[110] and subsequently adapted for 1D data sets[112], SPM is adept at discerning variances within signal

vectors, employing a dynamically varying 't-statistic'. In its operational methodology, SPM perceives signal data points as elements of a continuously evolving vector trajectory over time. When it comes to the analysis of multiple signals, SPM treats these as vector fields in a temporal context. This unique approach facilitates granular analysis, generating new vectors over time intervals, each marked by t-test values corresponding to each point in time. This allows for a more intricate comparison of multiple signals or factors.

Unlike traditional methods that tend to group data into a single summary statistic, SPM thoroughly analyzes the entire spectrum of data trajectories[113]. This characteristic is particularly advantageous when comparing multiple factors or criteria, each characterized by linear and angular components. SPM aids in pinpointing the most influential criterion in motion dynamics. It does this by normalizing the magnitudes of each criterion within a zero to one range and then employing statistical tests to determine which criterion most significantly dictates human motion during specific task phases. For further exploration and understanding, readers are encouraged to refer to[113, 114], as well as to access the SPM library in Python for practical applications and examples.

3.7 Motion Analysis

3.7.1 Motion Analysis of the Range of Motion Task

The study included eight healthy subjects from the original group of ten participants. The selection process involved excluding one left-handed subject, as the primary focus of the study revolved around right-handed subjects. Additionally, one right-handed subject was omitted from the analysis due to modeling errors encountered within the OpenSim software about that specific individual. The subject selection process aimed to ensure accurate and reliable outcomes while maintaining consistency and homogeneity in the sample population for investigating ROM tasks.

ROM for each joint is defined as the difference between the maximum and minimum joint angles. Table 3.8 displays the average maximum and minimum joint angles across all participants and the corresponding standard deviation. The determination of positive and negative joint angle limits is based on the extremes of joint motion, a crucial aspect for the successful implementation of the inverse kinematics algorithm and the enforcement of joint constraints.

Table 3.8 Motion analysis of the range of motion task

Anatomical Joint	Max (deg)		Min (deg)		ROM (deg)	
	AVG	St.D	AVG	St.D	AVG	St.D
Torso Lateral Flexion	135.1712	7.4867	50.8212	6.6131	84.3500	11.32844
Torso Flexion/Extension	116.2121	9.8777	13.7721	18.7245	102.4400	21.9296
Torso Rotation	341.0512	194.3625	-75.6400	19.0540	146.6900	27.9603
Shoulder Horizontal Flexion/Extension	120.0010	11.3591	-74.4600	21.8987	194.4600	25.1216
Shoulder Abduction/Adduction	-5.0000	15.2824	-150.000	11.0106	145.0000	21.7313
Shoulder Rotation	269.9102	160.1101	-89.9100	10.8121	109.8000	11.2967
Elbow Flexion	165.0000	6.3519	40.0000	0.2899	125.0000	6.4453
Elbow Pronation/Supination	150.0000	12.4032	-89.0000	1.0001	179.0000	14.2743
Wrist Flexion/Extension	160.0021	2.4328	-64.7900	25.2101	124.7900	5.6068
Wrist Abduction/Adduction	205.0001	5.5066	170.0000	1.9224	35.0000	6.4664

The Range of Motion of a joint is influenced by subject anthropometrics and variability in marker placement, where even slight differences in marker positions can result in offsets in coordinate frames. To mitigate this variability, the experimental protocol followed marker

placement, and photos were taken to assist in marker positioning during post-processing in OpenSim. This approach enhances the accuracy of marker placement on the OpenSim model, subsequently reducing the marker Root Mean Square (RMS) error during the scaling algorithm. After completing Range of Motion Task simulations in OpenSim, joint angles are exported to a subject-specific MATLAB model.

3.7.2 Motion Analysis of the Brushing Task

Table 3.9 Motion analysis of the brushing task

Anatomical Joint	Max (deg)		Min (deg)		ROM (deg)	
	AVG	St.D	AVG	St.D	AVG	St.D
Torso Lateral Flexion	92.9871	4.6528	76.7012	5.8589	16.2858	3.9006
Torso Flexion/Extension	89.9588	6.4913	82.5520	5.3611	7.4068	2.7929
Torso Rotation	278.4781	4.8484	264.9884	2.7244	13.4897	5.2331
Shoulder Horizontal Flexion/Extension	70.8075	5.1096	4.7518	15.8307	66.0556	16.9889
Shoulder Abduction/Adduction	-25.3899	5.8593	-92.4489	11.4990	67.0590	15.6257
Shoulder Rotation	233.4689	21.0547	161.1271	1.1897	72.3417	20.2676
Elbow Flexion	142.5483	16.8005	50.9948	2.1107	91.5533	17.7438
Elbow Pronation/Supination	109.7922	17.1225	52.6934	19.8987	57.0988	11.5220
Wrist Flexion/Extension	146.2926	21.9136	90.7950	37.0379	55.4975	23.7005
Wrist Abduction/Adduction	197.3187	7.5365	172.3930	2.0823	24.9256	6.7773

The MATLAB model offers flexibility for implementing various kinematic algorithms and streamlines work with MoCap. This enables the measurement of joint Range of Motion for subsequent sections, thereby contributing to effective joint limit avoidance strategies.

The "Brushing Hair" task encompasses five distinct phases (P1-P5), each contributing to the overall motion. These phases include the initiation of motion from the resting pose to obtaining the hairbrush (P1), guiding the brush toward the head (P2), combing through a section of hair (P3), placing the brush back on the table (P4), and finally returning to the initial posture (P5) as shown in Figure 3.14.

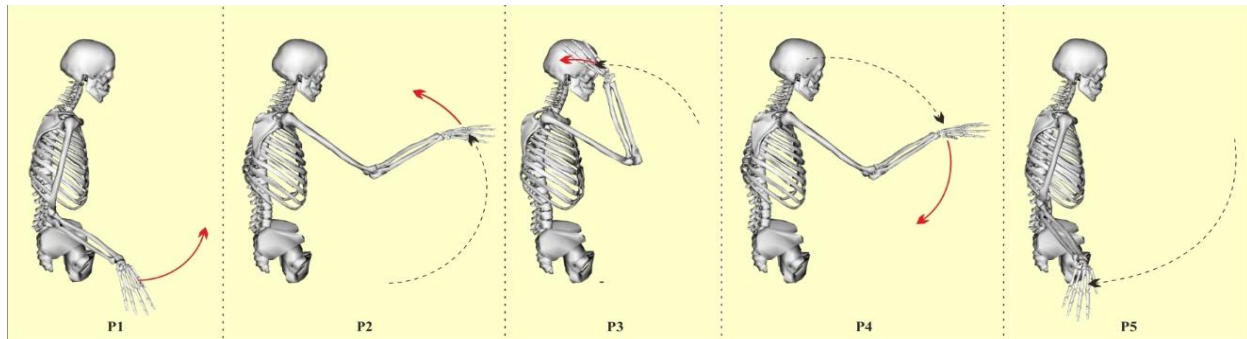


Figure 3.14 Phases of the brushing task

Table 3.9 provides a comprehensive overview of the absolute average ROM data obtained from the eight subjects participating in the task. It presents numerical values for the average maximum angle, minimum angle, absolute average ROM, and the corresponding standard deviations for each of these motion phases. The analysis of this data reveals that elbow flexion plays a central role in executing the task and exhibits consistent usage across all subjects. The average ROM for elbow flexion is calculated to be 91.5533 degrees with a standard deviation of 17.7438 degrees. Furthermore, the motions of the sternoclavicular joint and the shoulder also contribute significantly to task execution. It is noteworthy that the shoulder and wrist motions exhibit relatively high standard deviations, indicating inter-subject variation in posture.

Despite the variability in shoulder and forearm motions, a notable convergence exists in the kinematic strategy employed by able-bodied subjects to accomplish the "Brushing Hair" task. Wrist movements come into play once the brush reaches the head, facilitating precise positioning.

The torso maintains a relatively stationary position throughout the task to sustain an upright posture. In essence, the shoulder complex and the forearm collectively bear the primary workload, with the wrist contributing fine adjustments as needed.

3.7.3 Motion Analysis of the Drinking from a Cup Task

Table 3.10 Motion analysis of the drinking from a cup task

Anatomical Joint	Max (deg)		Min (deg)		ROM (deg)	
	AVG	St.D	AVG	St.D	AVG	St.D
Torso Lateral Flexion	93.7981	5.3910	80.9618	4.7051	12.8362	3.6358
Torso Flexion/Extension	90.5921	4.0173	85.9159	3.1162	4.6762	1.2058
Torso Rotation	277.6499	4.9856	268.4833	4.1253	9.1666	2.6005
Shoulder Horizontal Flexion/Extension	67.9502	5.3825	1.7810	19.8471	66.1692	17.1042
Shoulder Abduction/Adduction	-29.1256	8.5323	-66.5396	8.9644	37.4140	9.0614
Shoulder Rotation	201.0171	24.6208	160.7752	0.8271	40.2419	24.1450
Elbow Flexion	141.0105	16.6338	50.3020	0.5886	90.7085	16.7046
Elbow Pronation/Supination	82.7843	19.1250	54.5901	16.6377	28.1932	6.3769
Wrist Flexion/Extension	146.8197	17.5617	112.2965	36.5186	34.5231	20.5783
Wrist Abduction/Adduction	201.0802	3.8224	171.9556	2.3760	29.1245	4.0340

The "Drinking from a Cup" task comprises a sequence of actions divided into five distinct phases (P1-P5), as illustrated in Figure 3.15. Each phase involves specific steps: initiating the task by grasping the glass from a resting pose (P1), bringing it to the mouth (P2), performing the drinking action (P3), returning the glass to the table (P4), and ultimately returning to the initial posture (P5).

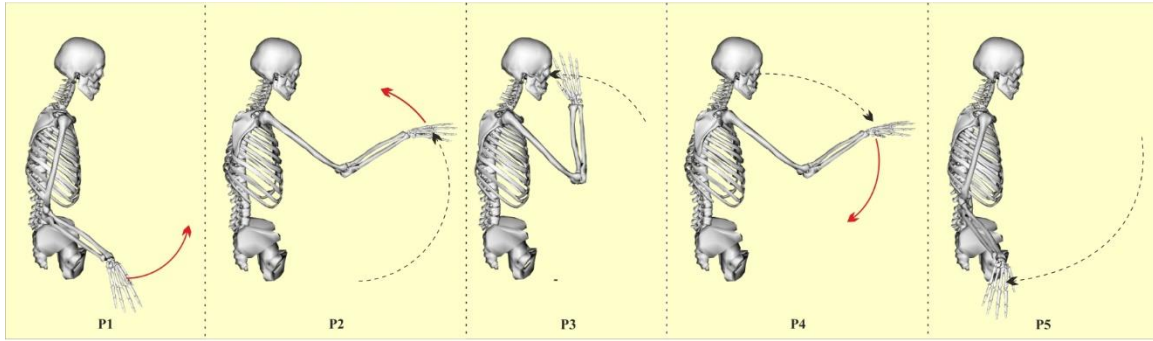


Figure 3.15 Phases of the drinking task

In this task, the full ROM is not fully utilized due to limited joint motion in some joints. Table 3.10 provides a comprehensive summary of the absolute average ROM data obtained from the eight participants involved in the task. Analysis of this dataset reveals that certain joint angles exhibit a smaller ROM during this task. The elbow flexion/extension ROM is 90.7085 degrees with a standard deviation of 16.7046 degrees, less than the "Brushing Hair" task. This is because the "Drinking from a Glass" task involves moving the cup towards the mouth, requiring less upper limb motion compared to the "Brushing Hair" task, where the hand must reach behind the head for specific hair sections. Similarly, the shoulder and wrist joints employ less ROM. Throughout the task, wrist motions show minimal deviation, except during phase 3, where users utilize maximum wrist deviation to control the glass's orientation for drinking. In other phases, the wrist is primarily used to maintain the cup's orientation while moving it toward the mouth and during the drinking action in phase 3.

3.7.4 Motion Analysis of the Opening a Higher-Level Cabinet Task

Throughout the process of Opening a Higher-Level Cabinet Task, a sequence of movements occurs, divided into four distinct phases (P1-P4). These phases involve actions such as initiating the reach to grasp the door handle or knob from the initial resting position (P1),

exerting force to pull the door open (P2), applying force to push the door closed (P3), and ultimately start returning to a neutral posture (P4) as illustrated in Figure 3.16.

Table 3.11 Motion analysis of the opening a higher-level cabinet task

Anatomical Joint	Max (deg)		Min(deg)		ROM (deg)	
	AVG	St.D	AVG	St.D	AVG	St.D
Torso Lateral Flexion	94.3876	6.1405	86.9805	1.7421	7.4070	2.1474
Torso Flexion/Extension	92.5270	6.4557	86.5440	6.0890	5.9830	2.0489
Torso Rotation	280.9229	2.9163	270.23	2.0176	10.6929	0.9253
Shoulder Horizontal Flexion/Extension	76.0654	4.2722	5.9600	22.3797	70.1053	24.4226
Shoulder Abduction/Adduction	-33.9003	19.9706	-111.7141	2.0905	77.8135	19.4120
Shoulder Rotation	223.1287	18.4582	160.8850	1.6860	62.2437	16.7956
Elbow Flexion	136.0749	9.5189	77.0953	11.5983	58.9795	9.2068
Elbow Pronation/Supination	125.9726	15.3491	38.5136	19.3433	87.4590	12.6715
Wrist Flexion/Extension	149.6863	16.2666	88.3870	49.7255	61.2993	40.9176
Wrist Abduction/Adduction	199.3437	10.4904	181.4283	9.6427	17.9153	9.7861

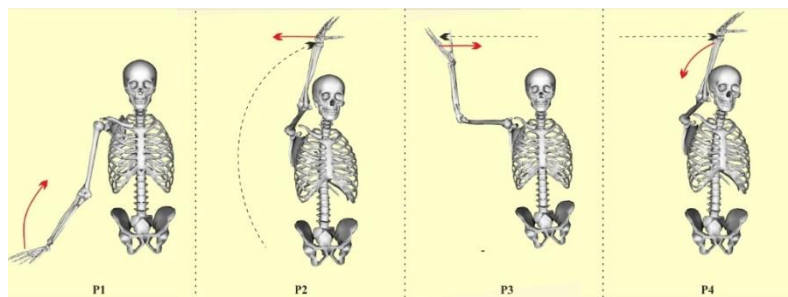


Figure 3.16 Phases of the opening a higher-level cabinet task

In this task, some joints fully utilize their ROM, particularly in Phase 1, Phase 2, and Phase 3, where the complete range of motion is engaged. Table 3.11 provides a comprehensive summary of the absolute average ROM data obtained from the participation of eight subjects in this task. An analysis of this dataset reveals that specific joint angles exhibit a greater ROM during this task, specifically shoulder adduction 77.8135 with a standard deviation of 19.4120, shoulder rotation 62.2437 with a standard deviation of 16.7956, shoulder abduction 70.1053 with a standard deviation of 24.4226, and elbow pronation 87.4590 with a standard deviation of 12.6715. Interestingly, minimal torso movement occurs during the task. Conversely, the elbow flexion 58.9795 with a standard deviation of 9.2068 employ less ROM.

Despite variations in shoulder movement, a remarkable convergence is evident in the kinematic strategy employed by subjects to complete the "Opening a Higher-Level Cabinet" task. The majority of the work is carried out by the shoulder joint, guiding the hand to grasp the doorknob and facilitating the cabinet's opening. Elbow pronation plays a significant role in precise door closure once the task is completed. The torso maintains a relatively stable position throughout the task to support an upright posture. Essentially, the shoulder complex bears the primary workload, with the forearm making fine adjustments as necessary.

3.7.5 Motion Analysis of the Picking Up a Full Water Jug for Shelving Task

Table 3.12 Motion analysis of the picking up a full water jug for shelving task

Anatomical Joint	Max (deg)		Min (deg)		ROM (deg)	
	AVG	St.D	AVG	St.D	AVG	St.D
Torso Lateral Flexion	101.7187	7.1485	80.5691	3.5717	21.1496	6.8632
Torso Flexion/Extension	101.3732	6.0786	88.0551	3.9426	13.3181	5.2639
Torso Rotation	281.8088	5.9667	268.5864	3.5406	13.2224	4.6415

Table 3.12 (Continued)

Shoulder Horizontal Flexion/Extension	68.8489	8.1686	-17.9553	17.5971	86.80422	17.4504
Shoulder Abduction/Adduction	-19.1855	5.8792	-112.709	13.4929	93.5238	13.0406
Shoulder Rotation	214.6975	15.9405	170.3616	6.7353	44.3359	17.9643
Elbow Flexion	144.2281	15.8029	57.7664	4.4653	86.4617	12.2053
Elbow Pronation/Supination	107.8713	23.9759	56.9126	9.8374	50.9586	22.9747
Wrist Flexion/Extension	158.8759	0.4472	133.1903	21.4228	25.6856	21.0272
Wrist Abduction/Adduction	201.7639	4.9841	178.3423	5.9912	23.4216	5.5598

The Picking Up a Full Water Jug for Shelving task comprises four distinct phases (P1-P4), each involving specific actions: object acquisition (P1), bringing the object closer to the body to facilitate lifting (P2), lifting the object and positioning it on the shelf (P3), and returning to the initial posture (P4) as illustrated in Figure 3.17.

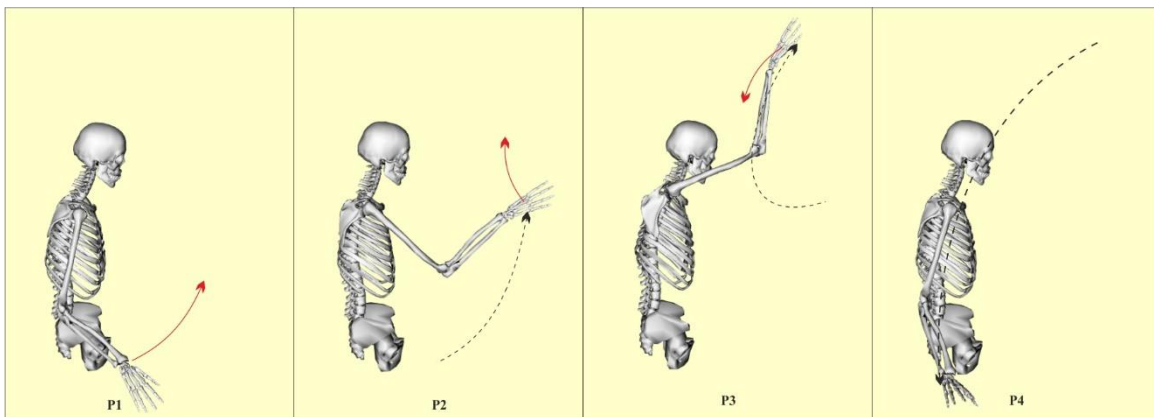


Figure 3.17 Phases of the picking up a full water jug for shelving task

Table 3.12 provides a comprehensive summary of the absolute average ROM data obtained from the eight participants participating in the task. Analysis of this dataset reveals that

the full ROM is primarily utilized in the shoulder adduction 93.5238 with a standard deviation of 13.0406 and elbow flexion 86.4617 with a standard deviation of 12.2053 joints during Phase 1 and Phase 2, which involve the grasping and lifting of heavy water jug. Wrist flexion and adduction exhibit minimal movement to maintain balance when handling the heavy object, with more noticeable movement occurring when placing the heavy object on the shelves.

Despite variations in shoulder movement, a notable convergence is evident in the kinematic strategy employed by subjects to complete the "Picking Up a Full Water Jug for Shelving" task. Most of the work is carried out by shoulder adduction and elbow flexion, both crucial for maintaining balance and accomplishing the task without undue strain on the joints and muscles. The torso maintains a relatively stationary position throughout the task to support an upright posture. Essentially, the shoulder complex shoulders the primary workload, with the elbow and wrist contributing fine adjustments as necessary.

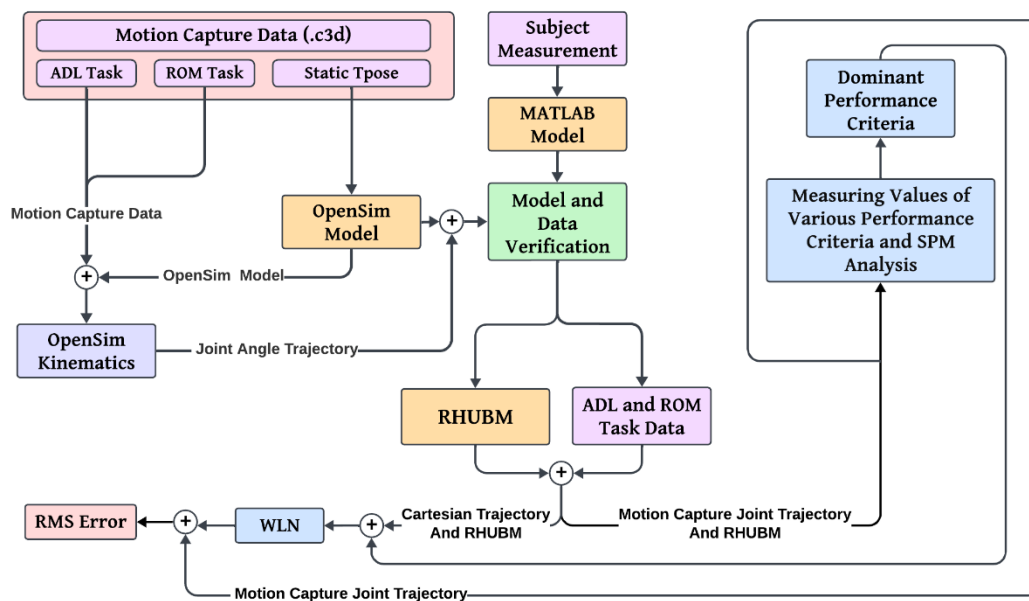


Figure 3.18 Flowchart of the data flow during the development of the RHUBM

Chapter 4: The Method and Results of Evaluating the Influence of Arm Configurations on Various Performance Criteria

Building upon a literature review outlined in Section 2, this research emphasizes four essential performance criteria: Manipulability, the Norm of the Gravity and Payload Torques, Velocity Ratio, and Mechanical Advantage. The optimization objective for human arm motion encompasses the simultaneous maximization of three criteria: Manipulability, Velocity Ratio, and Mechanical Advantage, while concurrently minimizing the Norm of the Gravity and Payload Torques. These criteria hold paramount importance when evaluating the efficiency and effectiveness of the human arm across various contexts [58, 74, 94, 95]. They encapsulate the arm's capacity to move optimally in all spatial directions, apply the requisite force for task execution, and account for joint load-bearing capabilities.

To investigate whether human motion results from optimizing a single criterion or a combination of multiple criteria and to explore the diverse performance criteria that influence the choice of particular arm configurations by humans during various ADLs, the application of null space projection was required. Specific Cartesian positions along the motion trajectory were thoughtfully selected to induce modifications in arm configuration while maintaining a constant hand position. This systematic selection process was designed to encompass various arm postures and orientations. Starting from the baseline natural human arm configuration (N), three distinct right-side arm configurations (C, D, E) were chosen. Notably, the third right-side configuration was deliberately oriented in proximity to the horizontal plane, aligning with specific ADLs.

Furthermore, two arm configurations (A, B) on the left side were thoughtfully selected, also derived from the natural arm configuration.

This systematic and thoughtful approach involved a diverse arm posture within the null space, thereby providing a comprehensive spectrum of configurations for analysis. Each chosen configuration was strategically selected based on well-defined rationales tied to potential arm movements during ADLs. By accounting for these factors, researchers can collect valuable insights into the human arm's performance strategies across a wide spectrum of ADL. This section uses the following acronyms for performance criteria: Linear Manipulability (LM), Angular Manipulability (AM), Velocity Ratio (VR), Linear Velocity Ratio (LVR), Angular Velocity Ratio (AVR), Mechanic Advantage (MA), Linear Mechanical Advantage (LMA), Angular Mechanical Advantage (AMA) and Norm of the Gravity and payload torques (GL).

4.1 Brushing Task

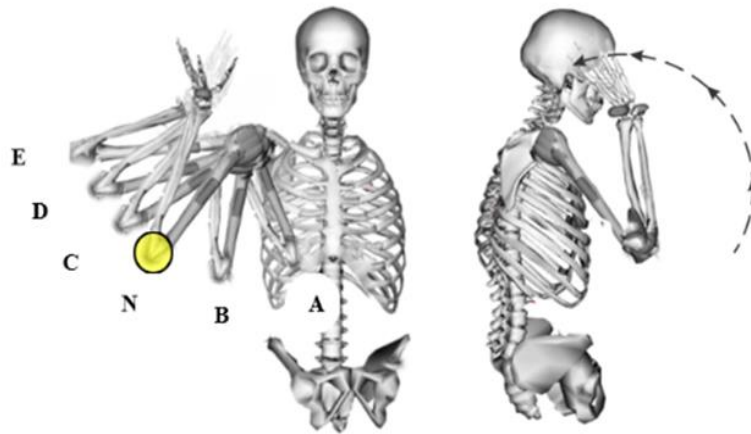


Figure 4.1 Brushing task

The task of brushing entails a sequence of motions that initiate with the initial action of reaching out to grasp the hairbrush, which has an approximate weight of 0.02 kg. Subsequently,

the brush is brought into proximity with the head, followed by its maneuvering through a section of the hair, concluding with its return to the table, as illustrated in Figure 3.14

Table 4.1 Results of brushing task

Performance Criteria	A	B	N	C	D	E
LM	0.1639	0.1528	0.1173	0.1279	0.1355	0.1456
AM	5.7293	5.7746	5.9984	5.9755	5.8936	5.7710
LVR	0.0329	0.0352	0.0407	0.0401	0.0380	0.0336
AVR	0.2302	0.2464	0.2848	0.2805	0.2659	0.2353
LMA	0.1299	0.1302	0.1275	0.1293	0.1290	0.1202
AMA	0.0672	0.0675	0.0674	0.0674	0.0673	0.0672
GL	30.6787	24.4946	26.4871	29.8950	35.5517	41.3849

Maximum Value Minimum Value

A comprehensive examination of intricate movements necessitated the adoption of six distinct arm postures in close proximity to the head. These postures were strategically selected to enable precise measurement of each performance criterion's values during task execution. Figure 4.1 presents a detailed trajectory of these motions, with quantitative outcomes summarized in Table 4.1.

The task of brushing involves a sequence of motions starting with reaching for the hairbrush, weighing approximately 0.02 kg, followed by positioning it near the head, maneuvering through the hair, and returning it to the table, as depicted in Figure 3.14. Throughout the hair brushing task, participants naturally incline towards arm postures that inherently aim to minimize

LM within the context of the natural arm configuration. This observed tendency underscores a conscious effort to prioritize arm configurations that mitigate excessive LM. By doing so, participants effectively enhance the stability of arm motion, a crucial factor in ensuring the task's successful execution. The deliberate emphasis on reducing LM aligns with the objective of achieving steady and controlled movements during the hair brushing activity.

In contrast, when considering AM, LVR, and AVR, a different preference emerges. Participants seek to maximize these parameters within the natural human arm pose while simultaneously striving to minimize them when transitioning to alternative arm configurations. This preference signifies a conscious choice aimed at optimizing AM, elevating LVR, and promoting smoother and more controlled brushing actions. These actions are critical in reducing the likelihood of hair tangling or discomfort during the hair brushing task.

Furthermore, it becomes evident that participants consistently select arm configurations that result in a GL greater than the minimum threshold during the hair brushing task. This decision reflects a careful equilibrium between minimizing joint and muscle strain, as indicated by observations related to LMA and AMA ensuring a certain level of arm stability and control throughout the hair brushing process. The strategic balance between these factors serves to facilitate efficient force transmission while preventing undue physical strain.

The results collected from this investigation underscore the deliberate and strategic choices made by participants when configuring their arms. These choices prioritize stability, motion efficiency, and force transmission optimization, all while minimizing the potential for joint and muscle strain during the hair brushing task. This strategic approach highlights the intricate interplay and adaptability inherent in human arm motion when executing specific tasks, shedding light on the decision-making processes underlying such actions.

4.2 Drinking from a Cup Task

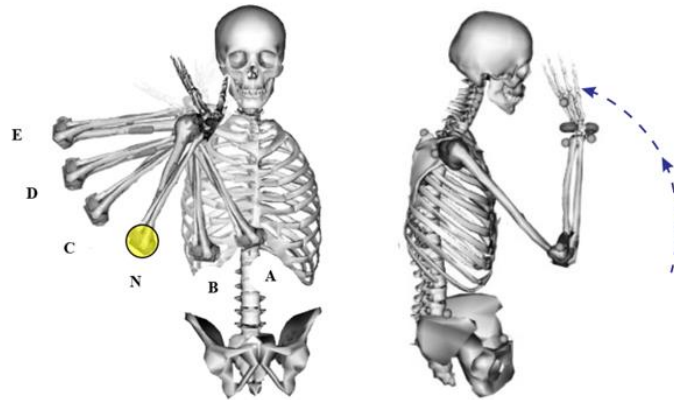


Figure 4.2 Drinking from a cup task

Table 4.2 Results of drinking from a cup task

Performance Criteria	A	B	N	C	D	E
LM	0.1119	0.1023	0.0913	0.0952	0.0970	0.1033
AM	5.8842	5.86915	5.8508	5.8499	5.8651	5.8711
LVR	0.12915	0.12045	0.1095	0.1165	0.1240	0.1427
AVR	0.50725	0.49735	0.4704	0.4879	0.5067	0.5718
LMA	2.2613	2.3412	2.3547	2.3473	2.34025	2.3283
AMA	0.2422	0.25655	0.27255	0.26455	0.2529	0.2502
GL	21.49885	17.1468	16.3253	18.2734	22.6801	25.2903



Maximum Value



Minimum Value

The task of drinking from a cup result in a sequence of coordinated movements that involve grasping the cup, bringing it to the mouth for liquid consumption, and subsequently returning it to its initial position, as visually depicted in Figure 3.15. The trajectory illustrating these well-

orchestrated motions, in combination with the deliberate utilization of six distinct arm postures in close proximity to the mouth, aimed at enabling the measurement of performance criteria values at an instance of the task, is presented in Figure 4.2. To offer a comprehensive and quantitative assessment of the task's execution, the results have been compiled and are presented in Table 4.2. This table serves as a concise summary, encapsulating the measured values associated with various performance criteria.

Ensuring the efficiency and stability of arm movements plays a critical role in mitigating the risk of spillage and accidents during the act of drinking from a glass. Observations drawn from natural arm movements reveal a pronounced inclination to prioritize the minimization of Manipulability, LVR, AVR and GL throughout the task, while concurrently endeavoring to maximize LMA, AMA. In contrast, alternative hand configurations within the null space exhibit different outcomes in these performance criteria.

Pursuing lower values in Manipulability, LVR, AVR, and GL underscores the human arm's innate ability to execute movements with heightened efficiency, a paramount property for maintaining stability throughout the task. This emphasizes the critical significance of speed and efficiency in accomplishing the drinking task. Maximizing LMA, AMA augments the arm's load-carrying capacity in the direction of motion and reinforces its stability by adeptly balancing forces and torques. Consequently, this strategic emphasis on LMA, AMA mitigates the undue strain imposed on joints and muscles, ultimately fostering greater efficiency and stability in task performance. Furthermore, a concerted effort minimizes the GL experienced during the task. This strategic approach, which maximizes LMA, AMA and minimizes GL, effectively curtails the joint load induced by gravitational forces. As a result, it engenders a more controlled and balanced

performance at specific junctures along the trajectory, thus contributing to overall task efficiency and stability.

This strategic approach explains the relationship and inherent adaptability within human arm motion while drinking from a cup. It offers insights into intricate decision-making processes governing these actions, framed by diverse performance criteria. This equilibrium develops our understanding of the interplay between efficiency, stability, and force management during the task, underscoring the adaptability of human arm motion. It highlights complex decision-making processes optimizing various performance criteria.

4.3 Opening a Higher-Level Cabinet Task

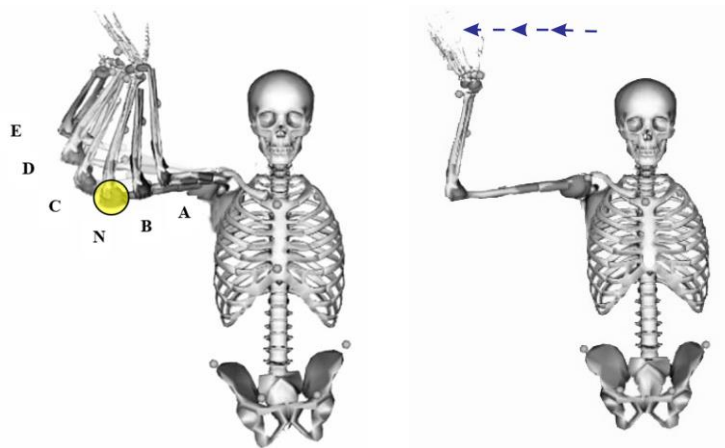


Figure 4.3 Opening a higher-level cabinet task

To initiate the process of opening a cabinet door, participants engage in a sequence of well-coordinated movements that encompass reaching out to grasp the door handle or knob, subsequently either pulling it towards themselves or pushing it away as shown in Figure 3.16. Within the context of assessing these dynamic actions throughout the cabinet door-opening task, a selection of six distinct arm postures was employed at a specific point in the task sequence.

Table 4.3 Results of opening a higher-level cabinet task

Performance Criteria	A	B	N	C	D	E
LM	0.1687	0.1785	0.1812	0.1951	0.2086	0.2199
AM	5.9728	5.9765	5.9767	5.9714	5.9596	5.9471
LVR	0.0285	0.0263	0.0291	0.0314	0.0319	0.0321
AVR	0.2703	0.2496	0.2757	0.2974	0.3022	0.3024
LMA	0.0564	0.0586	0.0587	0.0577	0.057	0.0565
AMA	0.0446	0.0451	0.0458	0.0456	0.0453	0.0450
GL	22.9313	18.0377	15.5979	17.1150	19.4053	26.7757

Maximum Value Minimum Value

Figure 4.3 offers a visualization of the trajectory and arm configurations associated with these movements, while the summarized task results are detailed in Table 4.3.

In the specific context of the cabinet door-opening task, the natural arm configuration shows with a distinctive profile marked by an evident emphasis on the maximization of AM, LMA and AMA. The increase of AM significantly contributes to the precision and dexterity required for manipulating the door handle, ultimately playing a central role in ensuring the successful execution of the task.

Furthermore, both LMA and AMA reach their top value in close proximity to the natural arm pose. Elevated LMA and AMA values inherently signify a heightened efficiency in the arm's load-carrying capacity, particularly in the direction of motion. Consequently, this optimization facilitates smoother and more controlled door-opening motions. Conversely, participants consistently tend to minimize GL within the natural arm pose during the task. This strategic

approach underscores a deliberate attempt to limit the influence of gravitational forces acting upon the arm and hand, consequently enhancing the flexibility of movement and reducing potential muscle and joint strain, all while maintaining stability throughout the door-opening endeavor.

In summation, these findings illuminate the participants' proficiency in adapting to a diverse array of performance criteria tailored to the complexities of the cabinet door-opening task. The selection of arm configurations at specific junctures along the task trajectory emphasizes the maximization of AM, LMA, and AMA while concurrently striving to minimize GL. The precise fine-tuning of arm movements underscores the participants' innate capacity to seamlessly adapt to the unique demands of door-opening tasks, seamlessly integrating performance criteria.

4.4 Picking Up a Full Water Jug for Shelving Task

The task of Picking Up a Full Water Jug for Shelving takes a series of intricate motions, involving actions such as reaching, grasping, and placing objects of substantial weight (approximately 3.5 kg) at predefined locations on a shelf as shown in Figure 3.17. An examination of these motions entails the deliberate selection of six mid-air arm postures, strategically chosen to facilitate the measurement of performance criteria at various task-specific locations. The orchestrated trajectory of these motions is visually depicted in Figure 4.4, while the resulting quantified data is thoughtfully presented in Table 4.4.

Within the domain of the shelving task, the natural arm configuration exhibits a distinctive profile characterized by a distinct emphasis on the maximization of LVR, AVR and AM. This emphasis is complemented by a concerted effort to minimize LM, LMA, AMA, and GL. The deliberate drive towards LM minimization within the natural arm pose signifies a strategic choice aimed at mitigating excessive LM. This calculated decision aligns with the overarching objective

of enhancing overall arm motion stability and control during the task, especially when engaged in the placement of weighty objects onto a shelf.

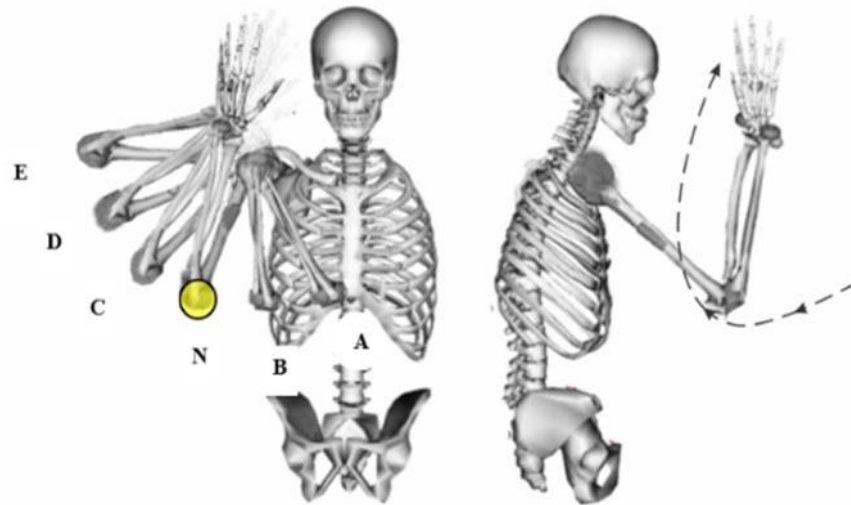


Figure 4.4 Picking up a full water jug for shelving task

Table 4.4 Results of picking up a full water jug for shelving task

Performance Criteria	A	B	N	C	D	E
LM	0.2305	0.1835	0.1657	0.1814	0.1998	0.2186
AM	5.969	5.9817	6.0150	6.0088	5.9856	5.9557
LVR	0.0665	0.0672	0.0812	0.0674	0.0645	0.06438
AVR	0.1525	0.1714	0.1848	0.1533	0.1467	0.1452
LMA	0.1541	0.1542	0.1544	0.1544	0.155	0.1709
AMA	0.0613	0.0668	0.0736	0.0759	0.078	0.0797
GL	39.9283	28.8917	25.6563	34.6300	32.5149	38.9838

Maximum Value Minimum Value

Conversely, participants display a propensity for maximizing AM values within the natural arm pose while concurrently seeking to minimize AM in alternative arm configurations. The prioritization of higher AM values within the natural arm pose underscores a deliberate endeavor to optimize angular movements, with a particular focus on achieving precise object orientation and accurate placement during the shelving task.

Furthermore, both LVR and AVR reach their high point in close proximity to the natural arm pose. These elevated LVR and AVR values signify the attainment of smoother and more rapid motions, imparting distinct advantages in achieving precise object placement while simultaneously reducing the physical exertion required. Throughout the shelving task, participants consistently engaged in the minimization of GL within the natural arm pose. This strategic choice reflects a conscious endeavor to mitigate the influence of gravitational forces acting upon the arm and hand, enhancing movement flexibility and alleviating muscle and joint strain potential. This approach ensures the sustained maintenance of stability throughout the task.

These findings shed light on the deliberate selection of arm configurations that prioritize stability, motion efficiency, and precise force application at specific junctures along the trajectory associated with shelving heavy objects. This is achieved by strategically maximizing AM, LVR, and AVR while concurrently minimizing GL, effectively reducing strain on joints and muscles. This strategic approach underscores the adaptability of participants in finely calibrating various performance criteria to address the unique demands posed by the task of shelving.

4.5 Summary

This section underscores the importance of conducting a systematic assessment of a diverse range of performance criteria within the context of participants engagement in ADLs. To attain a comprehensive understanding of human arm motion, it is essential to determine the combination

of performance criteria that individuals prioritize while participating in these tasks. Simultaneously, the observation of how the values of these performance criteria evolve in response to variations in arm configurations yields invaluable insights into the complex nature of human motion. A consistent trend emerges across three distinct tasks, namely "Drinking from a Cup," "Opening a Higher-Level Cabinet," and "Picking up a Full Water Jug for Shelving." In each of these tasks, a persistent effort is observed to minimize the influence of GL, except for the "Brushing" task, where this trend deviates due to task-specific requirements. This consistent pattern of behavior indicates an inclination of participants to actively reduce the loads imposed on both joints and muscles during the execution of these tasks. These insights significantly enhance our understanding of the optimization strategies that participants employ. Furthermore, they provide robust empirical evidence in support of the hypothesis that humans possess a remarkable capacity to effectively integrate multiple performance criteria, demonstrating the precision with which they can fine-tune these criteria to align with the distinctive demands imposed by specific tasks.

In the subsequent chapter, the significance of distinct performance criteria at various phases of the task will be established through the collection and comprehensive analysis of motion data. These findings provide invaluable insights into the domain of motor control, developing our understanding of the complex nature of human arm motion in the context of ADLs.

Chapter 5: The Method and Results of Identifying Phase Dominant Inverse Kinematics

Optimization Criteria Based on Motion Capture Data

In the preceding section, the focus was on investigating whether human motion results from optimizing a single criterion or a combination of multiple criteria and exploring the diverse performance criteria that influence the choice of particular arm configurations by humans during various ADLs. In this section, we examine how different performance criteria influence arm movements across various phases of ADLs.

To systematically address this objective, eight participants were recruited to participate in the execution of four predetermined ADLs as explained in section 3.5. This approach facilitated the evaluation of median values linked to each performance criterion throughout the entire task duration, thereby offering valuable insights into the primary performance criteria shaping the trajectory of each task.

The dataset containing values corresponding to each performance criterion was collected and subsequently subjected to analysis employing SPM. The core aim of this analytical process was to identify the specific performance criterion or combination thereof that most accurately captured the typical behavior exhibited during the different stages of ADL task execution.

Through examination of the acquired results, this investigation yielded invaluable insights into the influences exerted by distinct performance criteria within the context of ADLs.

5.1 Brushing Task

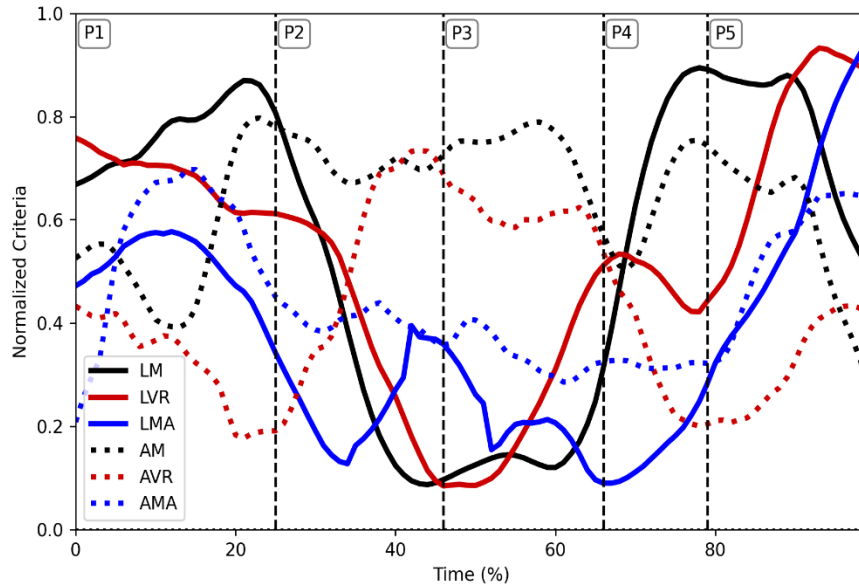


Figure 5.1 The mean continua of the criteria for brushing task.

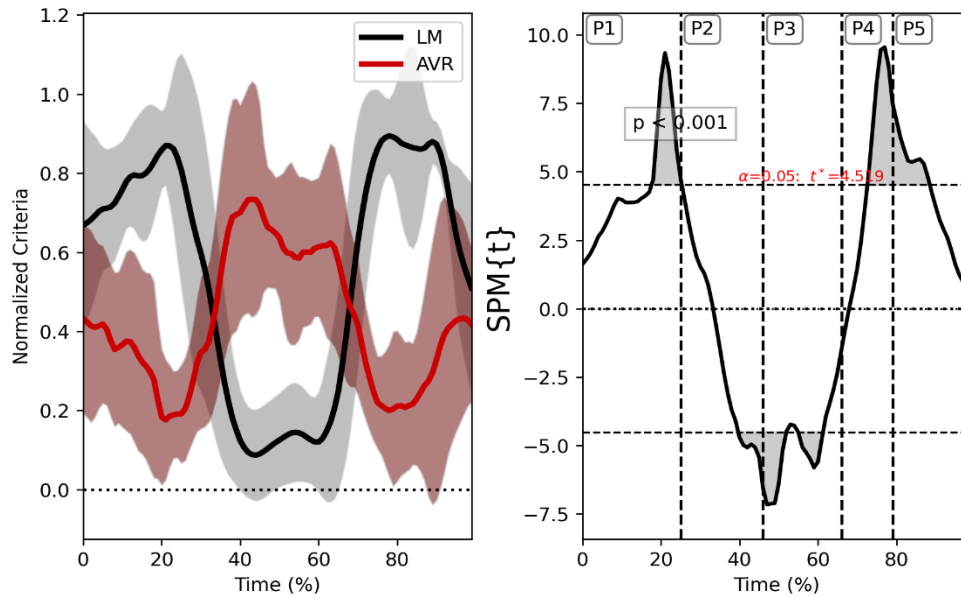


Figure 5.2 Left: The LM and AVR mean continua with their standard deviations. Right: The SPM t-test value and the regions of significance (shaded)

The brushing task is comprised of five distinct phases, denoted as P1 to P5, as visually represented in Figure 3.14. These phases encompass a sequence of actions, including the initiation of movement from the resting posture to the acquisition of the hairbrush (P1), the guidance of the hairbrush towards the head (P2), the combing through a section of hair (P3), the return of the brush to the table (P4), and the restoration of the initial posture (P5). For a visual representation of the evolving trends in normalized criteria throughout each phase of the brushing task, continuous mean trajectories are provided in Figure 5.1.

Upon a thorough analysis of the results, it becomes apparent that two specific criteria, LM and AVR, assume critical roles across various phases of the task. In Figure 5.2, the mean trajectories of LM and AVR, accompanied by their respective standard deviations, are presented. The left-hand graphs visually depict these metrics along with their standard deviations, while the right-hand graph illustrates the t-test values throughout the task duration. Notably, these trajectories intersect at two critical phases: the initiation of P2 and before the ending of the P4.

During the phase associated with acquiring the hairbrush (P2), LM significantly increases values as the hand descends, indicating a substantial enhancement in agility at this specific juncture. Conversely, the AVR metric exhibits an elevation in values as the hand ascends to perform the brushing task, signifying an augmented AVR while maintaining proximity to the top of the head. The shaded regions representing standard deviation consistently remain compact throughout the hand movement's ascending and descending phases. This observation implies that the kinematic strategy employed for the linear component of the task exhibits a relative consistency among individuals. In the context of the P3 phase, noticeable variations in standard deviation become evident, indicating a broader spectrum of user performance in the brushing task. This diversity is characterized by using various arm configurations tailored to meet the specific task

requirements. This analysis underscores the critical role played by LM and AVR in task execution. These criteria emerge as important determinants, suggesting their potential application within the WLN method as gradient-based weights to maximize the respective criterion during each task phase. This utilization of LM and AVR as dynamic weighting factors can effectively adapt to the varying demands imposed by different phases, thereby optimizing overall brushing task performance.

5.2 Drinking from a Cup Task

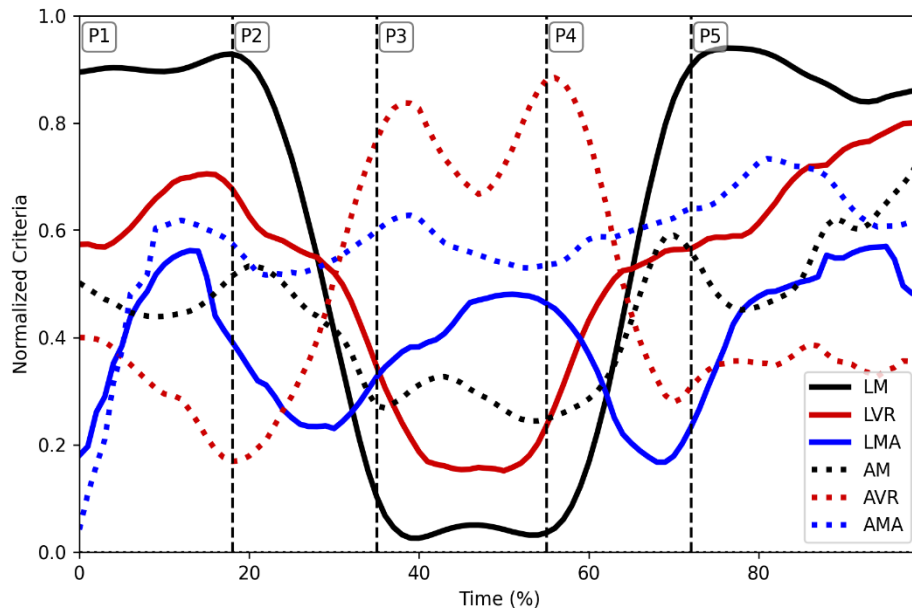


Figure 5.3 The mean continua of the criteria for drinking from a cup task.

The drinking from a glass task is composed of five distinct phases, labeled as P1 to P5 as shown in Figure 3.15, involving a sequence of actions that encompass glass grasping (P1), bringing it to the mouth (P2), drinking from it (P3), returning it to the table (P4), and finally, returning to the initial posture (P5). Figure 5.3 visually represents the continuous mean trajectories of normalized criteria throughout each phase.

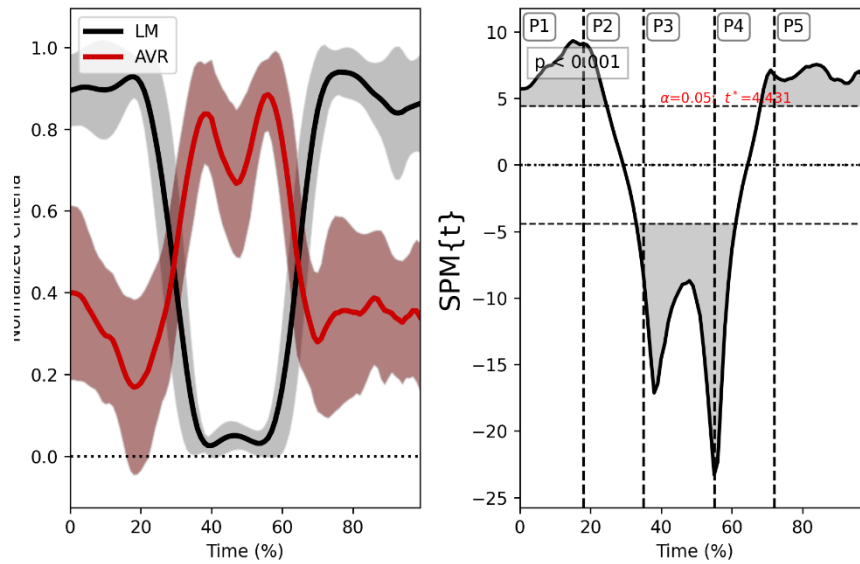


Figure 5.4 Left: The LM and AVR mean continua with their standard deviations. Right: The SPM t-test value and the regions of significance (shaded)

Upon conducting a comprehensive analysis of the results, it becomes evident that two specific criteria, LM and AVR, assume critical roles at various stages of the task similar to brushing task. Figure 5.4 provides a detailed examination of these pivotal metrics, LM and AVR, along with their respective standard deviations (left-hand side) and t-test values over time (right-hand side). Remarkably, these trajectories intersect at two significant phases: the commencement of the second phase (P2) and the end of the third phase (P3). An exhaustive data analysis reveals several noteworthy findings. Firstly, a distinct pattern emerges wherein LM experiences a notable increase in values at the onset of P2, coinciding with the hand's descent during the glass-grasping phase. This observation suggests a substantial enhancement in dexterity, particularly during this specific phase. Conversely, the AVR metric increases as the hand ascends for the drinking task in both P2 and P3, indicating an elevated AVR while maintaining proximity to the mouth. Throughout the ascending and descending phases of hand movement, the standard deviation remains compact,

implying a consistent and uniform kinematic approach employed by individuals for the linear aspect of the task. In the context of the P3 phase of the drinking from a cup Task, noticeable variations in standard deviation become apparent, signifying a wider spectrum of user performance characterized by the utilization of diverse arm configurations tailored to the specific demands of the task.

This analysis highlights the pivotal roles LM and AVR play in executing the task. These criteria emerge as critical determinants, indicating their potential applicability within the WLN method as gradient-based weighting factors to maximize the respective criterion during each task phase. This strategic utilization of LM and AVR as dynamic weighting factors demonstrates an ability to adapt effectively to the dynamic demands imposed by different task phases, consequently optimizing overall performance in the drinking from a cup task.

5.3 Opening a Higher-Level Cabinet Task

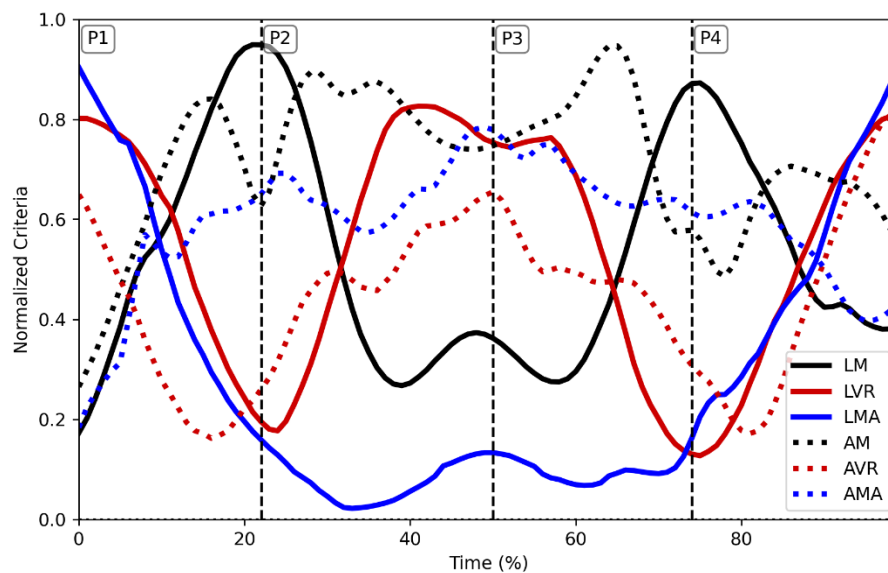


Figure 5.5 The mean continua of the criteria for opening a higher-level cabinet task

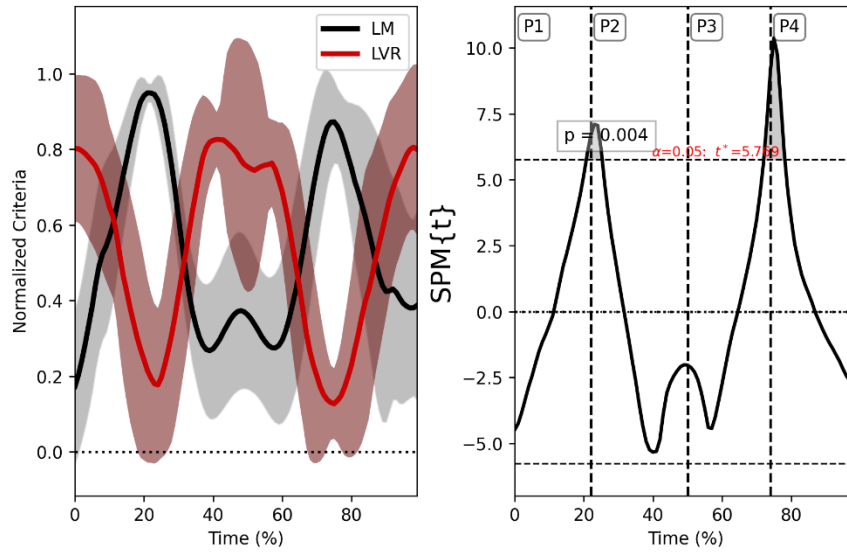


Figure 5.6 Left: The LM and LVR mean continua with their standard deviations. Right: The SPM t-test value and the regions of significance (shaded)

Opening a higher-level cabinet involves a sequence of precisely coordinated movements, which can be divided into four distinct phases (P1-P4) as shown in Figure 3.16. These phases encompass a series of sequential actions, commencing with the initiation of the reach to grasp the door handle or knob from a resting pose (P1), followed by the action of pulling the door open (P2), subsequently pushing the door closed (P3), and culminating in a return to a neutral posture (P4). As depicted in Figure 5.5, continuous mean trajectories of normalized criteria provide a visual representation of how these criteria evolve during each phase of the task. Notably, this visualization highlights the significant influence of two specific criteria LM and LVR, on task performance. A deeper understanding of the relationship between LM and LVR is presented in Figure 5.6, where the left-hand graphs visually depict these metrics alongside their respective standard deviations. In contrast, the right-hand graph dynamically illustrates t-test values over time, serving as a robust indicator of the statistical significance between LM and LVR as the task unfolds.

Throughout the execution of the task involving opening a higher-level cabinet, distinct patterns emerge in the influence of LM and LVR. During the initial phase (P1), there is a conspicuous increase in LM values, signifying an enhancement in hand agility, particularly in the context of door opening. Subsequently, in phase P2, LVR experiences a rise, coinciding with a decrease in LM, indicating a shift in arm strategy to enhance agility in the direction of motion. These two criteria continue to alternate in their influence throughout the task, reflecting a dynamic adaptation of arm motion strategies to meet the evolving demands of each task phase. Notably, the standard deviation remains consistently compact during the execution of phases P2 and P3 of hand movement, suggesting that the kinematic strategy for the linear component of the task remains relatively consistent among individuals during these phases.

In the specific context of the P3 phase of opening a higher-level cabinet, a noticeable divergence in standard deviation becomes apparent, indicating a broader spectrum of user performance characterized by the utilization of diverse arm configurations tailored to meet the specific demands of the task. This analysis underscores the pivotal roles played by LM and LVR in the execution of the task, as these criteria emerge as critical determinants of performance. The findings suggest the potential applicability of LM and LVR within the WLN method, where they can serve as gradient-based weighting factors aimed at maximizing the respective criterion during each phase of the task. This strategic utilization of LM and LVR as dynamic weighting factors underscores their inherent adaptability to the dynamic demands imposed by different task phases, ultimately optimizing overall performance in the context of the task involving the opening of a higher-level cabinet.

5.4 Picking Up a Full Water Jug for Shelving Task

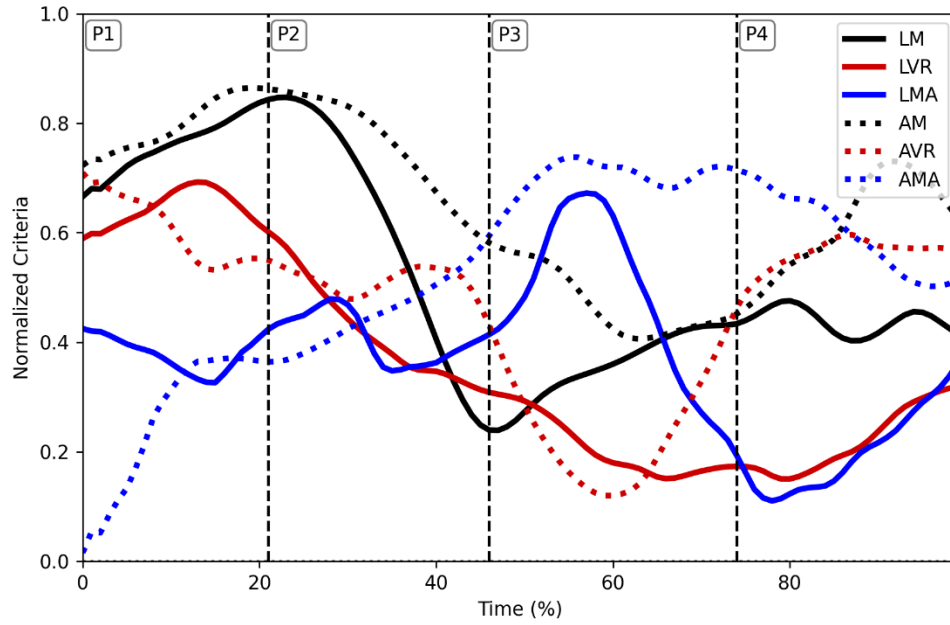


Figure 5.7 The mean continua of the criteria for picking up a full water jug for shelving task

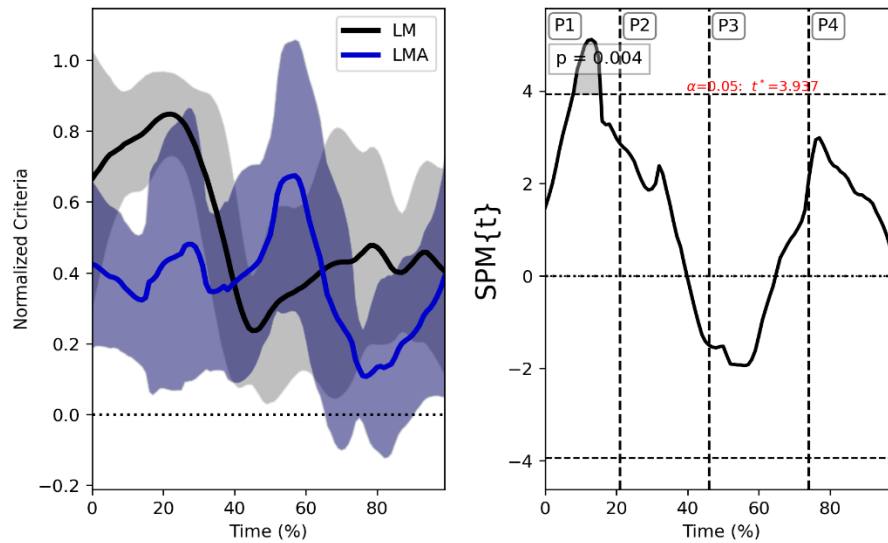


Figure 5.8 Left: The LM and LMA mean continua with their standard deviations. Right: The SPM t-test value and the regions of significance (shaded)

Picking Up a Full Water Jug for Shelving can be divided into four distinct phases, denoted as P1 to P4 as shown in Figure 3.17. These phases encompass a series of sequential actions, commencing with object acquisition (P1), followed by the motion of bringing the object closer to the body to facilitate lifting (P2), the actual lifting of the object and its placement on the shelf (P3), and concluding with a return to the initial posture (P4). A graphical representation of this multifaceted task is presented in Figure 5.7, illustrating continuous mean trajectories of normalized criteria throughout its execution.

Upon examination of the results, it becomes evident that two specific criteria wield substantial influence over task performance. These pivotal metrics, LM and LMA, are depicted in Figure 5.8. The left-hand graphs within Figure 5.8 provide visual representations of these metrics alongside their associated standard deviations, while the right-hand graph dynamically illustrates t-test values over time, offering insights into the statistical significance between LM and LMA as the task unfolds. At the onset of the task, particularly in the initial phase (P1), LM exhibits elevated values, signifying an enhanced level of hand agility and adaptability during object acquisition. However, as the task progresses into subsequent phases, starting with P2, LM values gradually diminish. In contrast, LMA demonstrates an ascending trajectory from P2, reaching its peak in P3.

The inherent nature of picking up a full water jug for a shelving task involves manually handling a substantial object, taking a significant degree of elevation. This additional weight imposes constraints on the hand's flexibility, compelling the coordination of multiple joints to maintain the object's orientation and facilitate efficient lifting. Consequently, this coordination increases mechanical advantage in the linear direction of motion during P3 phase. An important observation pertains to the consistent compactness of the standard deviation of LM during the execution of phases P1 and P2 of hand movement. This observation suggests that the kinematic

strategy employed for the linear component of the task maintains a relative consistency among individuals during these initial phases.

As the task progresses into the initial segment of the P3 phase of picking up a full water jug for the shelving task, a noticeable divergence in standard deviation becomes apparent in LMA. This divergence signifies a broader spectrum of user performance characterized by the utilization of diverse arm configurations tailored to meet the specific demands of the task. This analysis underscores the pivotal roles played by LM and LMA in the execution of the task, as these criteria emerge as critical determinants of performance. The findings suggest the potential applicability of LM and LMA within the WLN method, where they can function as gradient-based weighting factors to maximize the respective criterion during each task phase. This strategic utilization of LM and LMA as dynamic weighting factors underscores their inherent adaptability to the dynamic demands imposed by different task phases, ultimately optimizing overall performance in picking up a full water jug for a shelving task.

5.5 Summary

The primary objective of this section was to reveal the dominant performance criteria underlying human arm movements across a spectrum of ADLs. To accomplish this objective, an experimental study was conducted, involving a group of eight participants tasked with the execution of four specific ADL: Brushing, Drinking From A Cup, Opening A Higher-Level Cabinet, and Picking Up A Full Water Jug For A Shelving Task. Motion capture technology facilitated the acquisition of precise data, enabling the evaluation of median values associated with each performance criterion during the execution of these tasks. To gain further insight into these criteria across diverse phases of the tasks, SPM analysis was employed to elucidate their relative significance.

This study comprehensively explores the dominant performance criteria humans use to plan arm movements. The SPM analyses conducted on the values of these performance criteria unveil their varying degrees of importance throughout distinct task phases. The results affirm the hypothesis that humans adeptly optimize performance criteria at discrete task phases, underscoring their innate capacity to combine different criteria to facilitate effective motor control.

Subsequently, the forthcoming chapter will employ the observed results from Chapter 4 and Chapter 5, integrating them into the WLN algorithm in conjunction with joint limit avoidance. This combination aims to replicate human-like motion within the context of the RHUBM. The algorithm's effectiveness will be measured through a comparative analysis of RMS error between the WLN algorithm's output, and the ground truth provided by the motion capture data. This assessment will serve as a yardstick for quantifying the algorithm's capacity to emulate human-like movements during ADLs.

Chapter 6: Inverse Kinematics Methods and Results Predicting Human-Like Motion

6.1 Inverse Kinematics Methods for Predicting Human Motion

As discussed in Section 2, in robotics, achieving precise positioning and orientation of the end-effector within its workspace is crucial for effective task execution. To achieve this level of accuracy, six DOFs are required. Interestingly, with its numerous joints, the human body displays a redundant kinematic chain, expertly controlled by the central nervous system, enabling the execution of complex tasks in unstructured environments. Biomimetic robots aspire to replicate certain aspects of human motion, emphasizing achieving a kinematic and dynamic correspondence with the desired end-effector, typically the hand. This endeavor adopts a task-driven approach, with the challenge of identifying specific elements of human motion that should be replicated, all while ensuring that translational and rotational velocities align with the intended end-effector behavior.

Addressing this complex challenge, various inverse kinematics methodologies have emerged, as discussed in Section 2.2. The goal of replicating human motion drives each of these methodologies. This section's primary objective is to thoroughly investigate the two prominent methods utilized in this research: Least Norm and Weighted Least Norm. Furthermore, this examination will include a detailed account of the error analysis techniques employed to assess the accuracy of each method.

6.1.1 Least Norm Solution

Numerous algorithms have been developed to address the redundancy present in robotic arms, with one of the most direct approaches at the velocity level being the Least Norm solution,

often computed using the Jacobian matrix. The Least Norm method employs the pseudo-inverse for a redundant arm (i.e., the Jacobian matrix is non-singular). In cases of a non-redundant arm (i.e., the Jacobian matrix is singular), the inverse of the Jacobian matrix is employed. These methods establish a correspondence between the end effector's cartesian velocity and joint angle velocity, thereby enabling the derivation of an inverse kinematics solution by computing the disparity between the forward kinematic solution and the desired end effector position. In this study, the Least Norm solution served as a fundamental reference point for assessing the performance of various control algorithms and conducting qualitative evaluations of motion quality.

In forward kinematic Equation 6.1, a six-by-one vector represents the Cartesian position and orientation of the right hand alongside a corresponding one-by-ten joint angle vector. The Jacobian matrix establishes the relationship between the joint angle velocity and the end-effector's velocity and rotation in Cartesian space. The Least Norm solution for inverse kinematics is expressed in Equation 6.3, utilizing the pseudo-inverse of the Jacobian matrix, as described in Equation 6.2.

$$\dot{x} = J\dot{\theta} \quad 6.1$$

$$J^+ = J^T(JJ^T)^{-1} \quad 6.2$$

$$\dot{\theta}_{LN} = J^+\dot{x} \quad 6.3$$

Due to the equations' inherent non-linearity, an error was introduced in proportion to the step size between successive end-effector trajectory points. To mitigate this error, we have implemented an iterative method designed to maintain errors below specific thresholds. These thresholds have been established at less than 1mm for linear error and 1 degree for angular error.

The iterative least norm solution, a cornerstone of this methodology, is formally defined in Equation 6.4. In this equation, the variable θ_i represents the current joint angle vector at iteration i , while x_{i+1} symbolizes the desired end-effector position and orientation. x_c characterizes the current end-effector position and orientation as determined by the forward kinematics $fkine(\theta_i)$ of the RHUBM, and θ_{i+1} represents the joint angle vector associated with the target end-effector position.

$$\theta_{i+1} = \theta_i + J^+(x_{i+1} - x_c) \quad 6.4$$

This iterative process ensures that the robotic manipulator adeptly attains the desired position and orientation while adhering to the specified error thresholds. Consequently, it enhances the precision and reliability of task execution.

In this study, we have employed two distinct approaches: LN and WLN. WLN is based on an algorithm that assigns different weights to velocities, while LN is an unbiased method. However, our research findings have highlighted a crucial distinction between these two approaches.

The results indicate that the LN solution inherently exhibits bias by favoring the motion of proximal joints, such as the torso joints, over distal ones, like the wrist joints. This inherent bias leads to motions that deviate from human-like patterns. Notably, previous studies have also reported increased torso movement when LN is applied to able-bodied individuals [4]. This emphasizes the importance of considering these biases when implementing inverse kinematics algorithms, particularly in tasks that achieve human-like motions. Further analysis and evaluation of these biases will be discussed in later sections.

6.1.2 Weighted Least Norm Solution

As discussed in the previous section LN, although it is considered non-biased, inherently exhibits biased behavior by favoring the proximal joints more than the distal joints. To deal with this problem, we must move joints with a particular priority that will fulfill our objective. This can be done by using the Weighted Least Norm method.

According to the findings presented by Chan and Dubey, the management of relative joint motion can be achieved through the incorporation of a weighting term into the joint angle velocity norm as shown in 6.5.

$$\|\dot{\theta}\|_{WLN} = \sqrt{\dot{\theta}^T W \dot{\theta}} \quad 6.5$$

In this context, 'W' represents a symmetric positive definite weighting matrix, with dimensions 'n' by 'b,' where 'n' corresponds to the number of joints within the manipulator's structure. To introduce relative motion among various joints, the concepts of the weighted Jacobian and weighted joint angle velocity are utilized.

$$J_w = J W^{\frac{1}{2}} \text{ and } \dot{\theta}_w = W^{\frac{1}{2}} \dot{\theta} \quad 6.6$$

$$\dot{x} = J_w \dot{\theta}_w = J W^{\frac{1}{2}} W^{\frac{1}{2}} \dot{\theta} = J \dot{\theta} \quad 6.7$$

$$\dot{\theta}_w = J_w^+ \dot{x} \quad 6.8$$

$$\dot{\theta}_{WLN} = W^{-1} J^T [J W^{-1} J^T]^{-1} \dot{x} \quad 6.9$$

The weighted Jacobian matrix, denoted as J_w in Equation 6.6 is defined as the product of the weighting matrix 'W' and the original Jacobian 'J.' Similarly, the weighted joint angle velocity vector, represented as $\dot{\theta}_w$ in Equation 6.6 results from the multiplication of W and the standard joint angle velocity vector $\dot{\theta}$. The WLN solution can be derived by eliminating the weighting

factors from the angular velocity vector, thereby obtaining an expression that can be expanded through the pseudo-inverse as shown in Equations 6.8 and 6.9. This transformation results in the Weighted Least Norm formulation as a function of the inverse weights, allowing for the precise control and coordination of joint movements while addressing the bias inherent in traditional Least Norm methods. This methodology proves instrumental in achieving more human-like motions. Similar to the LN method, the WLN method can also be employed iteratively as shown in Equation 6.10.

$$\theta_{i+1} = \theta_i + (W^{-1} J^T [J W^{-1} J^T])(x_{i+1} - x_c) \quad 6.10$$

6.1.2.1 Link Based Weights

To mitigate the inherent bias of the LN method and achieve joint angle trajectories that closely resemble human-like motions, assigning priorities to individual joints that align with our objectives is imperative. In this research, we draw valuable insights from the extensive literature review presented in section 2. This review underscores a fundamental characteristic of human motion: the concerted effort to minimize joint load through strategic adjustments in joint configurations.

The RHUBM comprises 10 DOF and features four distinct links: Torso, Upper arm, Lower arm, and Hand. This kinematic structure spans from the Torso, the base (proximal) joint, to the Wrist, which functions as the end effector (distal) joint. Building upon the insights gleaned from the comprehensive analysis in Table 3.5, we can precisely calculate the weight associated with each link segment, as supported by the literature [106] and presented in Table 3.4. These computed weights serve as static parameters and are subsequently applied to their corresponding joints within the robotic system. The outcome of this weight assignment process results in the formulation of a weight matrix, as shown in 6.11, which is derived based on the individual link weights.

$$W_{\text{Link Weight}} = \begin{bmatrix} W_1 & 0 & 0 & 0 & 0 & 0 & 0 & 0 & 0 & 0 \\ 0 & W_1 & 0 & 0 & 0 & 0 & 0 & 0 & 0 & 0 \\ 0 & 0 & W_1 & 0 & 0 & 0 & 0 & 0 & 0 & 0 \\ 0 & 0 & 0 & W_2 & 0 & 0 & 0 & 0 & 0 & 0 \\ 0 & 0 & 0 & 0 & W_2 & 0 & 0 & 0 & 0 & 0 \\ 0 & 0 & 0 & 0 & 0 & W_2 & 0 & 0 & 0 & 0 \\ 0 & 0 & 0 & 0 & 0 & 0 & W_3 & 0 & 0 & 0 \\ 0 & 0 & 0 & 0 & 0 & 0 & 0 & W_3 & 0 & 0 \\ 0 & 0 & 0 & 0 & 0 & 0 & 0 & 0 & W_4 & 0 \\ 0 & 0 & 0 & 0 & 0 & 0 & 0 & 0 & 0 & W_4 \end{bmatrix} \quad 6.11$$

Notably, the Torso is the heaviest among the various segments within the RHUBM's kinematic structure. Consequently, by strategically assigning higher weights to the Torso joints, we effectively curtail the extent of Torso movement compared to the other joints. This deliberate weight allocation strategy is aligned with the overarching objective of minimizing joint load, thereby affording more substantial and pronounced movements within the lighter joints instead of the heavier ones. In essence, this weight distribution strategy closely emulates human-like behavior, fostering a more effective replication of human motions within the robotic system.

6.1.2.2 Joint Limits Avoidance Weights

The WLN method provides the flexibility to adjust joint movements relative to each other based on specific objective function. Among the various important objectives, a crucial one is to prevent the robotic joints from reaching their limits. In the human kinematic chain, inherent limitations exist in the ROM for different joints. The largest ROM is observed in shoulder horizontal flexion/extension, while the smallest is in Wrist Abduction/Adduction, as visually depicted in Figures 3-5 to 3-12 and outlined in Table 3.8. However, these limitations do not hinder the human hand from executing complex tasks with remarkable dexterity. The human arm, with a high number of DOF, functions as a redundant manipulator, capable of utilizing various joint

combinations to accomplish intricate tasks. Researchers have delved into mathematical representations of joint limits in robotic manipulators, including the approach proposed by [62].

$$H_{JL}(\theta) = \sum_{i=1}^n \frac{1}{4} \frac{(\theta_{i\max} - \theta_{i\min})^2}{(\theta_{i\max} - \theta_i)^2 (\theta_i - \theta_{i\min})} \quad 6.12$$

Equations 6.12, 6.13, and 6.14 i represent a joint number, $\theta_{i\max}$ maximum joint limit of joint i from MoCap data and $\theta_{i\min}$ minimum joint limit of joint i from MoCap data.

This representation is rooted in the proximity of the current joint angles to either the highest or lowest limit, as detailed in Equation 6.12. The incorporation of this optimization function into Equation 6.9 can be realized by employing a weight matrix for optimization, as shown in Equation 6.13.

$$W_{\text{Joint Limit Weight}} = \begin{bmatrix} \left| \frac{\partial H_{JL}(\theta)}{\partial \theta_1} \right| & 0 & \dots & 0 \\ 0 & \left| \frac{\partial H_{JL}(\theta)}{\partial \theta_2} \right| & \dots & 0 \\ \vdots & \vdots & \ddots & \vdots \\ 0 & 0 & \dots & \left| \frac{\partial H_{JL}(\theta)}{\partial \theta_{10}} \right| \end{bmatrix} \quad 6.13$$

The derivative is given by Equation 6.14.

$$\frac{\partial H_{JL}(\theta)}{\partial \theta_i} = \frac{(\theta_{i\max} - \theta_{i\min})^2 (2\theta_i - \theta_{i\max} - \theta_{i\min})}{4(\theta_{i\max} - \theta_i)^2 (\theta_i - \theta_{i\min})^2} \quad 6.14$$

From the above equation, it can be concluded that when a specific joint resides within the middle of its joint range, Equation 6.14 yields a weight value of zero for that joint. Conversely, when a particular joint reaches its limit, Equation 6.13 results in an "infinity" weight, effectively rendering the joint immobile beyond its limit. The criterion function governing these weights is

subject to four distinct conditions, as detailed in Figure 6.1. It is worth noting that the applicability of the third and fourth conditions primarily arises when employing coarse step sizes in the optimization process[108]. However, in our research, we have utilized very fine step sizes, rendering conditions 3 and 4 unnecessary for any of the tasks.

These conditions can be summarized as follows:

- (C1) When a joint approaches its limit from the outside and continues moving towards the limit (i.e., the weight difference between two consecutive steps is positive, and the current joint limit is not exceeded), the weight is calculated using Equation 6.15. Where i is a joint number and k is a tuning parameter. This means that it will slow down that particular joint relative to other joints.

$$w_i = k \left| \frac{\partial H_{JL}(\theta)}{\partial \theta_i} \right| \text{ if } \Delta \left| \frac{\partial H_{JL}(\theta)}{\partial \theta_i} \right| \geq 0 \quad \& \quad \theta_{i\min} \leq \theta_i \leq \theta_{i\max} \quad 6.15$$

- (C2) When a joint approaches its limit from the outside and then moves away from the limit (i.e., the weight difference between two consecutive steps is negative, and the current joint limit is not exceeded), the weight assigned is 1. This allows that particular joint to move without any restriction.

$$w_i = 0 \quad \text{if } \Delta \left| \frac{\partial H_{JL}(\theta)}{\partial \theta_i} \right| < 0 \quad \& \quad \theta_{i\min} \leq \theta_i \leq \theta_{i\max} \quad 6.16$$

- (C3) If a joint approaches its limit from inside the limit and proceeds to move away from it (i.e., the weight difference between two consecutive steps is negative, and the current joint limit is exceeded), an infinite weight is assigned, effectively prohibiting further motion inside the limit.

$$w_i = \infty \quad \text{if } \Delta \left| \frac{\partial H_{JL}(\theta)}{\partial \theta_i} \right| < 0 \ \& \ \theta_{i\min} \geq \theta_i \geq \theta_{i\max} \quad 6.17$$

- (C4) Similarly, when a joint approaches its limit from inside the limit and moves towards the limit (i.e., the weight difference between two consecutive steps is positive, and the current joint limit is exceeded), the weight assigned is 1, indicating that the joint is moving away from its limit.

$$w_i = 0 \quad \text{if } \Delta \left| \frac{\partial H_{JL}(\theta)}{\partial \theta_i} \right| \geq 0 \ \& \ \theta_{i\min} \geq \theta_i \geq \theta_{i\max} \quad 6.18$$

6.1.2.3 Gradient Based Weights

In recent years, researchers have focused on analyzing the intricacies of day-to-day human activities to understand the various performance criteria humans instinctively optimize while carrying out tasks. It has become evident through human demonstrations that individuals make the most of redundancy when performing ADLs. These underlying criteria are intrinsic to human motion, and the subconscious optimization of these diverse factors governs our movements. In this section, we propose a fundamental approach to harnessing and maximizing these inherent strategies of human motion by incorporating numerical gradient values as weighting factors within the weighted least norm algorithm.

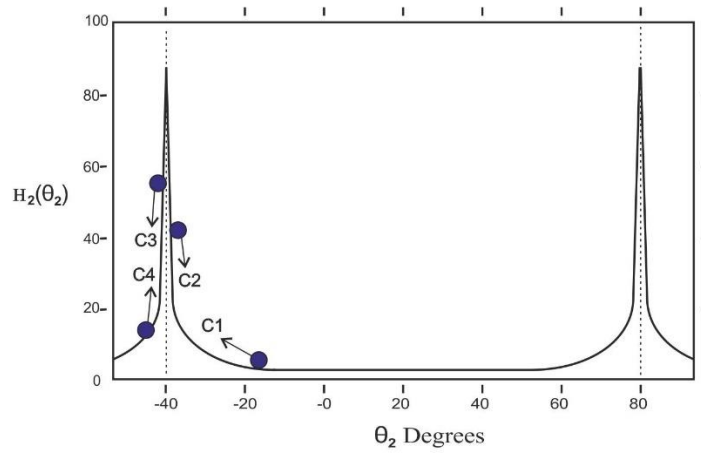


Figure 6.1 Gradient of joint limit

A gradient is a vector that signifies the rate of change of a function at a specific point. It points in the direction of the steepest ascent of the function, and its magnitude quantifies the rate of change in that direction. This research aims to maximize specific performance criteria that constitute intrinsic human movement strategies, including Manipulability, Velocity Ratio, and Mechanical Advantage. Details of each criterion are given in Section 2.3. Since obtaining analytical gradients for these performance criteria is challenging, we have opted to consider numerical gradients for each of them. The numerical gradient method is a computational technique for estimating the gradient of a function when obtaining an analytical gradient expression is either impractical or unavailable. This method approximates the gradient by evaluating the function at a finite step in both directions from a given point. Then, it employs finite differences to estimate the rate of change.

Within the framework of the WLN solution, we can utilize these numerical gradient values as weights to enhance the manipulator's overall performance. Given our objective of maximizing performance criteria, we assign '1' weight to joints whose gradients are improving so that those

particular joints move without any restriction and contribute more to improving the overall performance of the manipulator, while joints with decreasing or negative gradients receive weights as calculated by Equation 6.19, resulting in relatively restricted motion. The representation of this algorithm is provided below where h represents a small positive value that determines the step size.

$$\nabla H_{PC}(\theta_i) = \frac{f(\theta_i + h) - f(\theta_i - h)}{2h} \quad 6.19$$

$$W_{\text{Gradient Weight } i} = \begin{cases} |\nabla H_{PC}(\theta_i)| & \text{if } \nabla H_{PC}(\theta_i) \leq 0 \\ 0 & \text{if } \nabla H_{PC}(\theta_i) > 0 \end{cases}$$

It is worth noting that the accuracy of the numerical gradient hinges on the choice of finite differences and the step size employed, underscoring the importance of parameter tuning for dependable results.

6.1.2.4 Combined Weights

The WLN method offers the distinct advantage of combining multiple weight factors into a singular weight matrix. This methodology confers the flexibility required for effectively controlling a manipulator, all while optimizing specific performance criteria. Within this section, we explore the integration of various control schemes, merging their capabilities to attain human-like motion and simultaneously maximize desired performance criteria. To achieve this objective, we consider a range of weights, including link weight, weight due to joint limit, and weights based on dominant performance criteria represented as gradient weight in Equation 6.20. Each weight carries its own unique significance during various phases of the task. Through the merger of these weights and the introduction of fine-tuning parameters, the capacity to prioritize performance criteria over others is realized, as illustrated in Equation 6.20,

$$\text{Total Weight} = W_{\text{Link Weight}} + A \cdot W_{\text{Joint Limit Weight}} + B \cdot W_{\text{Gradient Weight}} \quad 6.20$$

where A and B serve as fine-tuning parameters.

Among these weights, those derived from link weights are categorized as static weights and hold a dominant role. On the other hand, the joint limit weights and gradient weights are dynamic in nature, contributing dynamically to the maximization of specific performance criteria during distinct phases of the task. In the upcoming results section, we will analyze the outcomes obtained by combining the different weights using Equation 6.20. We will refer to this combined weight matrix method as WLN_{CWM} .

6.1.3 Error Analysis

In order to assess the effectiveness of our approach, it is imperative to conduct a comparative analysis between the joint angles obtained from our simulation and those derived from MoCap data. This evaluation is facilitated through the utilization of a well-established metric, namely the RMS error, as represented mathematically in Equation 6.21. The RMS error provides a quantitative measure of the disparity between the two sets of joint angles, thereby serving as a robust indicator of the method's efficiency and its ability to accurately replicate human-like movements. where θ_{Mocap_i} for joint i , and $\theta_{Simulation_i}$ for our calculated joint angle values, covering the entire trial duration marked by ' n ' data points.

$$RMS_{\text{ERROR}} = \sqrt{\frac{\sum_{i=1}^n (\theta_{Mocap_i} - \theta_{Simulation_i})^2}{n}} \quad 6.21$$

6.2 Results of Different Motion Control Algorithm

The following section is an in-depth exploration of diverse inverse kinematics algorithms, engaging in an assessment of their performance metrics when compared with data acquired from motion capture technology. The central objective of this examination resides in selecting the algorithm that shows the best reliability in replicating human-like motion. This analysis includes examinations of the LN method alongside the WLN method; this technique allows for the selection of weights based on various components, effectively controlling joint motion through these assigned weights and enabling relative motion between joints. The WLN method involves a complex weighting scheme that involves factors such as link weight, joint limits, and a gradient-based weight, as explained in section 6.1.2.4, WLN_{CWM} accompanied by fine-tuning parameters labeled as A and B. For this research work, the values of A and B are set to one. This decision recognizes that the selection of fine-tuning parameters is highly subject-specific, and altering these values can affect the algorithm's efficiency. Maintaining uniform values for A and B avoids the complexities associated with comparing performance across various subjects and algorithms, thus ensuring a more balanced and fair evaluation framework. In Section 6.1.2.1, the analyses clarify that link weights play a crucial role in reducing movements in the heavier joints, which, in turn, lessens the total torque on these joints. The calculation of weights, which are based on joint limits, is detailed in Section 6.1.2.2. Moving on to the third component of the weight matrix, the gradient of performance criteria is involved. The methodology for computing the numerical value of the gradient with respect to each performance criterion is detailed in Section 6.1.2.3.

Understanding the numerical implications of weight values is essential for discerning the range of mobility associated with each joint. Weight values approaching zero denote a highly mobile joint, reflecting its frequent movement. However, in this specific method, weights do not

attain a zero-value due to the incorporation of link weights as the static weight, which inherently cannot be zero. On the other hand, weight values trending towards infinity indicate a joint with limited mobility, suggesting a tendency towards minimal movement. The examination of these weight values provides critical insights into the operational patterns of the joints across different tasks, pinpointing which joints are primarily active or remain largely stationary.

The overarching aim of this chapter extends beyond the simple identification of the most proficient algorithm for simulating the intricacies of human inverse kinematics. It embarks on a deeper investigation to unveil the fundamental reasonings underlying the prominence of specific weighting components in the execution of ADL. In doing so, it offers invaluable insights into the practical significance of these weight factors and their potential to stimulate human-like motion in future research work.

6.2.1 Brushing Task

Section 3.7.2 describes the "Brushing" task as encompassing five distinct phases, labeled P1 through P5, with a visual depiction provided in Figure 3.14. The simulation of human-like motion during this task in the RHUBM model employs the WLN method.

Figure 5.1 demonstrates how the normalized criteria evolve during each phase of the brushing task, helping identify which performance criteria most significantly affect the algorithm's overall effectiveness. Furthermore, Figure 5.2 provides insights into the shifts in selected performance criteria across different task phases. Notably, in the brushing task, Figure 5.2 shows where the LM and AVR trajectories intersect between the start of phase P2 and the end of phase P4. This intersection indicates the specific phases in which to maximize performance criteria, based on the gradient of these criteria and their integration into the weight matrix, a process outlined in Section 6.1.2.4.

During the hair-brushing task, priority is given to LM in phases P1, P4, and P5, whereas AVR is emphasized in phases P2 and P3. For each of the eight subjects studied, the phases were marked, and this information was used to calculate the gradient values of the respective performance criteria for each phase. Table 6.1 presents the average total weights for these eight subjects under WLN_{CWM} .

Table 6.1 Average weights of eight subjects using combined weights method

Anatomical Joint	WLN_{CWM}
Torso Lateral Flexion	43.3650
Torso Flexion/Extension	43.3807
Torso Rotation	43.3696
Shoulder Horizontal Flexion/Extension	4.1575
Shoulder Abduction/Adduction	4.1880
Shoulder Rotation	6.3829
Elbow Flexion	1.8306
Elbow Pronation/Supination	4.0816
Wrist Flexion/Extension	0.5406
Wrist Abduction/Adduction	40.9765

The Table 6.1, focuses on WLN_{CWM} , reveals that the torso joints have the highest weights relative to other joints. This suggests reduced movement compared to the shoulder and elbow joints. Notably, the dominant weights of the torso joints are predominantly linked weights. Joint

limit and gradient weights do not contribute maximally to the overall performance, which is explained in the latter part of the section.

Table 6.2 Brushing task average RMS error evaluation

Anatomical Joint	LN (deg)	St.D.	WLN_{CWM} (deg)	St.D.
Torso Lateral Flexion	8.2506	0.0943	3.7242	0.0162
Torso Flexion/Extension	20.7754	0.1285	3.2659	0.0327
Torso Rotation	18.2888	0.1595	3.9706	0.0456
Shoulder Horizontal Flexion/Extension	17.2747	0.1470	3.2682	0.0842
Shoulder Abduction/Adduction	14.3010	0.1169	5.3400	0.0398
Shoulder Rotation	32.6013	0.2643	11.7915	0.2150
Elbow Flexion	22.8037	0.3201	8.4683	0.0541
Elbow Pronation/Supination	14.4328	0.1037	14.3755	0.0929
Wrist Flexion/Extension	15.5787	0.1656	6.9557	0.1194
Wrist Abduction/Adduction	33.1112	0.3198	10.8576	0.0061

Conversely, the wrist flexion/extension joint displays the lowest weight, indicating it possesses the most mobility during the task. An interesting observation in the brushing task is the significant weight on the wrist abduction/adduction joint. This joint is crucial for combing through sections of hair, necessitating the wrist joint to move nearly to its limits. However, evaluating the algorithm's performance is feasible by examining the RMS error of each joint compared to motion

capture data. The RMS errors for each joint, using two different methods LN and WLN_{CWM} are detailed in Table 6.2

The analysis of the table indicates that the aggregate RMS error for WLN_{CWM} is the lowest, with the Torso Flexion/Extension joint exhibiting the lowest RMS error (3.2659, St.D. = 0.0327) and the Elbow Pronation/Supination joint displaying the highest RMS error (14.3755, St.D. = 0.0929). To examine the algorithm's effectiveness in greater detail, comparisons are made between joint angle trajectories. Figure 6.2 presents the joint angle trajectory for the Torso Flexion/Extension, while Figure 6.3 displays the joint angle trajectory for the Elbow Pronation/Supination, with comparisons drawn from data from MoCap, LN, and WLN_{CWM} . The figures reveal that the LN method exhibits the largest deviation in the respective joint's trajectory, consistent with findings by [64] that indicate a more significant movement at the base joint compared to the distal joint. In contrast, Figure 6.2 demonstrates that the WLN_{CWM} algorithm closely aligns with the MoCap joint trajectory, indicating superior performance.

Further analysis of the WLN_{CWM} algorithm's performance involved calculating the average weights of each component of the total weight value, as presented in Table 6.3. The analysis suggests that for the motion of the Torso Flexion/Extension joint, the link weight has the most substantial influence, while joint limit and gradient weights have a minimal impact on the joint's movement. Similarly, Figure 6.3 shows that the WLN_{CWM} algorithm's performance closely matches the MoCap joint trajectory for the Elbow Pronation/Supination joint. Detailed data in Table 6.4 indicates that the link weight significantly influences this joint's motion, followed by gradient weights, which have a more substantial impact than joint limit weights.

In conclusion, the performance of the WLN_{CWM} algorithm is superior when compared to the LN method. Across the entire spectrum of joint motion, the link weight emerges as the most influential factor. Gradient weights exert a more pronounced effect on distal joints compared to base joints, contributing to the use of arm redundancy to achieve motion that closely resembles human movement.

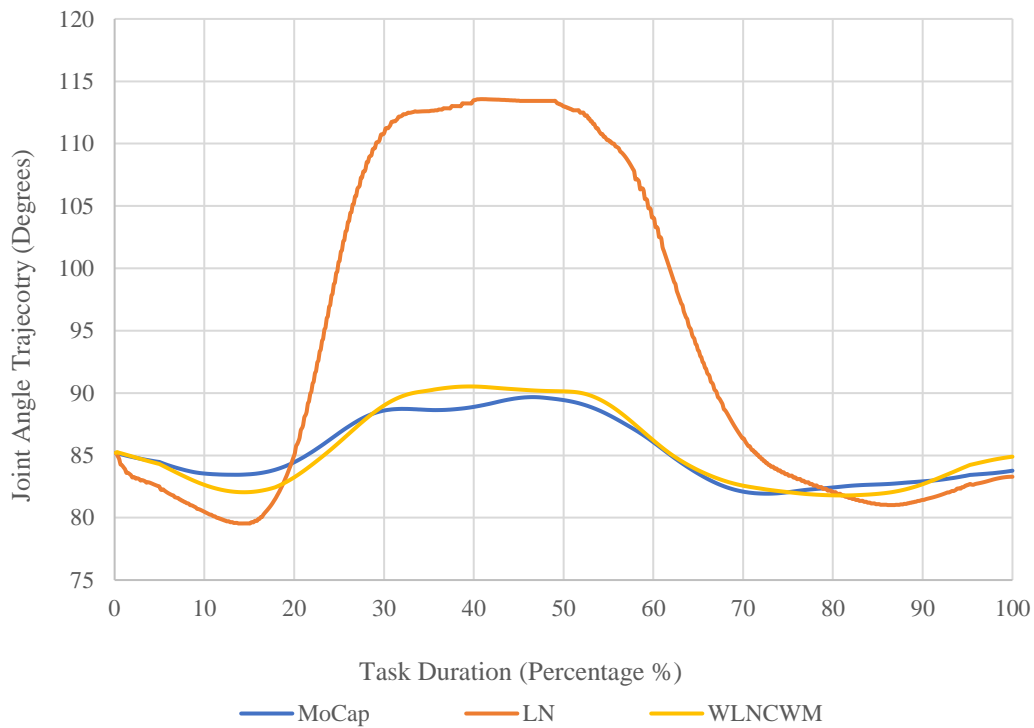


Figure 6.2 Torso flexion/extension joint trajectory for subject S06

Table 6.3 Weight distribution in the WLN_{CWM} method for torso flexion/extension joint

	Link Weight	Joint Limit	Gradient Weight
Average Weight Contribution	41.3916	0.0107	0.0218
(% Contribution)	99.92	0.03	0.05

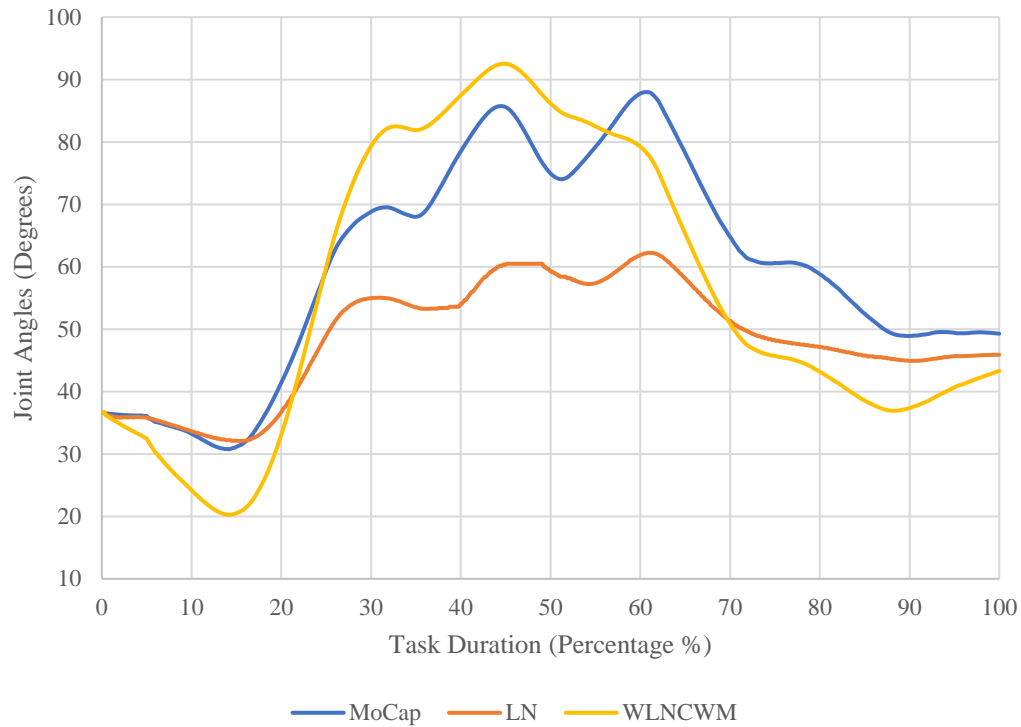


Figure 6.3 Elbow pronation/supination joint trajectory for subject S06

Table 6.4 Weight distribution in the WLNCWM method for elbow pronation/supination joint

	Link Weight (J8)	Joint Limit	Gradient Weight
Actual Weights	1.7136	0.11830	0.14368
(% Contribution)	86.74	5.99	7.27

6.2.2 Drinking from a Cup Task

The task of drinking from a cup, detailed in Section 3.7.3, involves actions similar to those in the hair-brushing task. The primary distinction lies in the motion of bringing the cup close to the mouth for the drinking task, as opposed to the motion of the hand moving behind the head in

the brushing task. The drinking task is segmented into five distinct phases, P1 through P5, as visually represented in Figure 3.15. The weighted least norm method, previously discussed, is employed to tailor weights based on diverse performance criteria, effectively managing joint motion and enabling relative motion among joints in the RHUBM model.

Section 6.1.2.1 highlights the importance of link weights in mitigating the movements of heavier joints, subsequently reducing the total torque exerted on these joints. The methodology for calculating weights based on joint limits is detailed in Section 6.1.2.2. The third element of the weight matrix involves the gradient of performance criteria, as depicted in Figure 5.4. This figure shows the evolution of normalized criteria throughout each phase of the task, aiding in the identification of performance criteria that significantly influence the algorithm's overall effectiveness. Additionally, Figure 5.5 provides insights into the shifts in selected performance criteria across different phases of the task. Specifically, the intersection of LM and AVR trajectories between the start of phase P2 and the end of phase P4, as illustrated in Figure 5.5, identifies the phases where enhancement of performance criteria is essential, aligning with the gradient of these criteria and their integration into the weight matrix, a concept detailed in Section 6.1.2.4. In the drinking from a cup task, LM is prioritized in phases P1, P4, and P5, while AVR is emphasized in phases P2 and P3. For each of the eight subjects studied, phases were distinctly marked, facilitating the computation of gradient values for the respective performance criteria for each phase. Table 6.5 presents the average total weights for these eight subjects under WLN_{CWM} . As previously discussed, weight values nearing one indicate a joint with high mobility and frequent movement. Conversely, weight values approaching infinity suggest a joint with limited mobility, indicative of minimal movement. Analysis of these weight values provides critical insights into

the operational dynamics of the joints in various tasks, identifying joints that are predominantly active or largely stationary.

Table 6.5 Average weights of eight subjects using combined weights method

Anatomical Joint	WLN_{CWM}
Torso Lateral Flexion	36.2438
Torso Flexion/Extension	36.2483
Torso Rotation	36.2548
Shoulder Horizontal Flexion/Extension	3.6045
Shoulder Abduction/Adduction	3.7499
Shoulder Rotation	3.5074
Elbow Flexion	1.6168
Elbow Pronation/Supination	1.6275
Wrist Flexion/Extension	19.4813
Wrist Abduction/Adduction	17.6568

The Table 6.5 focuses on WLN_{CWM}, reveals that torso joints have the highest weights relative to other joints, suggesting reduced movement in comparison to shoulder and elbow joints. Notably, the dominant weights in torso joints are link weights, with joint limit and gradient weights making minimal contributions to the overall performance this explained in the later section. In contrast, the Elbow Flexion joint exhibits the lowest weight, indicating it has the most mobility during the task, as extensive movement is required to complete the drinking action.

Table 6.6 Drinking from a cup task average RMS error evaluation

Anatomical Joint	LN (deg)	St.D.	WLN_{CWM} (deg)	St.D.
Torso Lateral Flexion	7.2250	0.0689	4.1941	0.0312
Torso Flexion/Extension	13.0462	0.0842	3.2086	0.0243
Torso Rotation	19.9447	0.2212	2.8762	0.0830
Shoulder Horizontal Flexion/Extension	19.7957	0.1584	7.8610	0.0497
Shoulder Abduction/Adduction	9.9465	0.0878	3.8445	0.0385
Shoulder Rotation	22.7350	0.2308	6.4229	0.2722
Elbow Flexion	18.2945	0.1918	9.5684	0.0739
Elbow Pronation/Supination	14.5199	0.1036	12.2498	0.1044
Wrist Flexion/Extension	16.3064	0.1819	5.6379	0.1531
Wrist Abduction/Adduction	21.6521	0.1447	8.7433	0.06434

An interesting observation in the drinking task is the significant weight assigned to the wrist joints, essential for grasping the cup and performing the drinking action near the mouth area, suggesting reduced movement in these joints to maintain stability while holding the cup. The algorithm's performance can be assessed by examining the RMS error of each joint against motion capture data, with RMS errors for each joint using methods LN and WLN_{CWM} detailed in Table 6.6.

The analysis of the table confirms that the aggregate RMS error for WLN_{CWM} is minimal, with the Torso Rotation joint exhibiting the lowest RMS error (2.8762, St.D. = 0.0830) and the Elbow Pronation/Supination joint recording the highest RMS error (12.2498, St.D. = 0.1044). A more nuanced examination of the algorithm's performance is achieved through the comparison of

joint angle trajectories. Figure 6.4 illustrates the joint angle trajectory for the Torso Rotation, while Figure 6.5 depicts the joint angle trajectory for the Elbow Pronation/Supination, with data comparisons drawn from MoCap, LN and WLN_{CWM}. These figures indicate that the LN method manifests the most significant deviation in the trajectory of the respective joints, corroborating findings by that highlight a greater movement at the base joint relative to the distal joint. In contrast, Figure 6.4 shows that the WLN_{CWM} algorithm's trajectory closely mirrors the MoCap joint trajectory, signifying its superior performance.

Further scrutiny of the WLN_{CWM} algorithm's efficacy involved computing the average weights of each component of the total weight value, as presented in Table 6.7. This analysis reveals that the motion of the Torso Rotation joint is predominantly influenced by the link weight, while joint limit and gradient weights exert minimal impact on the joint's motion. Similarly, Figure 6.5 demonstrates that the WLN_{CWM} algorithm's performance closely aligns with the MoCap joint trajectory for the Elbow Pronation/Supination joint. Detailed data in Table 6.8 confirms that the link weight significantly influences this joint's motion, followed by gradient weights, which exert a more considerable impact than joint limit weights.

In summary, similar to the findings in the hair-brushing task, the WLN_{CWM} algorithm's performance in the drinking from the cup task is superior when compared to the LN method. Throughout the entire spectrum of joint motion, link weight emerges as the most critical factor. Gradient weights have a more pronounced impact on distal joints compared to base joints, contributing to the effective utilization of arm redundancy to replicate motion that closely resembles human movement.

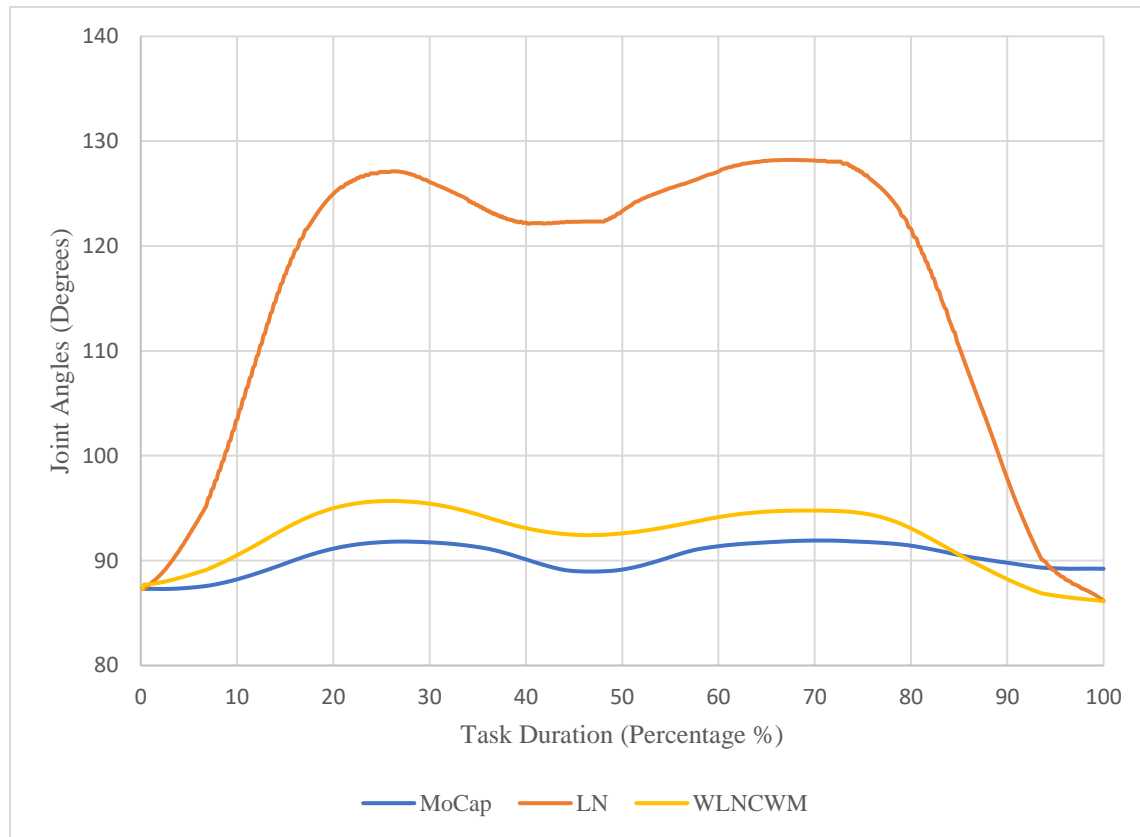


Figure 6.4 Torso rotation joint trajectory for subject S06

Table 6.7 Weight distribution in the WLN_{CWM} method for torso rotation joint

	Link Weight	Joint Limit	Gradient Weight
Actual Contribution	36.5220	0.0010	0.0126
(% Contribution)	99.963	0.003	0.034

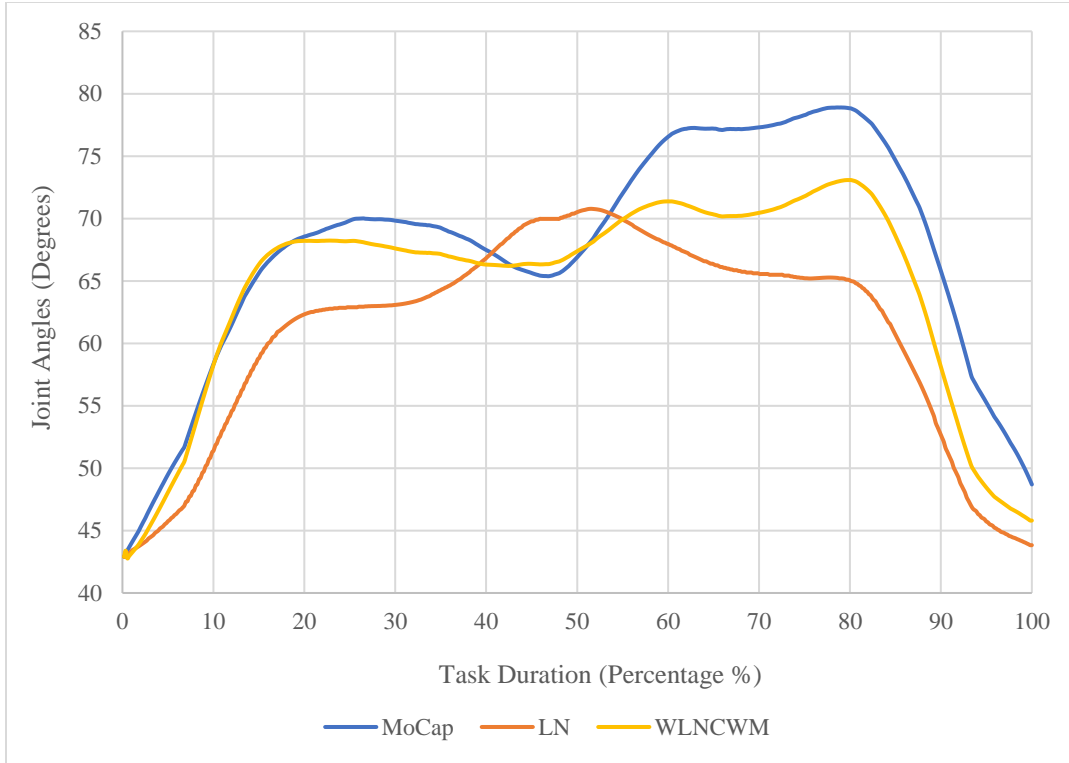


Figure 6.5 Elbow pronation/supination joint for subject S06

Table 6.8 Weight distribution in the WLN_{CWM} method for elbow pronation/supination joint

	Link Weight (J8)	Joint Limit	Gradient Weight
Actual Contribution	1.512	0.1411	0.1486
(% Contribution)	83.91	7.83	8.26

6.2.3 Opening a Higher-Level Cabinet Task

Section 3.7.4 details the Opening a Higher-Level Cabinet task, which, broken down into four distinct phases (P1 to P4), is visually represented in Figure 3.16. The WLN method, previously explored, is utilized to customize weights based on varied performance criteria, managing joint motion and facilitating relative motion among joints within the RHUBM model. Section 6.1.2.1 emphasizes the significance of link weights in reducing the movement of heavier

joints, thereby decreasing the total torque on these joints. The methodology for determining weights grounded in joint limits is specified in Section 6.1.2.2. The weight matrix's third element, the gradient of performance criteria, is portrayed in Figure 5.5. This key figure illustrates how normalized criteria evolve during each task phase, aiding in the discernment of performance criteria that substantially influence the algorithm's overall effectiveness. Moreover, Figure 5.6 sheds light on the dynamic shifts of selected performance criteria across different phases. Specifically, the intersection of LM and LVR trajectories, occurring between the onset of phase P2 and the conclusion of phase P3 as depicted in Figure 5.5, pinpoints the phases where performance criteria need to be optimized. This is aligned with the gradient of these criteria and their inclusion into the weight matrix, an approach elaborated in Section 6.1.2.3. In this task, LM takes precedence in phases P1 and P3, while LVR is emphasized in phases P2 and P4. The eight subjects' phases were distinctly labeled, enabling the calculation of gradient values for respective performance criteria for each phase. Table 6.9 tabulates the average total weights for these subjects under WLN_{CWM} . Examining these weight values provides in-depth insight into the functional dynamics of the joints in various tasks, pinpointing joints that are primarily active or largely stationary. The Table 6.9, focusing on WLN_{CWM} , shows that torso joints possess the highest weights in relation to other joints, indicating reduced movement compared to distal joints.

It's notable that torso joints primarily carry link weights, with joint limit and gradient weights contributing minimally to overall performance. Conversely, the wrist joint, indicating maximum mobility during the task, exhibits the lowest weight. This balance ensures that while heavier joints move less, lighter/distal joints perform most of the task work. Assessing the algorithm's performance involves analyzing the RMS error of each joint against motion capture data, with RMS errors for each joint detailed in Table 6.10, using methods LN and WLN_{CWM} .

Table 6.9 Average weights of eight subjects using combined weights method

Anatomical Joint	WLN_{CWM}
Torso Lateral Flexion	43.0996
Torso Flexion/Extension	43.1059
Torso Rotation	43.0992
Shoulder Horizontal Flexion/Extension	4.0965
Shoulder Abduction/Adduction	4.1086
Shoulder Rotation	4.1131
Elbow Flexion	1.8036
Elbow Pronation/Supination	1.7893
Wrist Flexion/Extension	0.4887
Wrist Abduction/Adduction	0.4699

The table analysis confirms that the cumulative RMS error for WLN_{CWM} is minimal, with the Torso Rotation joint showing the lowest RMS error (2.3434, St.D. = 0.0135) and the Elbow Pronation/Supination joint the highest (14.8052, St.D. = 0.0285). Comparing joint angle trajectories provides a more nuanced examination of the algorithm's performance. Figure 6.6 illustrates the joint angle trajectory for the Torso Rotation, while Figure 6.7 portrays the trajectory for the Elbow Pronation/Supination, with data comparisons drawn from MoCap, LN, and WLN_{CWM}. These figures corroborate that the LN method exhibits the most significant trajectory deviation, supporting [3]'s findings of greater movement at the base joint relative to distal joints.

Conversely, Figure 6.6 and Figure 6.7 shows the WLN_{CWM} algorithm's trajectory aligning closely with the MoCap joint trajectory, denoting superior performance.

Table 6.10 Opening a higher-level cabinet task average RMS error evaluation

Anatomical Joint	LN (deg)	St.D.	WLN_{CWM} (deg)	St.D.
Torso Lateral Flexion	12.1983	0.0513	5.5520	0.0448
Torso Flexion/Extension	7.0359	0.0951	3.8904	0.0328
Torso Rotation	11.5107	0.0639	2.3434	0.0135
Shoulder Horizontal Flexion/Extension	22.8381	0.0975	9.6028	0.0698
Shoulder Abduction/Adduction	11.9748	0.0655	3.2143	0.0345
Shoulder Rotation	17.0455	0.0581	9.5627	0.0525
Elbow Flexion	10.5023	0.1285	8.8407	0.0561
Elbow Pronation/Supination	25.3305	0.1386	14.8052	0.0285
Wrist Flexion/Extension	14.6162	0.0912	5.3285	0.0177
Wrist Abduction/Adduction	0.7334	0.1324	6.2510	0.0403

Further scrutiny of WLN_{CWM} algorithm's efficacy involved calculating the average weights of each component of the total weight value, as listed in Table 6.11. This analysis indicates the motion of the Torso Rotation joint is primarily driven by the link weight, with joint limit and gradient weights exerting minimal impact on the joint's motion. Figure 6.7 similarly demonstrates the WLN_{CWM} algorithm's performance closely matching the MoCap joint trajectory for the Elbow Pronation/Supination joint. Detailed data in Table 6.12 confirms that the link weight significantly

influences this joint's motion, with gradient weights exerting a greater impact than joint limit weights.

In summary, the findings in the Opening a Higher-Level Cabinet task, the performance of the WLN_{CWM} algorithm is superior compared to the LN method. Across the entire spectrum of joint motion, link weight proves to be the most influential factor. Gradient weights have a more pronounced impact on distal joints compared to base joints.

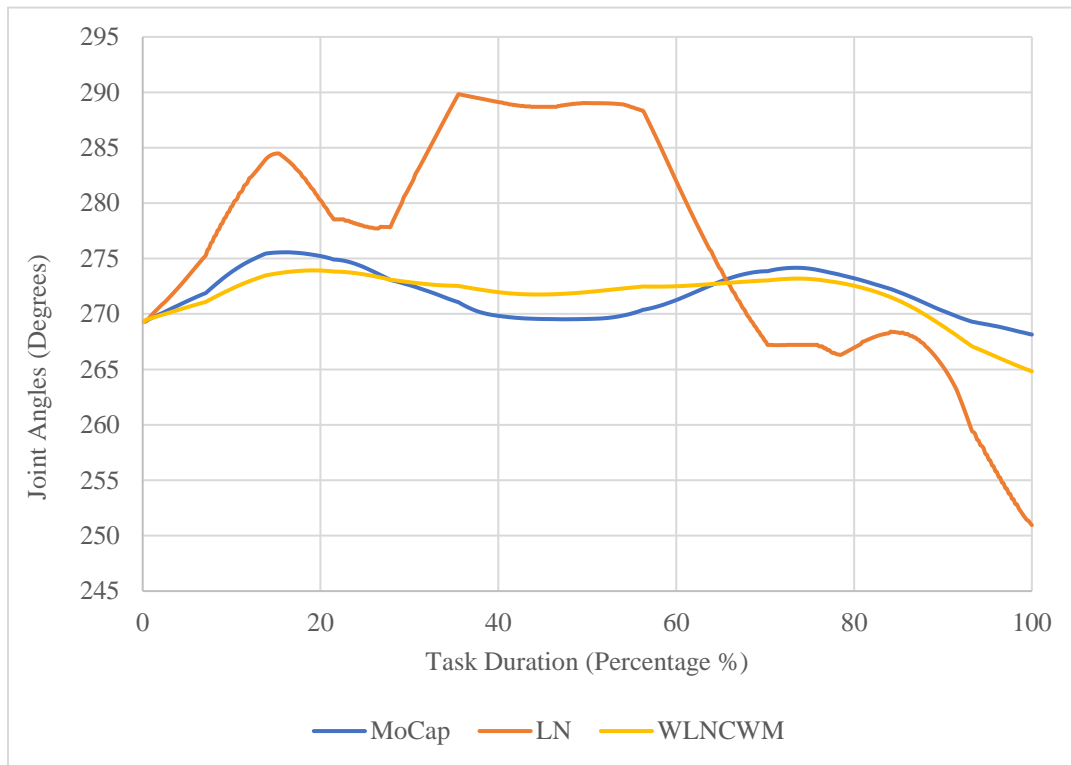


Figure 6.6 Torso rotation joint trajectory for subject S04

Table 6.11 Weight distribution in the WLN_{CWM} method for torso rotation joint

	Link Weight (J8)	Joint Limit	Gradient Weight
Actual Contribution	52.3482	0.0008	0.0076
(% Contribution)	99.9838	0.0016	0.0145

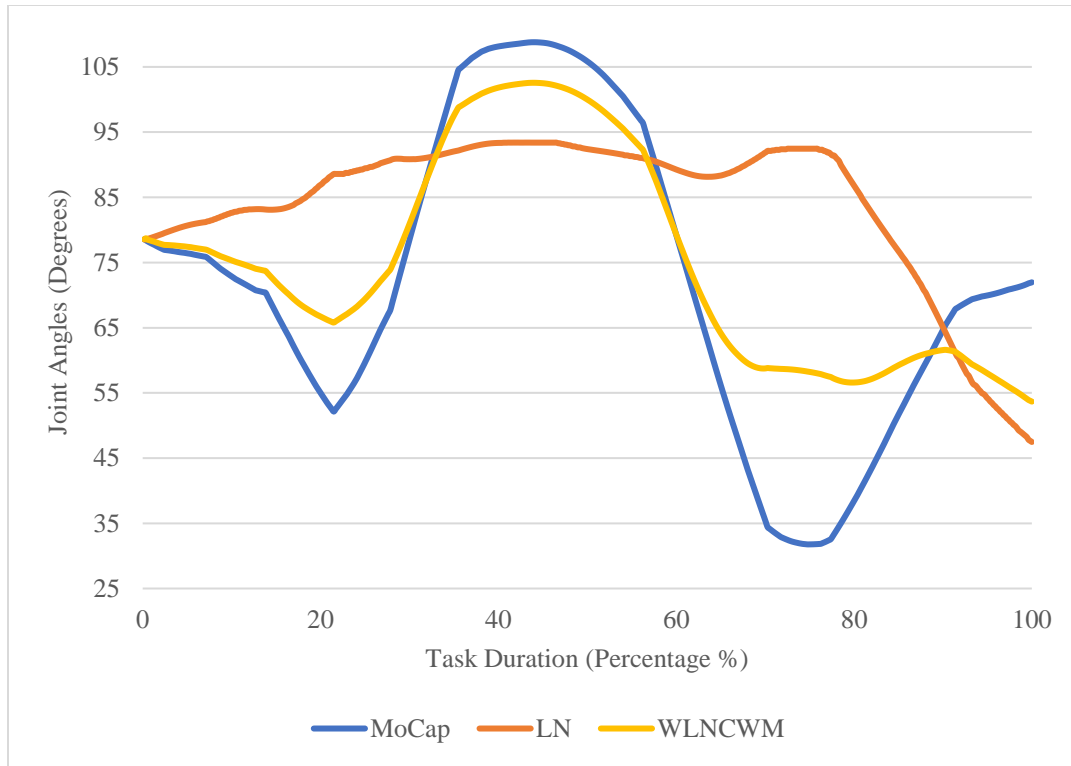


Figure 6.7 Elbow pronation/supination joint trajectory for subject S04

Table 6.12 Weight distribution in the WLN_{CWM} method for elbow pronation/supination joint

	Link Weight (J8)	Joint Limit	Gradient Weight
Actual Contribution	2.1672	0.0041	0.2595
(% Contribution)	89.1560	0.1685	10.6755

6.2.4 Picking Up a Full Water Jug for Shelving Task

Section 3.7.5 describes the results of "Picking Up a Full Water Jug for Shelving" task in detail, dividing it into four distinct steps (P1-P4) as shown in Figure 3.17. The RHUBM uses the weighted least norm method to adjust its movement based on different performance criteria. This fine-tuning allows the robot to move its joints efficiently and smoothly while achieving the necessary relative motions between them.

The discussions in Section 6.1.2.1 highlight the importance of link weights in limiting the movement of heavy joints. This, in turn, reduces the total force exerted on the arm joints. Section 6.1.2.2 explains how to calculate weights based on the limitations of each joint. This helps the robot move its joints efficiently without exceeding their limits. Additionally, the weight matrix incorporates the gradient of performance criteria as its third component. This aspect is described in Figure 5.7, which demonstrates the normalized criteria through each phase of the task, thus assisting in identifying those performance criteria that significantly lean the algorithm's comprehensive effectiveness. Furthermore, Figure 5.8 casts light on the dynamic alterations in selected performance criteria across the different phases. Particularly, the convergence of LM and LMA trajectories, as observed between the initiation of phase P2 and the end of phase P3 in Figure 5.7, marks the phases where an improvement in performance criteria, guided by their gradient and subsequent merger into the weight matrix, is crucial, a process thoroughly detailed in Section 6.1.2.3. In this specific task, priority is given to LM in phases P1 and P3, whereas LVR is given priority in phases P2 and P4. We divided the task into distinct phases for each of the eight participants. This allowed us to calculate values of different performance criteria at each phase of the task. The compilation of the average total weights for these subjects under WLN_{CWM} is presented in Table 6.13. The weight values in the WLN_{CWM} method reveal valuable information about joint movement in different tasks. Smaller weights represent joints with high mobility, while larger weights indicate joints with limited mobility. Analyzing these weight values helps understand how joints function in different tasks, showing which ones are primarily active or mostly stationary. Table 6.13 shows that torso joints have the highest weights in the WLN_{CWM} method, meaning they move less than other joints. They mainly rely on link weight, with minimal contributions from joint limit and gradient weights.

Table 6.13 Average weights of eight subjects using combined weights method

Anatomical Joint	WLN_{CWM}
Torso Lateral Flexion	38.9272
Torso Flexion/Extension	38.9773
Torso Rotation	38.9204
Shoulder Horizontal Flexion/Extension	3.7127
Shoulder Abduction/Adduction	3.7505
Shoulder Rotation	3.7249
Elbow Flexion	1.6508
Elbow Pronation/Supination	1.6137
Wrist Flexion/Extension	19.7884
Wrist Abduction/Adduction	21.0960

On the other hand, the elbow pronation/supination joint, which moves the most during the task, has the lowest weight. Interestingly, wrist weights are higher than shoulder and elbow weights, suggesting less mobility. This is likely because the wrist is close to its limits, which helps keep the hand oriented while performing the task.

To evaluate the method's effectiveness, researchers compared the predicted movement of each joint with actual motion capture data using RMS error. Figure 6.8 shows the RMS errors for each joint, employing methods LN and WLN_{CWM}.

Observing the results, we see that the WLN_{CWM} method has the lowest overall RMS error compared to LN method. The Torso Rotation joint has the smallest error (3.9821, St.D. = 0.0212), while the Shoulder Rotation joint has the largest (17.5554, St.D. = 0.1709). We can also compare

how well each method predicts the movement of each joint by looking at the joint angle trajectories. Figure 6.8 shows the trajectory for the Torso Rotation, and Figure 6.9 shows the trajectory for the Shoulder Rotation. Both figures compare to the actual MoCap with the predictions from different methods LN and WLN_{CWM}. These figures show that the LN method is the least accurate, with its predictions deviating significantly from the actual movement. In contrast, Figure 6.8 shows that the WLN_{CWM} method's trajectory closely follows the actual movement, making it the most accurate method.

Table 6.14 Picking up a full water jug for shelving task average RMS error evaluation

Anatomical Joint	LN (deg)	St.D.	WLN_{CWM} (deg)	St.D.
Torso Lateral Flexion	10.0783	0.1109	6.1135	0.0318
Torso Flexion/Extension	13.6077	0.0906	4.3201	0.0231
Torso Rotation	28.6593	0.0906	3.9821	0.0212
Shoulder Horizontal Flexion/Extension	37.0073	0.1683	11.0180	0.1668
Shoulder Abduction/Adduction	11.6941	0.0630	5.9416	0.0343
Shoulder Rotation	26.2014	0.3011	17.5554	0.1709
Elbow Flexion	23.0730	0.2502	8.1303	0.0545
Elbow Pronation/Supination	13.3843	0.0728	11.6024	0.0938
Wrist Flexion/Extension	23.5199	0.2174	9.9236	0.0756
Wrist Abduction/Adduction	20.0764	0.1804	13.8598	0.1097

To understand how well the WLN_{CWM} algorithm works, we looked at the average weight of each part of the total weight for each joint (Table 6.15). This showed that the movement of the Torso Rotation joint is mostly controlled by the link weight, with the other two types of weights

having little effect. Similarly, Figure 6.9 shows that the WLN_{CWM} algorithm predicts the movement of the Shoulder Rotation joint very accurately, similar to the MoCap. Table 6.16 confirms this, showing that the link weight has the biggest impact on this joint's movement, with the gradient weight having a larger effect than the joint limit weight.

The WLN_{CWM} algorithm demonstrates superior performance in the Picking up a Full Water Jug for Shelving task compared to the LN method. Analysis across all joint motions reveals that link weight is the most dominant factor influencing movement. Gradient weights exhibit a stronger impact on distal joints compared to base joints, effectively utilizing arm redundancy to generate motions highly resembling human movements.

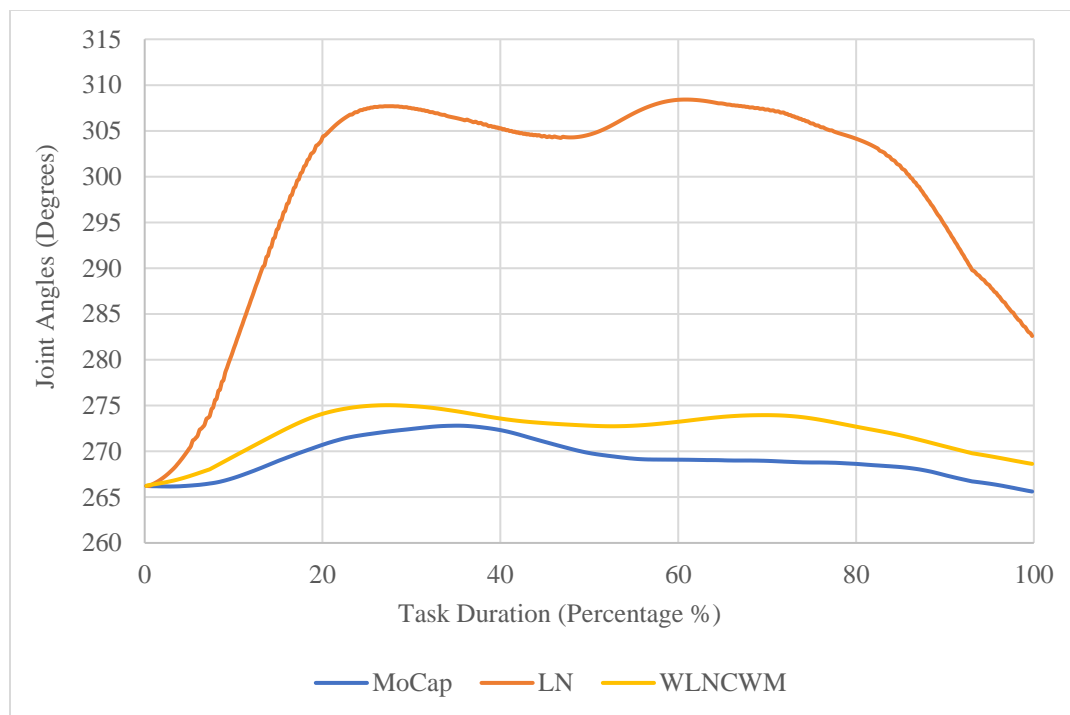


Figure 6.8 Torso rotation joint trajectory for subject S04

Table 6.15 Weight distribution in the WLN_{CWM} method for torso rotation joint

	Link Weight (J3)	Joint Limit	Gradient Weight
Actual Contribution	52.3482	0.0007	0.0636
(% Contribution)	99.8684	0.0013	0.1303

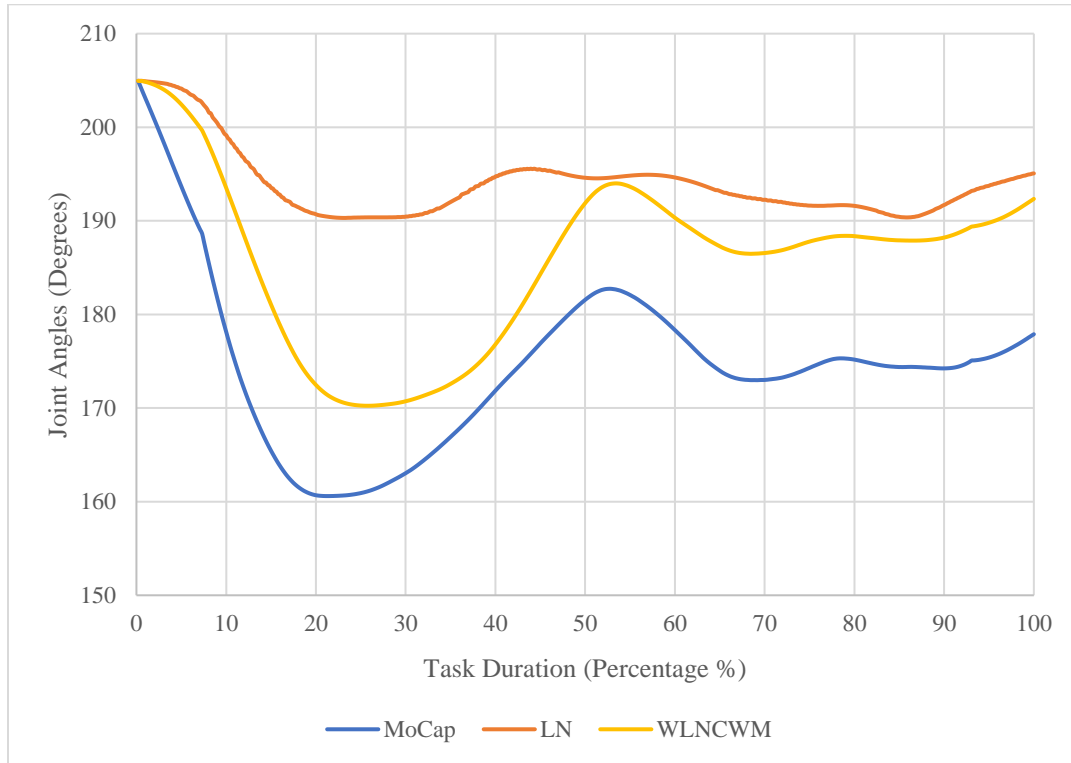


Figure 6.9 Shoulder rotation joint trajectory for subject S04

Table 6.16 Weight distribution in the WLN_{CWM} method for shoulder rotation joint

	Link Weight (J6)	Joint Limit	Gradient Weight
Actual Contribution	4.9622	0.0030	0.5778
(% Contribution)	89.5212	0.0547	10.4242

Chapter 7: Discussion and Future Works

This research explored motion planning algorithms that utilize the inherent redundancy in robotic systems, drawing inspiration from the efficient strategies humans employ during everyday activities. A dedicated framework was developed with three key objectives: ensuring humanoid robots' safe and natural motion in human environments, designing a better interface to assist prosthetic users, and aiding physiotherapists in designing rehabilitation protocols.

The central hypothesis of this research suggests that humans prioritize the movement of heavier joints and integrate various performance criteria, including manipulability, velocity ratio, and mechanical advantage, while avoiding joint limits across different phases of ADLs. Five experimental objectives were conducted to test this.

The first objective is to develop an RHUBM model based on MoCap data. The second objective is to investigate the influence of arm configurations on performance criteria using null space projection and understand how their combination governs motion. The third objective is to identify the dominant performance criteria for each task phase and derive a corresponding weight matrix. The fourth objective is to develop and implement a WLN inverse kinematics algorithm that generates human-like motion by prioritizing redundant joints based on these criteria. The fifth and final objective is to compare it with MoCap data to calculate the algorithm's accuracy in predicting human-like motion.

The designed weight matrix revealed three key components: joint load management, joint limit avoidance, and performance criteria optimization through the gradient method. These components improved algorithm accuracy and reduced reliance on MoCap data, representing a

significant advance over previous methods. Building upon the detailed findings presented earlier, this section discusses the research's overall impact, acknowledges the limitations (e.g., data size, specific applications), and proposes future directions for further investigation (e.g., expanding data scope and exploring alternative algorithms.).

7.1 Discussion

Building upon our earlier discussion of the five research objectives, this section presents the key findings from each objective. It highlights their specific contributions to the design of the weight matrix for the WLN algorithm implemented in the final phase.

The first objective is to create a subject-specific, ten-degree-of-freedom RHUBM dataset using MoCap in the OpenSim and MATLAB software platforms. The data includes eight range-of-motion (RoM) tasks and nine ADLs, recorded using an eight-camera Vicon motion analysis system.

The second objective of the study examined eight participants' performance in four specific ADLs: Brushing, Drinking from a Cup, Shelving a Heavy Object, and Opening Cabinets. Details are given in section 5.1. Diverse arm configurations were generated using null space projection methods at predetermined hand positions along the trajectory. The performance criteria values at these configurations were then analyzed and compared with those of natural human arm movements. Experimental outcomes indicated that participants selectively adopted certain arm configurations to optimize the combination of different performance criteria tailored to the demands of each specific task.

- For the Brushing task, there was a clear tendency to minimize LM and GL while maximizing AM, LVR, and AVR, as described in Table 4.1. The task of brushing entails a sequence of motions that initiate with the initial action of reaching out to grasp the

hairbrush, which has an approximate weight of 0.02 kg. Subsequently, the brush is brought into proximity with the head, followed by its maneuvering through a section of the hair, concluding with its return to the table, as illustrated in Figure 3.14. This strategic balance aims to efficiently transmit force while minimizing physical strain during the brushing task.

- In the Drinking task, a marked preference emerged to reduce overall Manipulability, VR, and GL while focusing on maximizing MA, as indicated in Table 4.2. This approach, which combines maximizing MA with minimizing GL, effectively reduces the joint load from gravitational forces, leading to a controlled and balanced performance along the trajectory.
- For the task of Opening a Higher-Level Cabinet, the selection of arm configurations at specific points emphasized maximizing AM and MA while aiming to reduce GL, as per the results described in Table 4.3. To initiate the process of opening a cabinet door, participants engage in a sequence of well-coordinated movements that encompass reaching out to grasp the door handle or knob, subsequently either pulling it towards themselves or pushing it away, as shown in Figure 3.16. Within assessing these dynamic actions throughout the cabinet door-opening task, six distinct arm postures were employed at a specific point in the task sequence. This strategy limits the impact of gravitational forces on the arm and hand, enhancing movement flexibility and reducing muscle and joint strain while ensuring stability during the task.
- In Picking Up a Full Water Jug for Shelving, the participant focused on maximizing VR and AM while making concerted efforts to reduce LM, MA, and GL, as detailed in Table 4.4. This approach seeks to counteract gravitational forces on the arm and hand, enhancing flexibility of movement and reducing potential muscle and joint strain.

Overall, the experimental findings revealed that participants consistently sought to minimize gravitational load from the weight of the links and the payload during ADL task execution, except in the brushing task, where task requirements differ. This significant observation can play a crucial role in deriving the weight matrix. Simultaneously, efforts were made to maximize the combination of various performance criteria. These observations confirm the hypothesis that humans combine and finely adjust performance criteria based on task-specific demands.

The third objective was to investigate the predominant performance criteria influencing human arm movements during a range of ADLs. A study involving eight participants focused on four specific ADLs: Brushing, Drinking from a Cup, Shelving a Heavy Object, and Opening Cabinets. Motion capture technology played a crucial role, allowing the median values of each performance criterion to be assessed during these tasks. Each task's trajectory was segmented into 4-5 phases designed for the specific ADL. SPM analysis was employed to determine the significance of these criteria throughout different phases of each task.

- For the Brushing task, comprehensive analysis pinpointed LM and AVR as central criteria across various stages of the task. Figure 5.2 illustrates the mean trajectories for LM and AVR, complete with their respective standard deviations.
- In the Drinking task, a trend mirroring the Brushing task became evident, underscoring the critical roles of LM and AVR at distinct stages of the activity. Figure 5.4 offers an in-depth examination of these crucial metrics, LM and AVR, coupled with their standard deviations and time-based t-test values.
- The task of Opening a Higher-Level Cabinet, the analysis highlighted the pronounced effects of LM and LVR on performance. Figure 5.6 provides a detailed exploration of the

relationship between LM and LVR, displaying their respective standard deviations and dynamically showcasing t-test values over time. This highlights the statistical importance of these criteria as the task unfolds.

- The task of Picking Up a Full Water Jug for Shelving, a thorough review of the data revealed the significant impact of LM and LMA on task execution. Their standard deviations are and t-test values over time presented in Figure 5.8.

The results of this phase clarify the underlying principles of motor control during ADLs by identifying the primary performance criteria employed in human arm movements. The SPM analysis of performance criteria values illuminates their relevance throughout various task phases. The findings validate the hypothesis that humans strategically fine-tune performance criteria at distinct phases of a task, effectively blending different criteria for optimal motor control. This understanding is particularly instrumental for calculating the weight matrix in the WLN algorithm.

In the fourth objective of the study, the WLN inverse kinematics algorithm was implemented. This algorithm allocates weights to each joint based on the previously identified performance criteria, prioritizing certain joints over others. This prioritization facilitates the creation of movements that closely simulate human motion. The weight matrix, established during objective 2 and 3 and utilized in objective 4, reveals three core components:

- Joint load management concentrates on regulating the load exerted on the joints. Heavier joints, such as the Torso, receive higher weights according to the link weights. Described in Section 6.1.2.1 and Table 3.4, this method details the computation of weights associated with each link segment. By diminishing the movement of heavier joints compared to their lighter counterparts, the overall strain on the joints and muscles is effectively reduced.

- Joint limit avoidance ensures that joint movements are confined within safe and pre-established boundaries. The methodologies for joint limit avoidance, thoroughly outlined in Section 6.1.2.2 and explained through Equations 6.13 and 6.14.
- Performance criteria optimization by utilizing gradient-based weights refines specific performance criteria during different phases of a task. These criteria, pinpointed in Phase 2, undergo optimization to boost the robot's overall performance significantly. Section 6.1.2.3 offers a comprehensive description of this optimization process, with Equation 6.19 explaining the numerical method used for weight calculation.

In the fifth objective, the MoCap data is utilized as a benchmark to evaluate the outcomes obtained by the WLN_{CWM} algorithm. The method's effectiveness is gauged in comparison with the standard LN method. The comparisons yield insightful observations:

- The LN method's results reveal a significant bias towards proximal joints, with weightings favoring torso joints over wrist joints. This prioritization aims to maximize end-effector movement while minimizing total joint movement. However, this differs from human movement strategies, which distribute weights variably across joints. This distribution creates relative motion among different joints to optimize specific combination of performance criteria.
- When integrating link weights, joint limit criteria weights, and gradient-based weights, the WLN_{CWM} algorithm demonstrates enhanced accuracy.
- In the task examined, it was observed that WLN_{CWM} achieved the lowest RMS error in comparison to LN. This outcome suggests that optimizing performance criteria phase-wise yields greater accuracy than applying a single criterion optimization across the entire task trajectory. Understanding the prominent performance criteria at various phases of the task

enables the development of optimal motion control for any novel tasks. By dividing the trajectory of a novel task into smaller segments, optimal performance criteria can be extrapolated from phases of previously analyzed similar tasks. This approach facilitates the formulation of a motion planning algorithm that closely emulates human-like movement.

- The performance of WLN_{CWM} is notably influenced by the fine-tuning parameter, as indicated in Equation 6.19. This parameter's variability across different participants and ADLs enables researchers to tailor the weight matrix to cater to specific task needs. Identifying optimal values for this parameter emerges as a promising area for future research.
- For tasks like lifting a full water jug where the end-effector must handle significant weight and complete the movement, link weights are prioritized in the weight matrix. This prioritization reflects the primary goal of balancing heavy objects and minimizing joint and muscle strain.

7.2 Limitation

While this study offers valuable insights, future work could address several limitations as described below to enhance the accuracy and generalizability of the results.

- The study included only eight participants performing nine ADLs. This limited the ability to comprehensively analyze human arm motion and apply findings to inverse kinematics algorithms. Expanding the participant pool and diversifying the ADLs could lead to more robust and generalizable motion planning algorithms.
- Most ADLs in this study involved minimal torso movement, which limited our understanding of tasks with more significant torso engagement. Expanding the dataset to include diverse ADLs with greater torso involvement will help address this limitation.

- This work primarily concentrated on single-hand movements, overlooking bimanual tasks. Incorporating a wider range of ADLs that involve bilateral arm coordination in future research will enhance both our knowledge and the robustness of our algorithms.
- While the algorithm considered manipulability, velocity ratio, and mechanical advantage, it's essential to recognize that humans might subconsciously optimize other criteria, such as muscle energy or jerk minimization. Incorporating additional performance criteria could lead to more robust and accurate motion planning algorithms.
- The accuracy of the algorithm heavily depends on the fine-tuning parameter in Equation 6.19, which varies across participants and tasks. Investigating and understanding this variability using advanced machine learning algorithms presents a promising avenue for future research.

7.3 Contribution

The research presented contributes significantly to applied robotics, particularly in the fields of humanoid motion, human body modeling, and biomechanics. The specific areas of contribution include.

- This research study provides a dataset of human movements performing ADLs. The data were collected using a Vicon motion capture system. This data was used to create personalized 3D models of each participant within the OpenSim framework. Additionally, the data allowed for calculating joint angles within the same software, which could then be applied to a robotic model created in MATLAB. The dataset includes nine ADLs and eight exercises for flexibility (Range of Motion) performed by ten healthy individuals. Each action was repeated twice, resulting in 340 total demonstrations. The entire database is publicly available through the Center for Assistive, Rehabilitation, and Robotics

Technologies (CARRT) under the name "CARRT-Motion Capture Data for Robotic Human Upper Body Model." The data include raw motion data (.c3d format), processed data for OpenSim (.trc format), and additional processed data for the MATLAB model.

- Analysis of four out of nine ADLs revealed the performance criteria humans prioritize during different task phases. These findings inform not only the weight matrix design for the WLN algorithm but also potentially other redundancy resolution methods.
- This study compared two methods for controlling the RHUBM: the LN and the WLN_{CWM} . Among these, the WLN_{CWM} method demonstrated the highest accuracy in predicting human arm motion without relying on MoCap data for weight calculations.

The implications of this study are far-reaching and hold significance across multiple domains. In robotics and biomechanics, the insights acquired can shape the development of advanced trajectory-planning algorithms designed for humanoid robots, leading to more efficient and humanlike movements. Similarly, individuals reliant on prosthetic devices can anticipate enhanced designs grounded in natural motion principles, which will elevate their engagement with their surroundings and daily activities. Moreover, given the inherent limitations in the degrees of freedom of prosthetic devices, individuals can partake in training sessions featuring optimized motions to minimize the risk of injuries arising from unintended compensatory movements. Furthermore, this research offers pragmatic applications in rehabilitation training programs. Tailored exercises harmonizing with natural motion patterns are poised to accelerate recovery and amplify motor skills.

7.4 Future Work

This section outlines potential avenues for future research, building upon the findings of this study.

- To enrich the understanding of human movement patterns and extend the generalizability of the findings, it is recommended to expand the current dataset. This expansion could involve recruiting more participants, incorporating tasks with significant torso involvement and bimanual coordination, and exploring activities from diverse domains, such as occupational or recreational activities.
- Utilizing the OpenSim musculoskeletal model, future research could focus on analyzing muscle energy expenditure and incorporating muscle length as a performance criterion. Such analysis would facilitate the study of muscle fatigue and its influence on movement optimization strategies.
- Further analysis and exploration of additional performance criteria governing human arm motion could reveal deeper insights into the complex interplay between these factors and their importance across different task phases. This could involve investigating criteria related to metabolic cost, safety, and coordination, among others.
- The availability of a larger and more diverse dataset could be instrumental in training supervised learning models to predict arm movements. Such models could not only reproduce movements based on learned patterns but also assist in optimizing the fine-tuning parameters of the WLN_{CWM} algorithm.
- This research holds significant potential for applications in the fields of prosthetics and rehabilitation. To translate this into practical clinical use, the creation of a graphical user interface (GUI) is crucial. This interface will facilitate the iterative analysis of the simulation tool, assisting therapists in comprehending patients' compensatory motions and recommending more human-like motion alternatives. Furthermore, it is essential that the interface includes an automated system capable of interpreting and converting model data

into outcomes relevant to clinical settings. The development of such an intuitive and accessible interface marks a critical advancement in converting this research into a functional and valuable tool for clinical applications.

References

- [1] Bar-Cohen, Y., *Biomimetics: biologically inspired technologies*. 2005: CRC press.
- [2] Welfare, K.S., et al. *Consider the human work experience when integrating robotics in the workplace*. in *2019 14th ACM/IEEE international conference on human-robot interaction (HRI)*. 2019. IEEE.
- [3] Menychtas, D., et al. *Upper limb motion simulation algorithm for prosthesis prescription and training*. in *2019 IEEE/RSJ International Conference on Intelligent Robots and Systems (IROS)*. 2019. IEEE.
- [4] Lura, D.J., *The creation of a robotics based human upper body model for predictive simulation of prostheses performance*. 2012: University of South Florida.
- [5] Žlajpah, L.J.M. and C.i. Simulation, *Simulation in robotics*. 2008. **79**(4): p. 879-897.
- [6] Trivedi, U., et al., *Biomimetic Approaches for Human Arm Motion Generation: Literature Review and Future Directions*. 2023. **23**(8): p. 3912.
- [7] Silva, E.C., et al., *Towards human-like bimanual movements in anthropomorphic robots: a nonlinear optimization approach*. 2015.
- [8] Richter, C., et al., *Musculoskeletal robots: scalability in neural control*. 2016. **23**(4): p. 128-137.
- [9] Holzbaur, K.R., W.M. Murray, and S.L.J.A.o.b.e. Delp, *A model of the upper extremity for simulating musculoskeletal surgery and analyzing neuromuscular control*. 2005. **33**: p. 829-840.

- [10] Fan, J., J. Jin, and Q. Wang. *Humanoid muscle-skeleton robot arm design and control based on reinforcement learning*. in *2020 15th IEEE Conference on Industrial Electronics and Applications (ICIEA)*. 2020. IEEE.
- [11] Al Borno, M., J.L. Hicks, and S.L. Delp, *The effects of motor modularity on performance, learning and generalizability in upper-extremity reaching: a computational analysis*. J R Soc Interface, 2020. **17**(167): p. 20200011.
- [12] Lenarcic, J., M.J.I.T.o.R. Stanisic, and Automation, *A humanoid shoulder complex and the humeral pointing kinematics*. 2003. **19**(3): p. 499-506.
- [13] Sapiro, V.D., J. Warren, and O. Khatib, *Predicting reaching postures using a kinematically constrained shoulder model*, in *Advances in robot kinematics*. 2006, Springer. p. 209-218.
- [14] Chan, M., et al., *An experimentally confirmed statistical model on arm movement*. 2004. **22**(6): p. 631-648.
- [15] Gams, A. and J. Lenarcic. *Humanoid arm kinematic modeling and trajectory generation*. in *The First IEEE/RAS-EMBS International Conference on Biomedical Robotics and Biomechatronics, 2006. BioRob 2006*. 2006. IEEE.
- [16] Tomić, M., et al., *Human to humanoid motion conversion for dual-arm manipulation tasks*. Robotica, 2018. **36**(8): p. 1167-1187.
- [17] Bogue, R., *Humanoid robots from the past to the present*. Industrial Robot: the international journal of robotics research and application, 2020. **47**(4): p. 465-472.
- [18] Calinon, S. and A. Billard. *Incremental learning of gestures by imitation in a humanoid robot*. in *Proceedings of the ACM/IEEE international conference on Human-robot interaction*. 2007.

- [19] Alibeigi, M., S. Rabiee, and M.N. Ahmadabadi, *Inverse Kinematics Based Human Mimicking System using Skeletal Tracking Technology*. Journal of Intelligent & Robotic Systems, 2016. **85**(1): p. 27-45.
- [20] Elbasiony, R. and W.J.I.S.R. Gomaa, *Humanoids skill learning based on real-time human motion imitation using Kinect*. 2018. **11**(2): p. 149-169.
- [21] Chen, P., et al. *Dimensionality Reduction for Motion Planning of Dual-arm Robots*. in *2018 IEEE International Conference on Mechatronics and Automation (ICMA)*. 2018. IEEE.
- [22] Suárez, R., J. Rosell, and N. Garcia. *Using synergies in dual-arm manipulation tasks*. in *2015 IEEE International Conference on Robotics and Automation (ICRA)*. 2015. IEEE.
- [23] Shepherd, S., A.J.R.F.i.A. Buchstab, Art, and Design, *Kuka robots on-site*. 2014: p. 373-380.
- [24] e Silva, E.C., et al., *Human-Like Movement of an Anthropomorphic Robot: Problem Revisited*. 2011. p. 779-782.
- [25] Liarokapis, M., et al., *Deriving Humanlike Arm Hand System Poses*. Journal of Mechanisms and Robotics, 2017. **9**(1).
- [26] MATLAB, F.A.I., *Robotics, Vision And Control: Fundamental Algorithms In MATLAB (Springer Tracts In Advanced Robotics) PDF*.
- [27] Delp, S.L., et al., *OpenSim: open-source software to create and analyze dynamic simulations of movement*. 2007. **54**(11): p. 1940-1950.
- [28] Billard, A., M.J.J.R. Matarić, and A. Systems, *Learning human arm movements by imitation:: Evaluation of a biologically inspired connectionist architecture*. 2001. **37**(2-3): p. 145-160.

- [29] Kim, Y., et al., *Similarities and differences between musculoskeletal simulations of OpenSim and AnyBody modeling system*. 2018. **32**: p. 6037-6044.
- [30] Fox, A.S., et al., *Simulating the effect of glenohumeral capsulorrhaphy on kinematics and muscle function*. J Orthop Res, 2021. **39**(4): p. 880-890.
- [31] Kashi, B., et al. *Synthesizing two criteria for redundancy resolution of human arm in point tasks*. in *2011 Third World Congress on Nature and Biologically Inspired Computing*. 2011. IEEE.
- [32] Kim, H. and J. Rosen, *Predicting Redundancy of a 7 DOF Upper Limb Exoskeleton Toward Improved Transparency between Human and Robot*. Journal of Intelligent & Robotic Systems, 2015. **80**(S1): p. 99-119.
- [33] Quigley, M., et al. *ROS: an open-source Robot Operating System*. in *ICRA workshop on open source software*. 2009. Kobe, Japan.
- [34] Todorov, E., T. Erez, and Y. Tassa. *Mujoco: A physics engine for model-based control*. in *2012 IEEE/RSJ international conference on intelligent robots and systems*. 2012. IEEE.
- [35] Kemp, C.C., et al., *Challenges for robot manipulation in human environments [grand challenges of robotics]*. 2007. **14**(1): p. 20-29.
- [36] Wisspeintner, T., et al., *RoboCup@ Home: Scientific competition and benchmarking for domestic service robots*. 2009. **10**(3): p. 392-426.
- [37] Gonzalez-Aguirre, J.A., et al., *Service robots: Trends and technology*. 2021. **11**(22): p. 10702.
- [38] Su, H., et al., *Online human-like redundancy optimization for tele-operated anthropomorphic manipulators*. International Journal of Advanced Robotic Systems, 2018. **15**(6).

- [39] Liu, W., D. Chen, and J. Steil, *Analytical Inverse Kinematics Solver for Anthropomorphic 7-DOF Redundant Manipulators with Human-Like Configuration Constraints*. Journal of Intelligent & Robotic Systems, 2016. **86**(1): p. 63-79.
- [40] Artemiadis, P.K., P.T. Katsiaris, and K.J. Kyriakopoulos, *A biomimetic approach to inverse kinematics for a redundant robot arm*. Autonomous Robots, 2010. **29**(3-4): p. 293-308.
- [41] Kim, C., et al. *Regenerating human-like arm motions of humanoid robots for a movable object*. in *SICE Annual Conference 2007*. 2007. IEEE.
- [42] Chen, W., C. Xiong, and S.J.I.T.o.C. Yue, *On configuration trajectory formation in spatiotemporal profile for reproducing human hand reaching movement*. 2015. **46**(3): p. 804-816.
- [43] Albrecht, S., et al. *Imitating human reaching motions using physically inspired optimization principles*. in *2011 11th IEEE-RAS International Conference on Humanoid Robots*. 2011. IEEE.
- [44] Zanchettin, A.M., L. Bascetta, and P. Rocco, *Achieving Humanlike Motion: Resolving Redundancy for Anthropomorphic Industrial Manipulators*. IEEE Robotics & Automation Magazine, 2013. **20**(4): p. 131-138.
- [45] Lamperti, C., A.M. Zanchettin, and P. Rocco, *A redundancy resolution method for an anthropomorphic dual-arm manipulator based on a musculoskeletal criterion*, in *2015 IEEE/RSJ International Conference on Intelligent Robots and Systems (IROS)*. 2015. p. 1846-1851.

- [46] García, N., J. Roseli, and R. Suárez. *Modeling human-likeness in approaching motions of dual-arm autonomous robots*. in *2018 IEEE International Conference on Simulation, Modeling, and Programming for Autonomous Robots (SIMPAR)*. 2018. IEEE.
- [47] Shin, S.Y. and C.J.I.T.o.I.E. Kim, *Human-like motion generation and control for humanoid's dual arm object manipulation*. 2014. **62**(4): p. 2265-2276.
- [48] Zanchettin, A.M., et al. *Kinematic analysis and synthesis of the human arm motion during a manipulation task*. in *2011 IEEE International Conference on Robotics and Automation*. 2011. IEEE.
- [49] Wang, Y., *Closed-form inverse kinematic solution for anthropomorphic motion in redundant robot arms*. 2013, Arizona State University.
- [50] Ding, X. and C. Fang, *A Novel Method of Motion Planning for an Anthropomorphic Arm Based on Movement Primitives*. IEEE/ASME Transactions on Mechatronics, 2013. **18**(2): p. 624-636.
- [51] Kim, H., et al., *Redundancy resolution of the human arm and an upper limb exoskeleton*. 2012. **59**(6): p. 1770-1779.
- [52] Zhao, J., B. Xie, and C. Song, *Generating human-like movements for robotic arms*. Mechanism and Machine Theory, 2014. **81**: p. 107-128.
- [53] Lura, D., et al. *Probability density based gradient projection method for inverse kinematics of a robotic human body model*. in *2012 Annual International Conference of the IEEE Engineering in Medicine and Biology Society*. 2012. IEEE.
- [54] Poignant, A., et al. *Computing the positioning error of an upper-arm robotic prosthesis from the observation of its wearer's posture*. in *2021 IEEE International Conference on Robotics and Automation (ICRA)*. 2021. IEEE.

- [55] Xie, B., J. Zhao, and Y. Liu. *Human-like motion planning for robotic arm system*. in *2011 15th International Conference on Advanced Robotics (ICAR)*. 2011. IEEE.
- [56] Jacquier-Bret, J., P. Gorce, and N. Rezzoug, *The manipulability: a new index for quantifying movement capacities of upper extremity*. *Ergonomics*, 2012. **55**(1): p. 69-77.
- [57] Jaquier, N., et al. *Geometry-aware Tracking of Manipulability Ellipsoids*. in *Robotics: Science and Systems*. 2018.
- [58] Jaquier, N., L. Rozo, and S. Calinon. *Analysis and transfer of human movement manipulability in industry-like activities*. in *2020 IEEE/RSJ International Conference on Intelligent Robots and Systems (IROS)*. 2020. IEEE.
- [59] Sentis, L. and O. Khatib. *Task-oriented control of humanoid robots through prioritization*. in *IEEE International Conference on Humanoid Robots*. 2004.
- [60] Whitney, D.E.J.I.T.o.m.-m.s., *Resolved motion rate control of manipulators and human prostheses*. 1969. **10**(2): p. 47-53.
- [61] Liegeois, A.J.I.t.o.s., man, and cybernetics, *Automatic supervisory control of the configuration and behavior of multibody mechanisms*. 1977. **7**(12): p. 868-871.
- [62] Chan, T.F., R.V.J.I.T.o.R. Dubey, and Automation, *A weighted least-norm solution based scheme for avoiding joint limits for redundant joint manipulators*. 1995. **11**(2): p. 286-292.
- [63] Lura, D.J., S.L. Carey, and R.V. Dubey, *Joint Limit vs. Optimized Weighted Least Norm Methods in Predicting Upper Body Posture*, in *Converging Clinical and Engineering Research on Neurorehabilitation*. 2013. p. 799-803.
- [64] Menychtas, D., et al. *A robotic human body model with joint limits for simulation of upper limb prosthesis users*. in *2016 IEEE/RSJ International Conference on Intelligent Robots and Systems (IROS)*. 2016. IEEE.

- [65] Gielniak, M.J., C.K. Liu, and A.L. Thomaz, *Generating human-like motion for robots*. The International Journal of Robotics Research, 2013. **32**(11): p. 1275-1301.
- [66] Kashima, T., K.J.A.I. Hori, and robotics, *Control of biomimetic robots based on analysis of human arm trajectories in 3D movements*. 2016. **21**(1): p. 24-30.
- [67] Ishida, S., et al. *Human motion imitation using optimal control with time-varying weights*. in *2021 IEEE/RSJ international conference on intelligent robots and systems (IROS)*. 2021. IEEE.
- [68] Choi, S. and J. Kim. *Towards a natural motion generator: A pipeline to control a humanoid based on motion data*. in *2019 IEEE/RSJ International Conference on Intelligent Robots and Systems (IROS)*. 2019. IEEE.
- [69] Rosado, J., et al. *Reproduction of human arm movements using Kinect-based motion capture data*. in *2013 IEEE international conference on robotics and biomimetics (ROBIO)*. 2013. IEEE.
- [70] Kim, H., et al. *Resolving the redundancy of a seven dof wearable robotic system based on kinematic and dynamic constraint*. in *2012 IEEE international conference on robotics and automation*. 2012. IEEE.
- [71] Vetter, P., T. Flash, and D.M.J.C.B. Wolpert, *Planning movements in a simple redundant task*. 2002. **12**(6): p. 488-491.
- [72] Sha, D. and J.S. Thomas, *An optimisation-based model for full-body upright reaching movements*. Comput Methods Biomech Biomed Engin, 2015. **18**(8): p. 847-60.
- [73] Al Borno, M., et al., *High-fidelity musculoskeletal modeling reveals that motor planning variability contributes to the speed-accuracy tradeoff*. Elife, 2020. **9**.

- [74] Khatib, O., et al. *Human-like motion from physiologically-based potential energies*. in *On advances in robot kinematics*. 2004. Springer.
- [75] Hua, J., et al., *Learning for a robot: Deep reinforcement learning, imitation learning, transfer learning*. 2021. **21**(4): p. 1278.
- [76] Fang, B., et al., *Survey of imitation learning for robotic manipulation*. 2019. **3**: p. 362-369.
- [77] Park, G.-R. and C. Kim. *Constructing of optimal database structure by imitation learning based on evolutionary algorithm*. in *2010 IEEE/RSJ International Conference on Intelligent Robots and Systems*. 2010. IEEE.
- [78] Wei, Y. and J.J.R. Zhao, *Designing human-like behaviors for anthropomorphic arm in humanoid robot NAO*. 2020. **38**(7): p. 1205-1226.
- [79] Su, H., et al., *Deep Neural Network Approach in Human-Like Redundancy Optimization for Anthropomorphic Manipulators*. IEEE Access, 2019. **7**: p. 124207-124216.
- [80] Su, H., et al. *Machine learning driven human skill transferring for control of anthropomorphic manipulators*. in *2020 5th International Conference on Advanced Robotics and Mechatronics (ICARM)*. 2020. IEEE.
- [81] Wen, S., et al. *Pose Analysis of Humanoid Robot Imitation Process Based on Improved MLP Network*. in *2019 WRC Symposium on Advanced Robotics and Automation (WRC SARA)*. 2019. IEEE.
- [82] Kratzer, P., M. Toussaint, and J. Mainprice. *Prediction of human full-body movements with motion optimization and recurrent neural networks*. in *2020 IEEE International Conference on Robotics and Automation (ICRA)*. 2020. IEEE.
- [83] Xie, Z., et al., *Robot learning from demonstration for path planning: a review*. 2020. **63**(8): p. 1325-1334.

- [84] Liu, Z., et al. *Learning arm movements of target reaching for humanoid robot*. in *2015 IEEE International Conference on Information and Automation*. 2015. IEEE.
- [85] Guenter, F., et al., *Reinforcement learning for imitating constrained reaching movements*. *Advanced Robotics*, 2012. **21**(13): p. 1521-1544.
- [86] Lim, B., S. Ra, and F.C. Park. *Movement primitives, principal component analysis, and the efficient generation of natural motions*. in *Proceedings of the 2005 IEEE international conference on robotics and automation*. 2005. IEEE.
- [87] Jenkins, O.C., M.J. Mataric, and S. Weber. *Primitive-based movement classification for humanoid imitation*. in *Proceedings, First IEEE-RAS International Conference on Humanoid Robotics (Humanoids-2000)*. 2000.
- [88] Yang, A., et al., *Humanoid motion planning of robotic arm based on human arm action feature and reinforcement learning*. *Mechatronics*, 2021. **78**.
- [89] Chang, P.H., *A Dexterity Measure for the Kinematic Control of Robot Manipulator with Redundancy*. 1988.
- [90] Yoshikawa, T.J.T.i.j.o.R.R., *Manipulability of robotic mechanisms*. 1985. **4**(2): p. 3-9.
- [91] Lenarcic, J. and F. Thomas, *Advances in robot kinematics: theory and applications*. 2002: Kluwer Academic Publishers.
- [92] Spong, M.W. and M. Vidyasagar, *Robot dynamics and control*. 2008: John Wiley & Sons.
- [93] Cardou, P., S. Bouchard, and C.J.I.T.o.R. Gosselin, *Kinematic-sensitivity indices for dimensionally nonhomogeneous jacobian matrices*. 2010. **26**(1): p. 166-173.
- [94] Patel, S., T.J.J.o.I. Sobh, and R. Systems, *Manipulator performance measures-a comprehensive literature survey*. 2015. **77**: p. 547-570.


- [95] Berret, B., et al., *Evidence for composite cost functions in arm movement planning: an inverse optimal control approach*. 2011. **7**(10): p. e1002183.
- [96] Feuer, A. and A.J.I.T.o.A.C. Morse, *Adaptive control of single-input, single-output linear systems*. 1978. **23**(4): p. 557-569.
- [97] Asada, H. and J. Granito. *Kinematic and static characterization of wrist joints and their optimal design*. in *Proceedings. 1985 IEEE International Conference on Robotics and Automation*. 1985. IEEE.
- [98] Dubey, R. and J. Luh. *Redundant robot control for higher flexibility*. in *Proceedings. 1987 IEEE International Conference on Robotics and Automation*. 1987. IEEE.
- [99] Dubey, R. and J.Y.J.J.o.r.s. Luh, *Redundant robot control using task based performance measures*. 1988. **5**(5): p. 409-432.
- [100] *Vicon Motion Capture System*. 2023 2023; Available from: <https://www.vicon.com/>.
- [101] Rajagopal, A., et al., *Full-body musculoskeletal model for muscle-driven simulation of human gait*. 2016. **63**(10): p. 2068-2079.
- [102] Magermans, D., et al., *Requirements for upper extremity motions during activities of daily living*. 2005. **20**(6): p. 591-599.
- [103] BUCKS, R.S., et al., *Assessment of activities of daily living in dementia: development of the Bristol Activities of Daily Living Scale*. 1996. **25**(2): p. 113-120.
- [104] Edemekong, P.F., et al., *Activities of daily living*. 2019.
- [105] Denavit, J. and R.S. Hartenberg, *A kinematic notation for lower-pair mechanisms based on matrices*. 1955.
- [106] *Weight of Human Body Parts as Percentages of Total Body Weight*. 2023; Available from: https://robslink.com/SAS/democd79/body_part_weights.htm

- [107] Trivedi, U., R. Alqasemi, and R.J.S. Dubey, *CARRT—Motion Capture Data for Robotic Human Upper Body Model*. 2023. **23**(20): p. 8354.
- [108] Alqasemi, R.M., *Maximizing manipulation capabilities of persons with disabilities using a smart 9-degree-of-freedom wheelchair-mounted robotic arm system*. 2007: University of South Florida.
- [109] Friston, K.J.J.N.d.a.p.g., *Statistical parametric mapping*. 2003: p. 237-250.
- [110] Friston, K.J., et al., *Statistical parametric maps in functional imaging: a general linear approach*. 1994. **2**(4): p. 189-210.
- [111] Worsley, K.J., et al., *A unified statistical approach for determining significant signals in images of cerebral activation*. 1996. **4**(1): p. 58-73.
- [112] Pataky, T.C., M.A. Robinson, and J.J.J.o.b. Vanrenterghem, *Vector field statistical analysis of kinematic and force trajectories*. 2013. **46**(14): p. 2394-2401.
- [113] Pataky, T.C., J. Vanrenterghem, and M.A.J.J.o.b. Robinson, *Zero-vs. one-dimensional, parametric vs. non-parametric, and confidence interval vs. hypothesis testing procedures in one-dimensional biomechanical trajectory analysis*. 2015. **48**(7): p. 1277-1285.
- [114] Pataky, T.C.J.C.m.i.b. and b. engineering, *One-dimensional statistical parametric mapping in Python*. 2012. **15**(3): p. 295-301.

Appendix A: Copyright Permissions

The permission below is for the use of material in Chapter 2 and 3.

MDPI Open Access Information and Policy

All articles published by MDPI are made immediately available worldwide under an open access license. This means: 

- everyone has free and unlimited access to the full-text of *all* articles published in MDPI journals;
- everyone is free to re-use the published material if proper accreditation/citation of the original publication is given;
- open access publication is supported by the authors' institutes or research funding agencies by payment of a comparatively low **Article Processing Charge (APC)** ([/about/apc](#)) for accepted articles.

Permissions

No special permission is required to reuse all or part of article published by MDPI, including figures and tables. For articles published under an open access Creative Common CC BY license, any part of the article may be reused without permission provided that the original article is clearly cited. Reuse of an article does not imply endorsement by the authors or MDPI.

Appendix B: Institutional Review Board Document



APPROVAL

November 21, 2022

On 11/21/2022, the IRB reviewed and approved the following protocol:

Application Type:	Initial Study
IRB ID:	STUDY004898
Review Type:	Expedited 4, 6
Title:	Study Biomechanics of Human Motion
Funding:	None
IND, IDE, or HDE:	None
Approved Protocol and Consent(s)/Assent(s):	<ul style="list-style-type: none">• IRB_Biomechanics Experiment Protocol;• Consent Form; <p>Approved study documents can be found under the 'Documents' tab in the main study workspace. Use the stamped consent found under the 'Last Finalized' column under the 'Documents' tab.</p>

Within 30 days of the anniversary date of study approval, confirm your research is ongoing by clicking Confirm Ongoing Research in BullsIRB, or if your research is complete, submit a study closure request in BullsIRB by clicking Create Modification/CR.

In conducting this protocol you are required to follow the requirements listed in the INVESTIGATOR MANUAL (HRP-103).

Sincerely,

Nicholas Hilker
IRB Research Compliance Administrator

Institutional Review Boards / Research Integrity & Compliance

FWA No. 00001669

University of South Florida / 3702 Spectrum Blvd., Suite 165 / Tampa, FL 33612 / 813-974-5638

Page 1 of 1

Appendix C: Data Collection Documents

Study Biomechanics of Human Motion

Data Collection Checklist

Subject ID: _____ Date: _____

- ☐ Subject's Signed Informed Consent Form
- ☐ Subject's Signed Photography Release (required)
- ☐ Collect Subject's Anthropometrics according to Tables 1-3 below:

Table 1: General body parameters.

Parameter	Tool for Measurement	Measured value
Body mass (kg)	Scale	
Height (mm)	Scale	

Table 2: Left-side body parameters.

Parameter	Tool for Measurement	Measured value
Forearm Length (mm)	Soft tape measure	
Upper arm Length (mm)	Soft tape measure	
Hand Length (mm)	Soft tape measure	
Left Shoulder Length (mm)	Soft tape measure	
Waist Knee length (mm)	Soft tape measure	
Knee Height (mm)	Soft tape measure	
Torso Length (mm)	Soft tape measure	

Table 3: Right- side body parameters.

Parameter	Tool for Measurement	Measured value
Forearm Length (mm)	Soft tape measure	
Upper arm Length (mm)	Soft tape measure	
Hand Length (mm)	Soft tape measure	
Right Shoulder Length (mm)	Soft tape measure	
Waist Knee length (mm)	Soft tape measure	
Knee Height (mm)	Soft tape measure	

☐ **Attach Markers as shown in the Appendix (Page 7 & 8)**

Torso/Back	Left Arm	Right Arm
<input type="checkbox"/> CLAV	<input type="checkbox"/> LSHOA	<input type="checkbox"/> RSHOA
<input type="checkbox"/> T1	<input type="checkbox"/> LSHOP	<input type="checkbox"/> RSHOP
<input type="checkbox"/> LBAK	<input type="checkbox"/> LELBM	<input type="checkbox"/> RELB
<input type="checkbox"/> STRN	<input type="checkbox"/> LELB	<input type="checkbox"/> RELBM
<input type="checkbox"/> T10(C7)	<input type="checkbox"/> LWRA	<input type="checkbox"/> RWRA
<input type="checkbox"/> RPSI	<input type="checkbox"/> LWRB	<input type="checkbox"/> RWRB
<input type="checkbox"/> LPSI	<input type="checkbox"/> LFIN	<input type="checkbox"/> RFIN
<input type="checkbox"/> RGT	<input type="checkbox"/> LFRA	<input type="checkbox"/> RFRA
<input type="checkbox"/> LGT	<input type="checkbox"/> LUPA	<input type="checkbox"/> RUPA
<input type="checkbox"/> RASI		
<input type="checkbox"/> LASI		
	Left Leg	Right Leg
	<input type="checkbox"/> LTHI	<input type="checkbox"/> RTHI
	<input type="checkbox"/> LLFC	<input type="checkbox"/> RLFC
	<input type="checkbox"/> LMFC	<input type="checkbox"/> RMFC
	<input type="checkbox"/> LTBI	<input type="checkbox"/> RTBI
	<input type="checkbox"/> LLMAL	<input type="checkbox"/> RLMAL
	<input type="checkbox"/> LMMAL	<input type="checkbox"/> RMMAL
	<input type="checkbox"/> LTOE	<input type="checkbox"/> RTOE
	<input type="checkbox"/> LCAL	<input type="checkbox"/> RCAL

- ☐ Calibrate Cameras and System
- ☐ Zero the Force Plates
- ☐ Collect 2 trials with subject using T-Pose
 - ☐ TPose_1 – Normal Plug-in Gait
 - ☐ TPose_2 – Normal Plug-in Gait
- ☐ Name all data files using the following convention:
 - ☐ FacilityProjectMonthDay-Year_SubjectID_Exercise_TrialNumber
 - ☐ Example: UsfCIFAug01-20_U02_STAND_1
- ☐ Ensure all data for each subject is saved in a folder named:
 - ☐ FacilityProjectMonthDay-Year/SubjectID (subfolder)
- ☐ Collect 3 Static standing trials of the following variations (can be collected while the subject is listening to instructions)
 - ☐ Stand_1 – Normal
 - ☐ Stand_2 – Normal
 - ☐ Stand_3 – Normal

Table 4: Range of Motion trials (ROM) performed to determine how far the subject can move his/her joints in different directions. Figure 2 will be used as a reference for these exercises. Each trial should be marked as completed after all three trials are carried out.

Completed	ROM Exercise	Trial Name
	Shoulder – Flexion/Extension, Abduction/Adduction, Rotation.	SHOROM
	Elbow - Flexion/Extension	ELBROM
	Wrist – Pronation/Supination.	WRIROM
	Torso - forward and lateral bending, and rotation	TORSOROM

Table 5: Activities of Daily Living (ADLs) Tasks to be completed in the RRT lab using the motion capture system. Each (ADLs) Task should be marked as completed after all three trials are carried out.

Completed	ADLs Task	Trial 1 Name	Trial 2 Name	Trial 3 Name
	Pickup Empty Cup	EPC1	EPC2	EPC3
	Pickup Full Cup	FPC1	FPC2	FPC3
	Drinking from Full Cup	FDC1	FDC2	FDC3
	Pickup spoon (Horizontally) and use spoon	PSU1	PSU2	PSU3
	Picking up a toothbrush (Vertically) and brush teeth	PTBV1	PTBV2	PTBV3
	Picking up a toothbrush (Horizontally) and brush teeth	PTBH1	PTBH2	PTBH3
	Brushing Hair	BH1	BH2	BH3
	Picking up a spatula and use	PSS1	PSS2	PSS3
	Picking up a water jug and pour some water into a cup	PWJ1	PWJ2	PWJ3
	Picking up an empty water jug and arrange it on a shelf	PEWJ1	PEWJ2	PEWJ3
	Picking up a jug full of water and arrange it on a shelf	PFWJ1	PFWJ2	PFWJ3
	Picking up a box	PB1	PB2	PB2
	Picking up the duster and performing the dusting task	PDC1	PDC2	PDC3
	Washing utensils	WU1	WU2	WU3
	Opening the cabinet	OC1	OC2	OC3
	Lifting light objects and arranging them on shelving	WLO1	WLO2	WLO3